University of Nottingham
UK | CHINA | MALAYSIA

Mean-field Dynamics of Rydberg-Dressed Bosonic Atoms in Free-Space and Optical Lattices

Gary McCormack

Thesis submitted to the University of Nottingham
for the degree of Doctor of Philosophy

November 2021

To my parents.
Thank you for all your love and support.

Abstract

In the past several decades, cold atom experiments have provided physicists with copious amounts of new discoveries, none more important than that of Bose-Einstein condensation, where laser-cooled bosonic gases '*condense*' into the lowest available energy state of the system. While playing a pivotal role in ultracold experiments, atoms within a Bose-Einstein condensate interact very weakly with one another. A major dichotomy to this is interaction experienced by Rydberg atoms, where the interaction strength between atoms are orders of magnitude larger than standard atom-atom interactions.

In this thesis we examine the dynamical properties of Rydberg-dressed Bose-Einstein condensates under different forms of trapping potentials. The study of the out-of-equilibrium dynamics of Bose-Einstein condensates has lead to a plethora of novel and interesting features. We aim to expand on this already lucrative field by inducing dynamics via Rydberg-dressing, which creates an effective soft-core interaction between the dressed states.

The work chapters will be divided into two main parts. First we study the excitation of roton and maxon modes in a three-dimensional free space model, where the dynamics is induced via an instantaneous quench of the interaction parameters in Chapter 3. The Bogoliubov eigenspectrum develops maxon and roton modes, which are respectively the local maximum and minimum of the spectrum in momentum space. They lead to exotic dynamics associated with the energy scales of the modes. The maxon modes are found to produce stable oscillations which are unseen in dipole-dipole interacting Bose-Einstein condensates. The simulations examined encapsulate the quantum depletion, density-density correlations, and condensate number fluctuation; all of which display two distinct oscillation frequencies, attributed to the development of maxon and roton modes for strongly interacting systems.

In the second half of this thesis, we examine the dynamics of Rydberg-dressed Bose-Einstein condensates, when confined on periodic lattice potentials. In particular, we focus our attention on a Bose-Hubbard chain, as this will allow us to truly utilise the long-range behaviour of the soft-core interaction. This will be discussed in Chapters 4 and 5. The eigenspectra of such systems develop complex anti- and avoided-level crossings. The resulting dynamics is described by mean-field Gross-Pitaevskii equations. This leads to nonlinear and chaotic dynamics in the adiabatic level crossings, and self-trapping behaviour. We show that the system is highly dependent on the initial state, the zero-energy level bias of the traps, and the nonlinear interaction strength. We then expand on the chaotic nature of the system by examining the energetic stability and the Lyapunov exponents. These show that the self-trapping behaviour arises due to strongly positive exponents, as opposed to the conventional idea of the system being energetically unstable. We finally discuss how the chaotic nature of Rydberg-dressing scales

with the size of the system. The findings show that such systems are hyper-chaotic, with the number of positive Lyapunov exponents scaling linearly with the number of sites.

The results of this thesis may prove to be highly useful in the creation of stable Rydberg-dressed Bose-Einstein condensates, and in the field of ultracold atoms as a whole.

Acknowledgements

To begin I would like to thank my supervisor, Professor Weibin Li. I have learned so much in the past few years, and it is all down to his teaching and supervision. More importantly he managed to put up with me for so long, which deserves an award all by itself! While this year has been less than ideal due to the pandemic, he has been able to make time for me whenever I asked him, even though he has a family of his own to worry about. For that, you forever have my gratitude.

While it is almost clichéd to say that your parents were a massive support, I cannot overstate how true this is in my case. During the days I felt like giving up my mother, Sharon, was always on-hand to give me moral support. She may be in a different country at the moment, but it never felt like I was away from her. We bicker and argue like all families do, but I love her with all my heart. I hope this thesis at least makes up partially for the amount of times I have woke you up early in the morning just for a chat. It is always great to catch-up with my father Matt, and my brother Glen. I know they always have my back. To both my grandmothers, Anne and Phyllis, I thank you for all your well-wishes (and the occasional few euro you would slip into my hand without Glen seeing). It has been hard living away from home, but I know that I will be always welcome back with you all whenever I want.

To all my friends back home in Ireland; Kinga, Katya, Hazel, Jay, Seamus, Ellen, Aisling, Dan, Ian, Thomas, Lauren, Jenny, Niamh and everyone else, thank you for never losing touch with me and making my times back home to be as fun as ever. To the amazing people I have found in England; Grady, Hannah, Jemma, Dom, Joe, Matt, Maike, Eliana, Loredana, Grace, Ellie and a plethora of others, thank you for accepting me into your lives. Now you're stuck with me!

Finally I would like to thank my (former) housemate, and one of my oldest friends, Ciarán. You have helped me so much in the past few years, and I wish you all the best with your thesis in the coming months.

Much love to you all.

List of Publications

1. Dynamical Excitation of maxon and roton modes in a Rydberg-dressed Bose-Einstein condensate
   G. McCormack, R. Nath, and W. Li
   Physical Review A: **102** 023319 (2020)

2. Nonlinear dynamics of Rydberg-dressed Bose-Einstein condensates in a triple-well potential
   G. McCormack, R. Nath, and W. Li
   Physical Review A: **102** 063329 (2020)

3. Hyperchaos in a Bose-Hubbard chain with Rydberg-dressed interactions
   G. McCormack, R. Nath, and W. Li
   Photonics: **8** 554 (2021)

Contents

Chapter 1

Introduction

In the field of ultracold gases, there exists no topic more deified by scientists and civilians alike, than Bose-Einstein condensation; a new state of matter where nearly all the atoms in a closed bosonic system 'condense' into the lowest available energy state. Bose-Einstein condensates have practical applications in the related fields of superconductivity and quantum computation, all the way to the other end of the physics spectrum at quantifying the behaviour of dark matter axions particles. However, the problem with this exotic state of matter is that is incredibly fragile, where even the slightest increase in temperature from the environment can trigger a complete collapse of the condensate. This has lead physicists to devote years of research into stabilising and controlling this phenomenon, with some astounding results.

A key way to manipulate these states is by controlling the interatomic interactions between either the atoms in the condensate, or the condensed and non-condensed particles. One such interaction is induced by Rydberg atoms. These atoms produce both strong and long-range interactions, which could in theory allow for highly precise experiments to take place. The problem with these atoms is that they are highly unstable, with life times on the order of microseconds. Unfortunately, this means that Rydberg atoms as they stand, are not a viable option for examining any sort of out-of-equilibrium dynamics, usually associated with dilute ultracold gases. To get around this hurdle, we propose the use of the

more novel states known as Rydberg-dressed states. These states are coupled to the groundstate, giving them extended lifetimes of the order of milliseconds. It should be noted that while the process of dressing the Rydberg atoms diminishes their long-range interaction strength, the resulting two-body interactions are still more than strong enough to produce interesting results.

In Chapter 2, we will present a brief theoretical summary of Bose-Einstein condensation. Key concepts like optical trapping and the famed Bose-Hubbard model are introduced. We discuss the different ground state configurations possible for a Bose-Hubbard Hamiltonian, such as the superfluid and Mott-insulating phases. Next we discuss Rydberg atoms and the related Rydberg-dressed states. These atoms are known to produce a soft-core shaped interaction, which allows for precise control of nearest- and next-nearest-neighbour interactions.

In Chapter 3 we begin by discussing the dynamical properties of dilute Bose gases with short-range two-body interactions, suspended in free-space. This allows us to explain some key concepts, such as collective excitations and Bogoliubov theory. We then expand on this foundation, and introduce Rydberg-dressed interactions to the condensate. This produces novel oscillations in the dynamics, unseen in other forms of long-range interacting Bose-Einstein condensates. We examine the resulting quantum depletion, density-density interactions, and the fluctuations away from the condensed state.

Chapters 4 involves confining Bose-Einstein condensates on neighbouring optical traps. Beginning again with short-range interactions, we introduce the concepts of Landau-Zener transitions when there are two and three traps side-by-side, along with self-trapping, which is analogous to the Mott-insulator of the Bose-Hubbard model. We produce the adiabatic eigenspectra for chains with a fixed number of traps. This allows us to discuss how both avoided and direct level-crossings affected the aforementioned dynamics. By introducing the dressed states into these chains, we find that the adiabatic theorem is unable to be fulfilled due to bifurcations in these energy levels along the ground state. What we find leads

us to the research carried out in chapter 5. As we increase the number of sites in these chains, the system naturally becomes more chaotic. In fact, we show that when there are more than three sites, the system is inherently hyperchaotic. This is verified by examining the dynamical stability and the Lyapunov exponents exponents. The corresponding phase-space representation shows regions of severe chaos, with very few islands of stability found, assuming the long-range interaction parameters are sufficiently large. The relative decrease in the size of phase-space that is encapsulated by chaotic trajectories is shown to be proportional to an increasing number of sites.

Finally in chapter 6 we conclude our examination of Rydberg-dressed Bose-Einstein condensates and discuss some possible next steps that could be used to enrich new research in this already prolific field.

Chapter 2

Theoretical background

In this chapter, we introduce the relevant physics that will play a pivotal role in the coming thesis. We begin in Sec. 2.1 with a brief introduction on ultracold gases. The behaviour of these gases under specific interactions is the main focus of this thesis, and as such, it is important to understand, not only the theory of these gases, but also how we can realise them viably in experiments. From here we discuss optical trapping, which is a natural lead to the extended Bose-Hubbard model; a Hamiltonian that describes the dynamics of bosons between lattice sites, which are subjected to both onsite and offsite interactions. In Sec. 2.2 we introduce the physics behind Rydberg atoms; along with both pros and cons to these highly excited atoms. We then explore the idea of *Rydberg-dressed* states. This interaction is the fundamental concept for the coming chapters.

2.1 Ultracold gases

Ultracold atoms refer to atoms that have been cooled to temperatures near absolute zero. At these energy scales, the quantum mechanical nature of the atom dominates. Experimentally, this regime has been achieved with dilute Bose and Fermi gases, using laser cooling [1]. The experiments have been so fruitful as the high degree of controllability that these atoms innately have allowed for the precise construction of specific Hamiltonians to study. These experiments were

spurred on by decades of theoretical research ranging from the study of ground state phase diagrams, to the exciting area of out-of-equilibrium dynamics, which will be at the forefront of this thesis in later chapters [2].

2.1.1 Bose-Einstein condensation

Arguably one of the most important physical phenomena uncovered in the past several decades is Bose-Einstein condensation. This new state occurs when atoms are cooled to ultracold temperatures, allowing them to occupy the same ground state. In this regime, typical microscopic quantities behave macroscopically. While first being predicted in 1924 by Albert Einstein, it was Satyendra Nath Bose's calculations that developed the relevant statistical physics that describes this new state.

Assuming a system is in thermal equilibrium, the mean occupation state is given by the Bose distribution

$$\bar{n}_s = \frac{1}{\mathrm{e}^{(\mathcal{E}_s-\mu)/k_\mathrm{B}T}-1}, \tag{2.1}$$

where $\mathcal{E}_s$ refers to the single-particle energy in state s, μ is the chemical potential, T is temperature and k_B is Boltzmann's number. This describes the statistics behind identical particles with integer spin, known as bosons. What is clear from Eq. 2.1 is that the single-particle energy and the chemical potential provide a fundamental constraint for the system, where $\mu < \mathcal{E}_0$, $s = 0$ referring to the ground state of the system. This prevents negative occupation of states. For $\bar{n}_s$ to be conserved with decreasing temperature, the chemical potential must increase in turn. The total number of atoms in the system is given by $N = N_c + N_{ex}$, where N_c and N_{ex} represent the condensed and excited atoms respectively.

The density of states for a particle in D-dimensions with a system size L is

$$\rho(\mathcal{E}) = \frac{\Omega_D}{2}\left(\frac{L}{2\pi}\right)^D\left(\frac{2m}{\hbar^2}\right)^{\frac{D}{2}}\mathcal{E}^{\frac{D}{2}-1}, \tag{2.2}$$

where $\Omega_1 = 1$, $\Omega_2 = 2\pi$, and $\Omega_3 = 4\pi$. It can be shown that BECs are in fact unstable in one and two dimensions [3] due to the behaviour of $\rho(\mathcal{E})$. As such, we consider a three-dimensional BEC in the following scenario.

Within the thermodynamic limit, the density of excited atoms in the ultracold gas can be expressed in terms of $\rho(\mathcal{E})$ as

$$n_{ex} = \frac{N_{ex}}{L^3} = \int_0^\infty \frac{\rho(\mathcal{E})\,\mathrm{d}\mathcal{E}}{\mathrm{e}^{(\mathcal{E}-\mu)/k_\mathrm{B}T} - 1}. \tag{2.3}$$

At temperatures close to absolute-zero it is expected that all atoms will condense, meaning that Eq. (2.1) will become

$$N \approx \frac{1}{\mathrm{e}^{-\mu/k_BT} - 1} \tag{2.4}$$

$$\Rightarrow \frac{-\mu}{k_BT} = \log\left(1 + \frac{1}{N}\right) \approx \frac{1}{N} \tag{2.5}$$

Therefore, once N is sufficiently large, the term $\mathrm{e}^{-\mu/k_BT}$ can be set to 1. The number of excited atoms will then be given by

$$n_{ex} = = \frac{1}{4\pi^2}\left(\frac{2m}{\hbar^2}\right)^{\frac{3}{2}} \int_0^\infty \frac{\sqrt{\mathcal{E}}\,\mathrm{d}\mathcal{E}}{\mathrm{e}^{\mathcal{E}/k_\mathrm{B}T} - 1}. \tag{2.6}$$

Using the standard integral $\int \frac{\sqrt{x}}{\mathrm{e}^x - 1} = \zeta_{3/2}\Gamma_{3/2}$, where $\zeta_{3/2}$ is the Riemann-zeta function and $\Gamma_{3/2}$ is the gamma function; $\Gamma_{3/2} = \frac{\sqrt{\pi}}{2}$, we obtain the atom density

$$n = \zeta_{3/2}\left[\frac{2\pi m k_B T}{\hbar^2}\right]^{3/2}. \tag{2.7}$$

This leads to a critical Bose temperature for condensation

$$T_c = \left[\frac{n}{\zeta_{3/2}}\right]^{\frac{2}{3}} \frac{\hbar^2}{2\pi m k_B}. \tag{2.8}$$

For temperatures below this threshold, the bosons will condense into a BEC. Above T_c, and the atoms will have passed the thermal critical value, and the condensate will collapse. The amount of bosons in the ground state is therefore

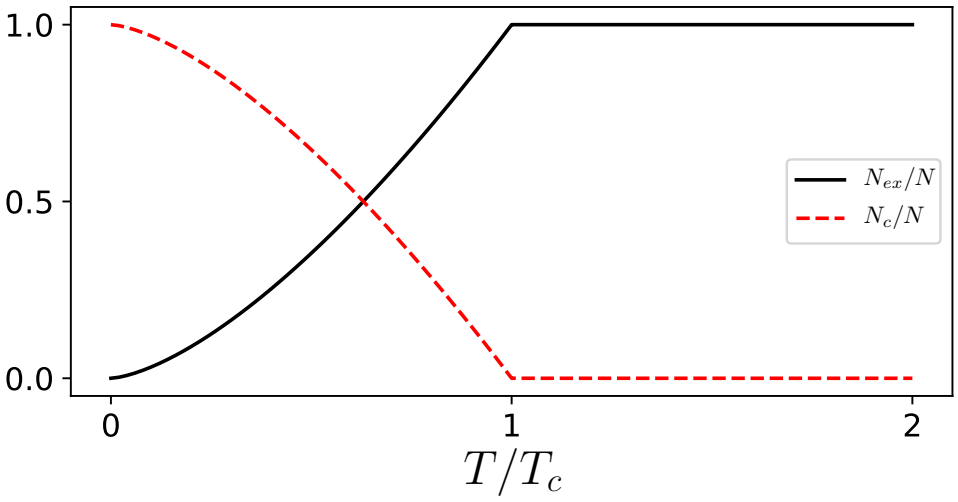

Figure 2.1: ***Critical temperature for BEC transition.*** *The condensed fraction N_c/N and the excited fraction N_{ex}/N is shown. At $T/T_c = 1$ we see that the BEC has been destroyed by the increasing thermal energy.*

given by

$$\frac{N_c}{N} = 1 - \left[\frac{T}{T_c}\right]^{3/2}. \tag{2.9}$$

The first experimental creation of an atomic BEC was achieved in 1995 [4–6].

2.1.2 Preparation of rubidium BECs

As with most aspects of atomic physics, the advent of lasers was crucial to the development of trapping and controlling atoms. Once the required atom sample is created in an oven, they are released towards a *Zeeman slower*, where they are travelling of speeds up to $500 - 600ms^{-1}$. Upon entering the Zeeman slower, a pump laser, shinning in the opposite direction of the incoming particles, slows the atoms to around $10ms^{-1}$. From here they are then captured by a magneto-optical trap, where they are cooled to temperatures close to $100\mu K$. The final step in creating a BEC is 'evaporative cooling', where higher energy particles are removed from the system by incrementally lowering the trap energy, as these particles are found near the boundary of the trap. This technique was originally designed for creation of BECs [6]. It reduces the average thermal energy of the

system as a whole, leading to systems with ultracold energy scales.

2.1.3 Effective interaction between atoms

An important property of ultracold gases is that particle separation is usually an order of magnitude larger than the length scales associated with atom-atom interactions, meaning that we can neglect three-body interactions and focus our attention on two-body interactions.

However, the process of trapping atoms means we are left with a dilute sample as the majority of atoms have been removed through evaporative cooling [1, 6].

For neutral atoms, the main form of interaction between atoms is a weak van der Waals (vdW) interactions scaling as r^{-6}, where r represents the interatomic distance. At short distances, where the orbitals of the atoms begin to overlap, this vdW interaction is superseded by a strong Coulomb interaction, meaning that the full scattering process for these atoms becomes quite complex [2, 7].

In order to calculate the full interaction, one would need to evaluate short-range correlations between atoms when constructing the many-body Hamiltonian. This can be avoided however by introducing the concept of an effective interaction. This describes the process of 'integrating out' short-wavelength degrees of freedom in the interaction [8].

The scattering process for a pair of particles is due to s-wave interactions [9], and can be characterised by a single parameter, called the scattering length. The Born approximation tells us that the scattering length is given as

$$a_{\text{Born}} = \frac{m_{\text{r}}}{2\pi\hbar^2} \int \mathrm{d}\mathbf{r} U(\mathbf{r}). \tag{2.10}$$

What has been shown is that the low-energy scattering process is described with a great accuracy using only an effective two-body interaction U_{eff}. This means

that the interaction takes the following form

$$\int \mathrm{d}\mathbf{r} U_{eff}(\mathbf{r}) = \frac{2\pi\hbar^2 a_s}{m_\mathrm{r}} \tag{2.11}$$

For a particle of equal mass m, the reduced mass is simply $m_\mathrm{r} = m/2$, meaning that we obtain

$$U_0(\mathbf{r} - \mathbf{r}') \quad = \quad \frac{4\pi a_s \hbar^2}{m}\delta(\mathbf{r} - \mathbf{r}'), \tag{2.12}$$

where a_s is the scattering length of the atoms, which is typically on the magnitude of $10^3 a_0$, the Bohr radius being $a_0 = 0.529\,\text{Å}$. This result shows that a pair of particles may exhibit an effective contact interaction, by means of the scattering process, while vdW interactions are suppressed due to the large spacing between atoms.

2.1.4 Optical lattices

Atoms in a BEC can be trapped optically using lasers [10]. Expanding on that, atoms can be trapped in periodic potentials using standing waves, creating optical lattices. While first being suggested by Letokhov in 1968 [11], it was nearly two decades later until the world saw the advent of the first optical lattice by Saloman *et. al.* in 1987 [12]. A standing wave laser field is periodic in space, meaning that they form periodic potentials due to the stark effect [9]. These are then used to trap groups of atoms, where they are subjected to a periodic lattice potential $V_\mathrm{lat}(r)$, such that $V_\mathrm{lat}(r + d) = V_\mathrm{lat}(r)$, where d is that lattice spacing.

The motional energy eigenstate for a particle in an infinite length periodic potential is described by a Bloch function $\phi_{b,\mathbf{q}}$, where b is the energy band that the particle is localised on in the potential and $\mathbf{q}$ is the quasi-momentum. The wavefunction for such states is therefore simply $\hat{u}_\mathbf{q}(\mathbf{r}) = \phi_{b,\mathbf{q}}(\mathbf{r})\mathrm{e}^{\mathrm{i}\mathbf{q}\cdot\mathbf{r}}$ The Fourier

transform of these form a complete basis which takes the form

$$W_b(\mathbf{r}-\mathbf{r}_j) = \sum_{\mathbf{q}\in \mathrm{BZ}} \phi_{b,\mathbf{q}}(\mathbf{r}) \mathrm{e}^{\mathrm{i}\mathbf{q}\cdot\mathbf{r}}, \tag{2.13}$$

where the summation is restricted to the first Brillouin zone. These are known as Wannier functions, and they describe the wave function localised around each site j.

Assuming that we are using a deep lattice, the atoms are further localised in the lowest Bloch band of the Wannier functions, meaning $b = 0$. The connection between these Wannier functions and the field operator $\psi(\mathbf{r})$ is

$$\hat{\psi}(\mathbf{r})^{(\dagger)} = \sum_j W^{(*)}(\mathbf{r}-\mathbf{r}_j)\hat{a}_j^{(\dagger)}, \tag{2.14}$$

where $\hat{a}_j^{(\dagger)}$ is the annihilation (creation) operator associated with the Wannier state at site j.

2.1.5 Gross-Pitaevskii equation

One of the pillars of quantum mechanics is the Schrödinger equation, which describes the dynamics of non-interacting particles. However when many-body interactions are introduced, we need to look elsewhere to model the dynamics seen.

As we are switching to a many-body picture, we begin with a second quantization Hamiltonian with short-range interactions $U(\mathbf{r}-\mathbf{r}') = U_0\delta(\mathbf{r}-\mathbf{r}')$ [see Eq. 2.12]. The total Hamiltonian of the system is

$$\hat{H} = \hat{H}_0 + \hat{H}_s \tag{2.15}$$

where

$$\begin{aligned}\hat{H}_0 &= \int \hat{\psi}^\dagger(\mathbf{r})\Big(-\frac{\nabla^2\hbar^2}{2m} - \mu + V_{\text{lat}}(\mathbf{r})\Big)\hat{\psi}(\mathbf{r})\,\mathrm{d}\mathbf{r} \\ \hat{H}_s &= \frac{1}{2}\int \hat{\psi}^\dagger(\mathbf{r})\hat{\psi}^\dagger(\mathbf{r}')U(\mathbf{r}-\mathbf{r}')\hat{\psi}(\mathbf{r})\hat{\psi}(\mathbf{r}')\,\mathrm{d}\mathbf{r}\,\mathrm{d}\mathbf{r}', \qquad (2.16) \\ &= \frac{U_0}{2}\int \hat{\psi}^\dagger(\mathbf{r})\hat{\psi}^\dagger(\mathbf{r})\hat{\psi}(\mathbf{r})\hat{\psi}(\mathbf{r})\,\mathrm{d}\mathbf{r}. \qquad (2.17)\end{aligned}$$

Here, $\hat{\psi}(\mathbf{r})$ is given by Eq. (2.14), ∇ is the gradient operator, and $V_{\text{lat}}(\mathbf{r})$ is a periodic lattice potential. The field operator obeys standard bosonic commutation relations as

$$\begin{aligned}\left[\hat{\psi}\left(\mathbf{r}\right),\hat{\psi}^\dagger\left(\mathbf{r}'\right)\right] &= \delta\left(\mathbf{r}-\mathbf{r}'\right) \\ \left[\hat{\psi}\left(\mathbf{r}\right),\hat{\psi}\left(\mathbf{r}'\right)\right] &= \left[\hat{\psi}^\dagger\left(\mathbf{r}\right),\hat{\psi}^\dagger\left(\mathbf{r}'\right)\right] = 0. \qquad (2.18)\end{aligned}$$

By means of the Heisenberg equations, we can then derive the equations of motion for the field $\hat{\psi}(\mathbf{r})$ as

$$\mathrm{i}\hbar\frac{\partial}{\partial t}\hat{\psi}(\mathbf{r}) = \left[\hat{\psi}(\mathbf{r}),\hat{H}\right]. \qquad (2.19)$$

By neglecting any correlations beyond quadratic order, the Gross-Pitaevskii equation of motion is found as

$$\mathrm{i}\hbar\frac{\partial}{\partial t}\hat{\psi}(\mathbf{r}) = \left(-\frac{\nabla^2\hbar^2}{2m} + V_{\text{lat}}\left(\mathbf{r}\right) + U_0|\hat{\psi}\left(\mathbf{r}\right)|^2\right)\hat{\psi}\left(\mathbf{r}\right). \qquad (2.20)$$

2.1.6 Bose-Hubbard model

Bosonic lattice systems can also be described by the *Bose-Hubbard model* (BHM). Originally Hubbard's model was used to describe electrons in a crystalline solid and superconductors [13]. The model rose to the forefront of bosonic physics when it successfully predicted the superfluid-Mott insulator phase transition [14]. The BHM in general is used to describe atoms with short-range interactions,

controlled by s-wave interactions [see Eq. (2.12)].

By using Eq. (2.14), and substituting this into Hamiltonian (2.15), the BHM is found as

$$\hat{H} = \sum_{i}^{L}(\Gamma_j - \mu)\hat{n}_j - \sum_{\langle i,j\rangle}^{L} J_{i,j}\hat{a}_i^{\dagger}\hat{a}_j + \frac{U_0}{2}\sum_{j}^{L}\hat{n}_j(\hat{n}_j - 1). \tag{2.21}$$

J controls the strength of the quantum tunnelling between lattice sites, while Γ_j is a local potential operator for any given lattice site.

In this situation, the parameters are given in terms of the Wannier functions on each site as

$$J_{i,j} = \int \mathrm{d}\mathbf{r} W^*(\mathbf{r} - \mathbf{r}_i)\left(- \frac{\nabla^2\hbar^2}{2m} + V_{\mathrm{lat}}(\mathbf{r})\right)W(\mathbf{r} - \mathbf{r}_j), \tag{2.22}$$

$$\Gamma_j = \int \mathrm{d}\mathbf{r}|W(\mathbf{r} - \mathbf{r}_j)|^2 V_{\mathrm{lat}}(\mathbf{r} - \mathbf{r}_j), \tag{2.23}$$

$$U_0 = \int \mathrm{d}\mathbf{r}|W(\mathbf{r})|^4 U(\mathbf{r}). \tag{2.24}$$

It should also be made clear that quantum tunnelling between sites becomes exponentially suppressed across any sites on the lattice that are not nearest neighbour [2, 15]. This is indicated by $\langle ... \rangle$ in the summation in Hamiltonian (2.29).

The most fundamental results of the Bose-Hubbard model are that of the fabled superfluid-Mott insulator transition. In the Mott phase, the atoms remain completely localised in their respective sites due to the dominance of the interaction strength. Once the tunnelling strength dominates, the atoms enter the superfluid phase where they move freely between sites with no resistance. The order parameter governing this phase transition is the expectation value of creation operator $\phi_i = \langle \hat{a}_i \rangle$. In the Mott phase, $\phi = 0$ as hopping is completely suppressed. In the superfluid phase, $|\phi| > 0$. Approaching the Hamiltonian from a mean-field perspective, and assuming a flat periodic lattice potential [$\Gamma_j = 0 \ \forall \ j$] the many-body Hamiltonian can be decomposed into single-body Hamiltonians by means

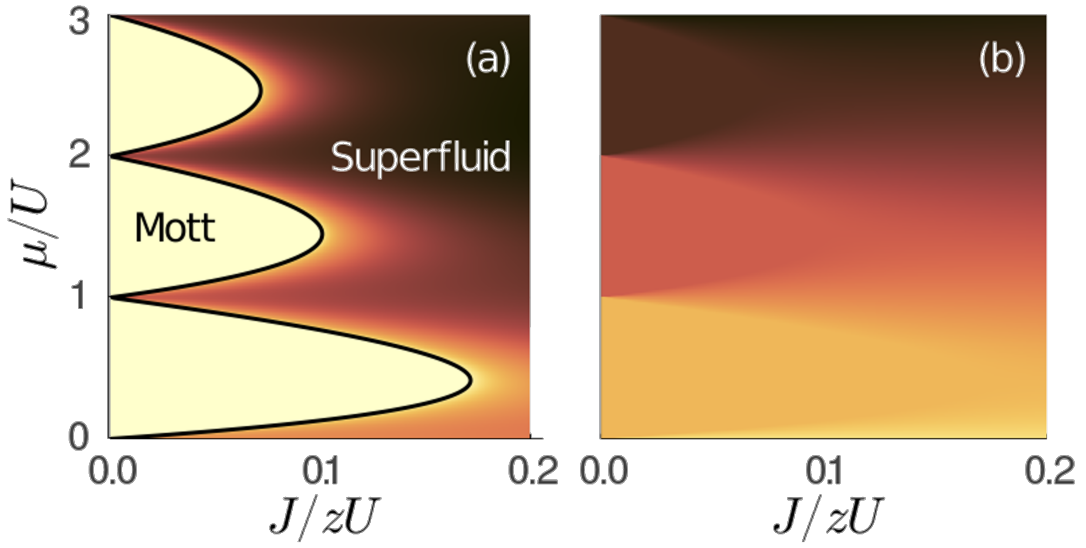

Figure 2.2: ***Phase Diagrams for the Bose-Hubbard Model.*** *The phase diagrams for the order parameter ϕ(a) and the average density $\bar{n}$ (b) are shown. The order parameter shows the clear dichotomy between the Mott phase and the superfluid phase. The black line shows the analytic boundary found by Landau's mean-field theory. Here we show up to and including $\bar{n} = 3$.*

of the approximation $\hat{a}_i^\dagger \hat{a}_j \approx \phi_i^* \hat{a}_j + \phi_j \hat{a}_i^\dagger - \phi_i^* \phi_j$, and by examining only the site j, where the site index can be neglected. The single-body Hamiltonian can therefore be expressed as

$$H = -J\phi(\hat{a}^\dagger + \hat{a}) + J\phi^2 + \frac{U_0}{2} n(n-1) - \mu n. \tag{2.25}$$

The groundstate is always real, and therefore the complex components of ϕ_j can be neglected. Direct diagonalisation of the above mean-field Hamiltonian produces a superfluid-insulator phase map. We can additionally calculate expected densities as $n = \phi^2$.

Additionally, Hamiltonian (2.25) can be expressed as $H = H_{int} + H_{hop}$. The Hamiltonian H_{int} is the interaction Hamiltonian, of which the occupation number state $|n\rangle$ is an eigenstate, such that $H_{int}|n\rangle = E_{int}|n\rangle$. The eigenenergy is $E_{int} = \frac{U}{2} n(n-1) - \mu n$. The energy of the hopping Hamiltonian can be found by

perturbation theory as

$$\begin{aligned} E_{hop} &= \sum_{m \neq n} \frac{|\langle n|H_{hop}|m\rangle|^2}{E_m - E_n} \\ &= (J\phi)^2 \left[\frac{U_0 n}{U_0(n-1) - \mu} - \frac{n+1}{U_0 n - \mu} \right]. \end{aligned} \tag{2.26}$$

This means that the total energy using this occupation number state can be expressed in the following form $E = E_{int} + E_{hop} = a \pm b\phi^2$. Landau's formulation for second-order phase transition [16] tells us that the the flipping of b from positive to negative determines the occurrence of a phase transition. This allows us to analytically find the phase boundary for the parameters J and μ for different occupation numbers $\bar{n}$ as

$$J/U_0 = \left(\frac{n}{U_0(n-1) - \mu} - \frac{n+1}{U_0 n - \mu} \right)^{-1}. \tag{2.27}$$

Both the analytical and direct diagonalisation phase boundaries are shown in Fig. 2.2.

2.1.7 Extended Bose-Hubbard model

A natural extension to the Bose-Hubbard model is the inclusion of density-density interactions from neighbouring sites. This addition is known as the *extended Bose-Hubbard model* (eBHM).

Assuming a nonlocal interaction $V(\mathbf{r} - \mathbf{r}')$, the second quantization Hamiltonian 2.16 picks up an additional energy term $\hat{H}_L$

$$\hat{H}_L = \frac{1}{2} \int \hat{\psi}^\dagger(\mathbf{r}_i)\hat{\psi}^\dagger(\mathbf{r}_j)V(\mathbf{r} - \mathbf{r}')\hat{\psi}(\mathbf{r}_i)\hat{\psi}(\mathbf{r}_j)\, \mathrm{d}\mathbf{r}_i\, \mathrm{d}\mathbf{r}_j, \tag{2.28}$$

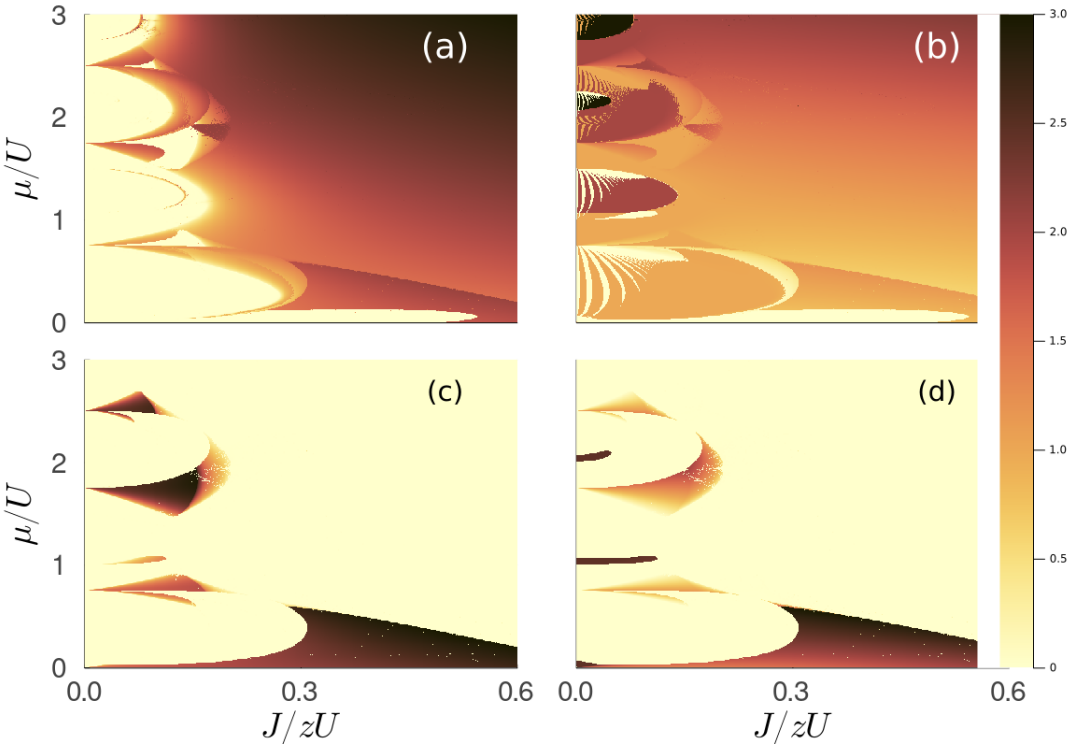

Figure 2.3: ***Phase Diagrams for the Extended-Bose-Hubbard Model.*** *The first order parameter is shown in (a), along with the onsite density in (b). We also show both $\Delta\phi$ (c) and Δn (d). The long-range interaction parameter in this scenario is $V_{i,j}/U_0 = 1.5$.*

Using the same methodology as before, we obtain the following Hamiltonian

$$\hat{H}_L = \sum_i^L (\Gamma_j - \mu)\hat{n}_j - \sum_{\langle i,j\rangle}^L J_{i,j}\hat{a}_i^\dagger \hat{a}_j + \frac{U_0}{2}\sum_j^L \hat{n}_j(\hat{n}_j - 1) + \frac{1}{2}\sum_{i,j}^L V_{i,j}\hat{n}_i\hat{n}_j. \tag{2.29}$$

where the final terms dictates the interactions between neighbouring sites and

$$V_{i,j} = \int \mathrm{d}\mathbf{r}\,\mathrm{d}\mathbf{r}' |W(\mathbf{r} - \mathbf{r}_i)|^2 V(\mathbf{r}_i - \mathbf{r}_j)|W(\mathbf{r}' - \mathbf{r}_j)|^2. \tag{2.30}$$

The addition of the long-range interactions mean that we need another order parameter to account for next-nearest neighbour-interactions. In this case, if sites i and j are nearest-neighbours, then the two order parameters are ϕ_j and ϕ_{j+1}, meaning that $\hat{a}_j^\dagger \hat{a}_j \approx \phi_j^* \hat{a}_j + \phi_j \hat{a}_j^\dagger - \phi_j^* \phi_j$ and $\hat{a}_j^\dagger \hat{a}_{j+1} \approx \phi_j^* \hat{a}_{j+1} + \phi_{j+1}\hat{a}_j^\dagger - \phi_j^* \phi_{j+1}$. We can then quantify the phases by looking at the differences in both the order

parameters $\Delta\phi$, and the densities Δn. When $\phi_j = \phi_{j+1} = 0$ and $n_j = n_{j+1}$ then we are in the superfluid phase where atoms are free to move from site to site without restriction, and the system is homogeneous in density. When $\phi_j \neq \phi_{j+1}$ and $n_j \neq n_{j+1}$ we enter the regime dominated by supersolidity.

Like a superfluid, atoms have free movement between sites, however there will exist order in spatial modulations in the densities, forming a pseudo-lattice structure of varying densities. Now, in the case where both $\phi_j = \phi_{j+1} = 0$ we enter insulating regions, where atom movement is restricted. There are two scenarios for this, either we are in a Mott-insulting phase where $n_j = n_{j+1}$ or density-wave phase where $n_j \neq n_{j+1}$. For example, all of this information can be extrapolated from Fig. 2.3, where we have set the long-range interaction parameter as $V_{i,j}/U_0 = 1.5$, and restrict our calculation to include onsite, and nearest neighbour interactions only. In Fig. 2.3 (a) and (b) we respectively show the order parameter ϕ_j and the density n_j. Additionally we show the difference in the two order parameters and the difference in the two densities, $\Delta\phi$ and Δn. From these we can infer the densities of the other order parameter, thus distinguishing the phases seen in the extended Bose-Hubbard model.

Superfluidity, supersolidity, and insulating phases will play a pivotal role in the coming chapters.

2.2 Rydberg Interactions

To fully realise the potential of the many-body quantum states described so far, we need highly controllable and strong interatomic interactions. One of the methods that has been at the forefront of ultracold physics for the past few decades is manipulating Rydberg states.

2.2.1 Rydberg states

In the early years of quantum mechanics, Niels Bohr successfully developed a model that quantised the orbital angular momentum of the electron in a hydrogen atom, showing that energies at the smallest scales are distributed into quanta. His model says that the energy of a quantum state with a specific integer principal quantum number $\mathcal{N}$ is

$$E_{\mathcal{N}} = -\frac{Z^2}{\mathcal{N}^2}\mathrm{Ry}. \tag{2.31}$$

Here $\mathrm{Ry} = \frac{e^4 m_r}{32\varepsilon^2\hbar^2\pi^2}$ is the Rydberg energy unit, where e is the electron charge, ε is the free space permittivity and m_r is the reduced mass between the valance electron and the atomic core. Eq. (2.31) describes the scaling behaviour for alkali atoms, such as sodium, rubidium, and caesium. States where $\mathcal{N} \gg 1$ are known as Rydberg states. This model can be extended to multi-electron atoms using quantum defect [17], which were originally described by Rydberg himself in 1890 [18]. It is well known that Rydberg atoms have interesting and unique properties such as experiencing long-range two-body van der Waals (vdW) interactions as well as allowing high precision research to be undertaken with a large degree of controllability [19]. These atoms may be used in the formation of exotic quantum phases including solitons, the melting of ordered crystalline states to disordered liquids, and supersolidity, where the translational symmetry of a superfluid is broken [20–31]. These strong interatomic interactions scale in strength as $\mathcal{N}^{11}$. This can suppress other excitations by shifting the energy levels of neighbouring

atoms within a certain volume, known as the Rydberg blockade, where the typical length scale is much larger than the average coherence length of a Bose gas [32, 33]. The radiative lifetime of Rydberg states has been shown to scaled as roughly $\mathcal{N}^3$ In general, the lifetime of a Rydberg atom with $\mathcal{N} \sim 50$ is of the order of 100μs, which is far too quick to allow for the evolution of out-of-equilibrium dynamics [34].

2.2.2 Rydberg-dressed states

To compensate for the lack of longevity of Rydberg states, we propose an alternative process known as *Rydberg-dressing*, where the groundstate is dressed via laser coupling to excited Rydberg states. This creates a new groundstate of Rydberg-dressed atoms, where a weak admixture of Rydberg states modifies the neutral atom groundstate. The lifetime of these dressed atoms can be observed to be as large as 10ms [35]. This means that by applying a Born-Oppenheimer approximation, the Rydberg states are adiabatically eliminated, leaving a Bose gas of only Rydberg-dressed atoms whose properties can be exploited.

These dressed states also allow for their own interesting properties, such as the formation of quantum magnets [36], the creation of strongly correlated phases which can lead to a quantum-classical crossover [37], and can show coherent quantum transport [38]. Furthermore, in recent years, they have become more accessible in experiments due to more advanced theoretical methods of observation [39]. Additionally, recent experiments have successfully demonstrated Rydberg-dressing in optical tweezers [39], optical lattices [40–42], and traps [43, 44].

2.2.3 Soft-core interaction

Dressing the groundstate with Rydberg states is done by utilising a highly detuned laser as illustrated in Fig. 2.4. To begin, we have the electronic Hamiltonian

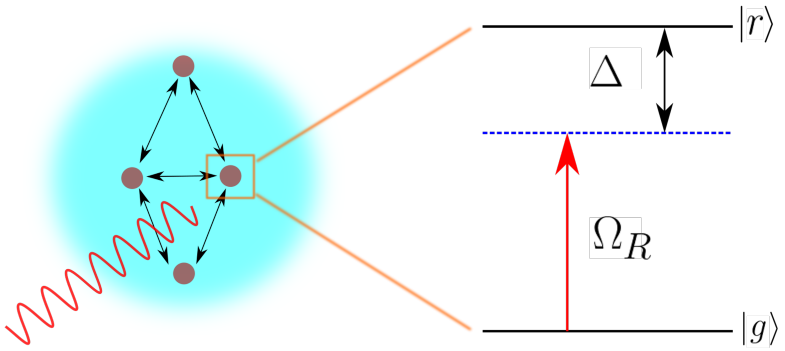

Figure 2.4: ***Bose gas of Rydberg-dressed bosons.*** *A Bose gas interacting in free space, being radiated by a driving laser, producing the Rydberg-dressed interaction with detuning Δ and Rabi frequency Ω_R.*

coupling a high-lying Rydberg state $|r\rangle$ to the ground state $|g\rangle$

$$\hat{H}_r = \sum_j \sum_{i<j} V_{i,j} \sigma_{rr}^{(i)} \sigma_{rr}^{(j)} - \Delta \sum_j \sigma_{rr}^{(j)} + \frac{\Omega_R}{2} \sum_{i,j} \left[\sigma_{rg}^{(i)} + \sigma_{gr}^{(j)} \right], \tag{2.32}$$

where Δ is the detuning and Ω_R is the Rabi frequency of oscillations between the ground state and the excited state. $V_{\alpha,\beta} = C_0/|\mathbf{r}_i - \mathbf{r}_j|^6$ is the Rydberg-Rydberg interaction potential between states α and β, while $\sigma_{\alpha\beta}^j = |\alpha\rangle_j \langle\beta|$ is the jump operator between states α and β on site j. C_0 is the vdW dispersion coefficient for the excited Rydberg states, which controls the strength of the dressed interaction. For this calculation let us consider a simple two-atom model. The Hamiltonian can then be expressed as

$$\begin{aligned} \hat{H}_{r2} &= V_{1,2} \sigma_{rr}^{(1)} \sigma_{rr}^{(2)} + \Delta \left[\sigma_{rr}^{(1)} \otimes \mathbb{I} + \mathbb{I} \otimes \sigma_{rr}^{(2)} \right] \\ &+ \frac{\Omega_R}{2} \left[\sigma_{gr}^{(1)} \otimes \mathbb{I} + \sigma_{rg}^{(1)} \otimes \mathbb{I} + \mathbb{I} \otimes \sigma_{gr}^{(2)} + \mathbb{I} \otimes \sigma_{rg}^{(2)} \right] \end{aligned} \tag{2.33}$$

The single atom excitation Hamiltonian is then

$$\hat{H}_0 = \begin{pmatrix} V_{1,2} + 2\Delta & 0 & 0 & 0 \\ 0 & \Delta & 0 & 0 \\ 0 & 0 & \Delta & 0 \\ 0 & 0 & 0 & 0 \end{pmatrix}, \tag{2.34}$$

while the interaction Hamiltonian is

$$\hat{H}_I = \frac{\Omega_R}{2} \begin{pmatrix} 0 & 1 & 1 & 0 \\ 1 & 0 & 0 & 1 \\ 1 & 0 & 0 & 1 \\ 0 & 1 & 1 & 0 \end{pmatrix}. \tag{2.35}$$

As we can see the single-atom Hamiltonian is degenerate in Δ. To avoid complexity in the mathematics, we switch our basis to the dressed-atom basis of

$$|gg\rangle = \begin{pmatrix} 0 \\ 0 \\ 0 \\ 1 \end{pmatrix}, \; |rr\rangle = \begin{pmatrix} 1 \\ 0 \\ 0 \\ 0 \end{pmatrix}, \text{ and } \; |D\rangle = \frac{1}{\sqrt{2}} \begin{pmatrix} 0 \\ 1 \\ 1 \\ 0 \end{pmatrix}, \tag{2.36}$$

where $|D\rangle = |gr\rangle$ is the symmetric dressed state. The anti-symmetric dressed state is decoupled and can be neglected from this point. Within this basis, we avoid degenerate energy levels since

$$\hat{H}_0' = \begin{pmatrix} V_{1,2} + 2\Delta & 0 & 0 \\ 0 & \Delta & 0 \\ 0 & 0 & 0 \end{pmatrix}, \tag{2.37}$$

and

$$\hat{H}_I' = \frac{\Omega_R}{\sqrt{2}} \begin{pmatrix} 0 & 1 & 0 \\ 1 & 0 & 1 \\ 0 & 1 & 0 \end{pmatrix}. \tag{2.38}$$

The eigenvalues of the unperturbed Hamiltonian can be simply read as $E_{rr} = V_{1,2} + 2\Delta$, $E_d = \Delta$, and $E_{gg} = 0$. The matrix elements of the interaction Hamiltonian are given by $H_{n,m} = \langle n|H_i'|m\rangle$. We then apply a fourth-order perturbative

expansion on the ground state, of the form

$$E_{gg}^{(4)} = \sum_{\gamma\neq gg}\sum_{\alpha\neq gg}\sum_{\beta\neq gg}\frac{H_{gg,\gamma}H_{\gamma,\alpha}H_{\alpha,\beta}H_{\beta,gg}}{(E_{gg}-E_\gamma)(E_{gg}-E_\alpha)(E_{gg}-E_\beta)} - E_{gg}^{(2)}\sum_\gamma\frac{|H_{gg,\gamma}|^2}{(E_{gg}-E_\gamma)^2}, \tag{2.39}$$

where the superscripts denote the perturbative order, and $E_{gg}^{(1)} = E_{gg}^{(3)} = 0$. The perturbation can then be expressed as

$$E_{gg}^{(4)} = \frac{4\Omega_R^4}{\Delta^3}\left[1 - \frac{\Delta}{V_{1,2}+2\Delta}\right] \tag{2.40}$$

Recalling that the van der Waals interaction between atoms 1 and 2 is $V_{1,2} = C_0/|\mathbf{r}_1-\mathbf{r}_2|^6$, we can simplify Eq. (2.40) as follows;

$$\begin{aligned} E_{gg}^{(4)} &= \frac{4\Omega_R^4}{\Delta^3}\left[\frac{V_{1,2}+\Delta}{V_{1,2}+2\Delta}\right] \\ &= \frac{4\Omega_R^4}{\Delta^3}\frac{1}{2}\left[\frac{C_0/|\mathbf{r}_1-\mathbf{r}_2|^6+\Delta}{C_0/\left(2|\mathbf{r}_1-\mathbf{r}_2|^6\right)+\Delta}\right] \\ &= \frac{4\Omega_R^4}{\Delta^3}\left\{\frac{1}{2}+\frac{1}{2}\left[\frac{C_0}{C_0/2\Delta+|\mathbf{r}_1-\mathbf{r}_2|^6}\right]\right\} \\ &= \frac{2\Omega_R^4}{\Delta^3}+\frac{2\Omega_R^4}{\Delta^3}\frac{C_0}{C_0/2\Delta+|\mathbf{r}_1-\mathbf{r}_2|^6}, \end{aligned} \tag{2.41}$$

Rydberg-dressing creates an effective interaction which is soft-core in nature meaning [23–26, 28, 30, 45–48] that interactions are constant between neighbouring atoms within a range known as the soft-core radius [27]. This length scale is analogous to the Condon Radius for interatomic interactions [49], and is denoted by $R = (C_0/2\Delta)^{1/6}$. With this, and Eq. (2.41), the soft-core interaction takes the following form (up to a constant),

$$\Lambda(\mathbf{r}-\mathbf{r}') = \frac{C_0}{R^6+|\mathbf{r}-\mathbf{r}'|^6}. \tag{2.42}$$

The interaction potential saturates to a constant, i.e., $\Lambda(\mathbf{r}) \to C_0/R^6$ when

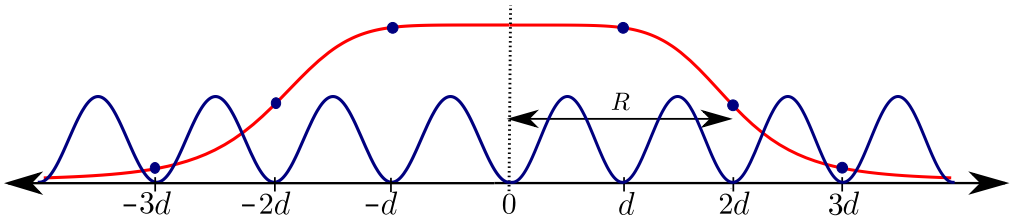

Figure 2.5: ***Different length scales in a Rydberg-dressed system.*** *The different length scales between an optical lattice is compared with a Rydberg-dressed soft-core interaction (red curve). The soft-core radius R can span multiple lattice sites.*

$|\mathbf{r}| \ll R$, and approaches to a vdW type at distances of $|\mathbf{r}| \gg R$, i.e., $\Lambda(\mathbf{r}) \to C_0/|\mathbf{r}|^6$. What is interesting is that typically $R \gg d$ (d being the lattice spacing), meaning that the range of this interaction can span, not only distances vastly exceeding standard boson coherence lengths, but also multiple lattice sites where the strength of the off-site coupling is equal in magnitude to the onsite coupling [45].

For a discrete system the soft-core interaction may be expressed as

$$\Lambda_{i,j} = \frac{C_0}{R^6 + d^6|i-j|^6}. \tag{2.43}$$

where i and j are the site indices. This will coincide with the notation used in Chapters 4 and 5.

Chapter 3

Roton and maxon excitations in a Rydberg-dressed Bose-Einstein condensate

In this chapter, we investigate the dynamics of a three-dimensional Bose-Einstein condensate of ultracold atomic gases with a soft-core shape long-range interaction, which is induced by laser dressing the atoms with a highly excited Rydberg state. For a homogeneous condensate, the long-range interaction drastically alters the dispersion relation of the excitations, supporting both roton and maxon modes. Rotons are typically responsible for the creation of supersolids, while maxons are normally dynamically unstable in BECs with dipolar interactions. We show that maxon modes in the Rydberg-dressed condensate, on the contrary, are dynamically stable. We find that the maxon modes can be excited through an interaction quench, i.e. turning on the soft-core interaction instantaneously. The emergence of the maxon modes is accompanied by oscillations at high frequencies in the quantum depletion, which is the process of losing atoms within the condensate. Roton modes on the other hand lead to much slower oscillations. The dynamically stable excitation of the roton and maxon modes leads to persistent oscillations in the quantum depletion. Through a self-consistent Bogoliubov approach, we

identify the dependence of the maxon mode on the soft-core interaction. Our study shows that maxon and roton modes can be excited dynamically and simultaneously by quenching Rydberg-dressed long-range interactions. This is relevant to current studies in creating and probing exotic states of matter with ultracold atomic gases. Several sections of the following chapter have been transcribed verbatim (with minor changes to symbols and mathematical notation to comply with the overall continuity), along with the accompanying data and figures, from the following publication:

"Dynamical excitation of maxon and roton modes in a Rydberg-dressed Bose-Einstein condensate"

G. McCormack, R. Nath, and W. Li

Physical Review A: **102** 023319 (2020) [50]

3.1 Introduction

Collective excitations induced by particle-particle interactions play an important role in the understanding of static and dynamical properties of many-body systems. The ability to routinely create and precisely control properties of ultracold atomic gases opens exciting prospects to manipulate and probe collective excitations. In weakly interacting Bose-Einstein condensates (BECs) with s-wave interactions [2, 7, 9, 51], phonon excitations reduce the condensate density, giving rise to *quantum depletion* [52]. It has been shown [35] that quantum depletion can be enhanced by increasing the s-wave scattering length through Feshbach resonances [53, 54]. By dynamically changing the s-wave scattering length [55], phonon excitations can alter the quantum depletion, the momentum distribution [56], correlations [57], contact [58–61], and statistics [62] of the condensate. Moreover the phonon induced quantum depletion plays a vital role in the formation of droplets in BECs [63].

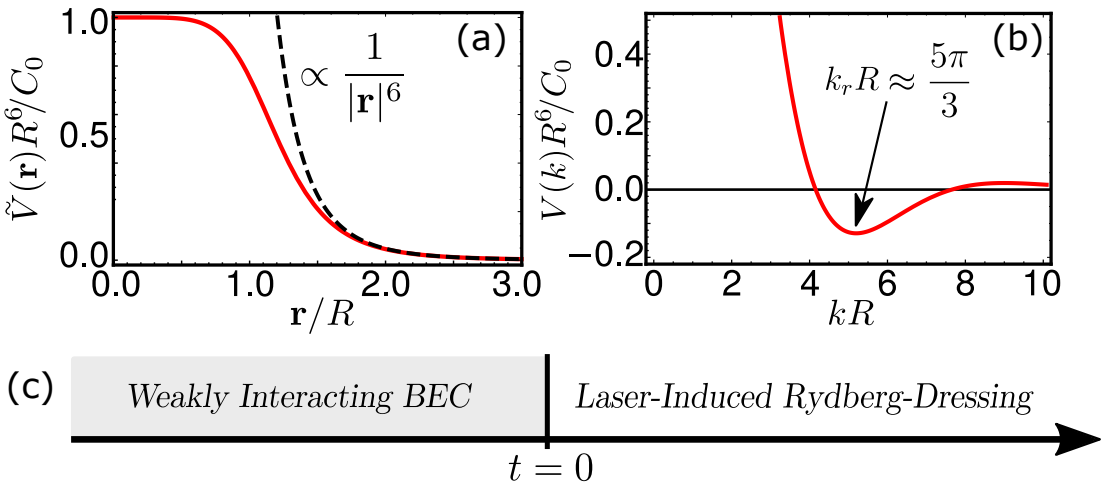

Figure 3.1: ***Soft-core interaction and quench scheme.*** *(a) The soft-core interaction as a function of the interatomic distance* $\mathbf{r}$*. Energy is scaled by* R^6/C_0 *with* R *and* C_0 *to be the soft-core radius and dispersion coefficient. The interaction is constant when* $\mathbf{r} \ll R$*, and becomes a vdW type when* $\mathbf{r} \gg R$*. (b) Fourier transformation of the soft-core interaction. The minimum of the interaction locates at* $k_rR \approx 5\pi/3$*, where the interaction is attractive. (c) The quench scheme. A weakly interacting BEC with s-wave interactions is first prepared. The laser dressing is applied at time* $t = 0$*, which induces the soft-core interaction.*

When long-range interactions are introduced, the dispersion relation corresponding to the quasiparticle spectrum of a BEC is qualitatively different, where the excitation energies of the collective modes depend non-monotonically on the momentum. Previously BECs with dipole-dipole interactions have been extensively examined [64–70]. In two-dimensional (2D) dipolar BECs [71], *roton* and *maxon* modes emerge, where roton (maxon) modes correspond to local minima (maxima) in the dispersion relation. The strength of dipolar interactions can be tuned by either external electric or magnetic fields [68]. When instabilities of roton modes are triggered, a homogeneous BEC undergoes density modulations such that a supersolid phase could form. The existence of roton modes has been supported by a recent experiment [72]. Maxon modes, on the other hand, normally appear at lower momentum states [71]. It was shown however that the maxon modes in dipolar BECs are typically unstable and decay rapidly through the Beliaev damping [64, 69].

Strong and long-range interactions are also found in gases of ultracold Rydberg atoms [22, 29, 31, 73, 74]. As a result, *Rydberg-dressing* is proposed as an alternate

long-range interaction. In this chapter, we study excitations of roton and maxon modes in three dimensional (3D) Rydberg-dressed BECs in free space at zero temperature. Three dimensional uniform trapping potentials of ultracold atoms have been realized experimentally [75]. When the soft-core interaction is strong, both the roton and maxon modes are found in the dispersion relation of the collective excitations. Starting from a weakly interacting BEC, roton and maxon modes are dynamically excited by instantaneously switching on the Rydberg-dressed interaction. Through a self-consistent Bogoliubov calculation, we show that the roton and maxon modes leads to non-equilibrium dynamics, where the quantum depletion exhibits slow and fast oscillations. Through analyzing the Bogoliubov spectra, we identify that the slow oscillations correspond to the excitation of the roton modes, while the fast oscillations come from the excitation of the maxon modes. The dependence that these modes have on the quantum depletion in the long time limit is determined analytically and numerically.

In Sec. 3.2 we begin by introducing the Hamiltonian for a 3D Bose gas with both short-range and long-range interactions. The Bogoliubov approximation is explained and we introduce the concept of collective excitations.

In Sec. 3.3, dispersion relations are found using the static Bogoliubov calculation, where roton and maxon modes are identified. We then examine the dynamics of the quantum depletion due to the interaction quench. Excitations of the roton and maxon modes are studied using a self-consistent Bogoliubov method. The asymptotic behavior of the BEC at long times is also explored. The fluctuations within the condensate are discussed alongside the density-density correlation function. We go on to draw comparisons between the interaction induced via Rydberg-dressing, and dipolar BECs. Finally, with Sec. 3.4, we summarise and discuss some implications of our work.

3.2 Hamiltonian of 3D Bose gases and theoretical method

In this section we wish to develop a macroscopic representation for Bose gases. We begin with the construction of the relevant Hamiltonian that will govern the energy of the system. The Bogoliubov spectrum and dynamics for short-range interacting BECs are then explored, to introduce us to the key concepts of the momentum distribution and the quantum depletion.

3.2.1 Hamiltonian

To begin with, let us consider a 3D Bose gas with both short-range and long-range interactions described by the second quantization Hamiltonian (2.28). The Hamiltonian can be expressed as $\hat{H} = \hat{H}_0 + \hat{H}_s + \hat{H}_l$, where $\hat{H}_0$ is the single particle Hamiltonian, $\hat{H}_s$ is the short-range interaction Hamiltonian, and $\hat{H}_l$ is the long-range interaction Hamiltonian. The full form of these Hamiltonian elements are discussed in Chapter 2.

Using the Fourier basis for the field operator

$$\hat{\psi}(\mathbf{r}) = \frac{1}{\sqrt{\Omega}} \sum_k \mathrm{e}^{\mathrm{i}\mathbf{k}\cdot\mathbf{r}} \hat{a}_{\mathbf{k}}, \tag{3.1}$$

where $\hat{a}_{\mathbf{k}}$ is the bosonic annihilation operator acting on a momentum state $\mathbf{k}$ and Ω is the volume of the system, the single particle Hamiltonian is found to be

$$\hat{H}_0 = \frac{1}{\Omega} \int \mathrm{d}\mathbf{r} \sum_{\mathbf{k}_1 \mathbf{k}_2} \hat{a}^\dagger_{\mathbf{k}_1} \mathrm{e}^{-\mathrm{i}\mathbf{k}_1\cdot\mathbf{r}} \left(-\frac{\nabla^2}{2m} - \mu \right) \hat{a}_{\mathbf{k}_2} \mathrm{e}^{\mathrm{i}\mathbf{k}_2\cdot\mathbf{r}} \tag{3.2}$$

$$= \frac{1}{\Omega} \int \mathrm{d}\mathbf{r} \sum_{\mathbf{k}_1 \mathbf{k}_2} \hat{a}^\dagger_{\mathbf{k}_1} \hat{a}_{\mathbf{k}_2} \left(\frac{|\mathbf{k}_2|^2}{2m} - \mu \right) \mathrm{e}^{-\mathrm{i}(\mathbf{k}_1 - \mathbf{k}_2)\cdot\mathbf{r}}, \tag{3.3}$$

where m is the mass of the boson. Using the normalisation requirement that

$\int \mathrm{e}^{\mathrm{i}(\mathbf{k}_l-\mathbf{k}_j)\cdot\mathbf{r}}\,\mathrm{d}\mathbf{r} = \Omega\delta(\mathbf{k}_l-\mathbf{k}_j)$. We arrive at

$$\hat{H}_0 = \sum_{\mathbf{k}}(\epsilon_k-\mu)\hat{a}^\dagger_{\mathbf{k}}\hat{a}_{\mathbf{k}}, \tag{3.4}$$

where $\epsilon_k = |\mathbf{k}|^2/2m$ is the kinetic energy dispersion relation.

Next we can examine the short-range interaction Hamiltonian where we follow a similar substitution approach.

$$\begin{aligned}
\hat{H}_s &= \frac{1}{2\Omega^2}\int\int \mathrm{d}\mathbf{r}\,\mathrm{d}\mathbf{r}'\psi^\dagger(\mathbf{r})\psi^\dagger(\mathbf{r}')U_0\delta(\mathbf{r}-\mathbf{r}')\psi(\mathbf{r})\psi(\mathbf{r}') && (3.5)\\
&= \frac{1}{2\Omega^2}\int \mathrm{d}\mathbf{r}\psi^\dagger(\mathbf{r})\psi^\dagger(\mathbf{r})U_0\psi(\mathbf{r})\psi(\mathbf{r}) && (3.6)\\
&= \frac{U_0}{2\Omega^2}\int \mathrm{d}\mathbf{r}\sum_{\mathbf{k}_1\mathbf{k}_2\mathbf{k}_3\mathbf{k}_4}\hat{a}^\dagger_{\mathbf{k}_1}\hat{a}^\dagger_{\mathbf{k}_2}\hat{a}_{\mathbf{k}_3}\hat{a}_{\mathbf{k}_4}\mathrm{e}^{\mathrm{i}(\mathbf{k}_1-(\mathbf{k}_2-\mathbf{k}_3+\mathbf{k}_4))} && (3.7)\\
&= \frac{U_0}{2\Omega}\sum_{\mathbf{k}_2\mathbf{k}_3\mathbf{k}_4}\hat{a}^\dagger_{\mathbf{k}_2-\mathbf{k}_3+\mathbf{k}_4}\hat{a}^\dagger_{\mathbf{k}_2}\hat{a}_{\mathbf{k}_3}\hat{a}_{\mathbf{k}_4}. && (3.8)
\end{aligned}$$

Defining $\mathbf{k}_4-\mathbf{k}_2 = q$ and adhering to conservation of momentum, we arrive at

$$\hat{H}_s = \frac{U_0}{2\Omega}\sum_{\mathbf{k}\mathbf{k}'\mathbf{q}}\hat{a}^\dagger_{\mathbf{k}+\mathbf{q}}\hat{a}^\dagger_{\mathbf{k}'-\mathbf{q}}\hat{a}_{\mathbf{k}}\hat{a}_{\mathbf{k}'}. \tag{3.9}$$

When we look at the long-range interaction Hamiltonian, we switch to a centre of mass reference frame where we define the vectors $\mathbf{P} = \mathbf{r}-\mathbf{r}'$ and $\mathbf{R} = \frac{\mathbf{r}+\mathbf{r}'}{2}$ which gives

$$\begin{aligned}
\hat{H}_l &= \int\int \frac{\mathrm{d}\mathbf{R}\,\mathrm{d}\mathbf{P}}{2\Omega^2}\sum_{\mathbf{k}_1\mathbf{k}_2\mathbf{k}_3\mathbf{k}_4}\hat{a}^\dagger_{\mathbf{k}_1}\hat{a}^\dagger_{\mathbf{k}_2}\hat{a}_{\mathbf{k}_3}\hat{a}_{\mathbf{k}_4}V(\mathbf{P})\mathrm{e}^{-\mathrm{i}(\mathbf{k}_1-\mathbf{k}_3)\cdot(\mathbf{R}+\frac{\mathbf{P}}{2})}\mathrm{e}^{-\mathrm{i}(\mathbf{k}_2-\mathbf{k}_4)\cdot(\mathbf{R}-\frac{\mathbf{P}}{2})}\\
&= \int\int \frac{\mathrm{d}\mathbf{R}\,\mathrm{d}\mathbf{P}}{2\Omega^2}\sum_{\mathbf{k}_1\mathbf{k}_2\mathbf{k}_3\mathbf{k}_4}\hat{a}^\dagger_{\mathbf{k}_1}\hat{a}^\dagger_{\mathbf{k}_2}\hat{a}_{\mathbf{k}_3}\hat{a}_{\mathbf{k}_4}V(\mathbf{P})\mathrm{e}^{-\mathrm{i}(\frac{1}{2}[\mathbf{k}_1-\mathbf{k}_3-\mathbf{k}_2+\mathbf{k}_4])\cdot\mathbf{P}}\mathrm{e}^{-\mathrm{i}(\mathbf{k}_1-(\mathbf{k}_3-\mathbf{k}_2+\mathbf{k}_4)\cdot\mathbf{R}}\\
&= \int \frac{\mathrm{d}\mathbf{R}}{2\Omega^2}\sum_{\mathbf{k}_1\mathbf{k}_2\mathbf{k}_3\mathbf{k}_4}\hat{a}^\dagger_{\mathbf{k}_1}\hat{a}^\dagger_{\mathbf{k}_2}\hat{a}_{\mathbf{k}_3}\hat{a}_{\mathbf{k}_4}\tilde{V}\left(\frac{1}{2}[\mathbf{k}_1-\mathbf{k}_3-\mathbf{k}_2+\mathbf{k}_4]\right)\mathrm{e}^{-\mathrm{i}(\mathbf{k}_1-(\mathbf{k}_3-\mathbf{k}_2+\mathbf{k}_4)\cdot\mathbf{R}}\\
&= \frac{1}{2\Omega}\sum_{\mathbf{k}_1\mathbf{k}_2\mathbf{k}_3\mathbf{k}_4}\hat{a}^\dagger_{\mathbf{k}_1}\hat{a}^\dagger_{\mathbf{k}_2}\hat{a}_{\mathbf{k}_3}\hat{a}_{\mathbf{k}_4}\tilde{V}\left(\frac{1}{2}[\mathbf{k}_1-\mathbf{k}_3-\mathbf{k}_2+\mathbf{k}_4]\right)\delta_{\mathbf{k}_1,(\mathbf{k}_3-\mathbf{k}_2+\mathbf{k}_4)}\\
&= \frac{1}{2\Omega}\sum_{\mathbf{k}_2\mathbf{k}_3\mathbf{k}_4}\hat{a}^\dagger_{\mathbf{k}_3+\mathbf{k}_4-\mathbf{k}_2}\hat{a}^\dagger_{\mathbf{k}_2}\hat{a}_{\mathbf{k}_3}\hat{a}_{\mathbf{k}_4}\tilde{V}\left(\mathbf{k}_4-\mathbf{k}_2\right). && (3.10)
\end{aligned}$$

Following the same momentum conservation as the short-range Hamiltonian, we arrive at

$$\hat{H}_L = \frac{1}{2\Omega}\sum_{\mathbf{kk'q}} \tilde{V}(\mathbf{q})\hat{a}^\dagger_{\mathbf{k+q}}\hat{a}^\dagger_{\mathbf{k'-q}}\hat{a}_{\mathbf{k}}\hat{a}_{\mathbf{k'}}. \tag{3.11}$$

Combining all three components yields the required form

$$\hat{H} = \sum_{\mathbf{k}}(\epsilon_k - \mu)\hat{a}^\dagger_{\mathbf{k}}\hat{a}_{\mathbf{k}} + \sum_{\mathbf{kk'q}} \frac{g_k}{2\Omega}\hat{a}^\dagger_{\mathbf{k+q}}\hat{a}^\dagger_{\mathbf{k'-q}}\hat{a}_{\mathbf{k}}\hat{a}_{\mathbf{k'}}. \tag{3.12}$$

where for continuity with later sections, we define the nonlocal momentum space interaction as $g_k = \tilde{V}(\mathbf{q}) + U_0$. The operators $\hat{a}_k$ and $\hat{a}^\dagger_k$ obey the standard bosonic commutation relations $[\hat{a}_k, \hat{a}^\dagger_{k'}] = \delta_{k,k'}$.

3.2.2 Bogoliubov approximation

We now return to the statement that for a system at zero temperature, the groundstate is macroscopically occupied as a Bose-Einstein condensate [see Sec. 2.1.1]. In the thermodynamic limit, the expectation value of the number of particles in this state will be given by N_c. With that in mind, and defining $\hat{a}_0 \equiv \hat{a}_{\mathbf{k}=0}$ we can say that

$$\begin{aligned} \hat{a}_0 |N_c\rangle &\approx \sqrt{N_c}\,|N_c\rangle \\ \hat{a}^\dagger_0 |N_c\rangle &\approx \sqrt{N_c}\,|N_c\rangle \end{aligned} \tag{3.13}$$

since for the many-body condensate state, $|N_c\rangle \approx |N_c \pm 1\rangle$. In other words, the macroscopic state of the condensate is so large, that the addition or subtraction of a particle does not change the condensed state. This approach was first used by Bogoliubov [76, 77] in the context of ^{4}He, however, it is now used to explain many aspects of weakly interacting zero temperature physics. The total energy of the system is then given by the Hamiltonian (3.12). We can separate the $\mathbf{k} = 0$

terms, from all terms where $\mathbf{k} \neq 0$ as

$$\begin{aligned}\hat{H} &= (\epsilon_0 - \mu)\,\hat{a}_0^\dagger \hat{a}_0 + \sum_{\mathbf{k}\neq 0} (\epsilon_k - \mu)\,\hat{a}_{\mathbf{k}}^\dagger \hat{a}_{\mathbf{k}} \\ &+ \sum_{\mathbf{k}\mathbf{k}'\mathbf{q}\neq 0} \frac{g_k}{2\Omega}\Big[\hat{a}_{\mathbf{k}+\mathbf{q}}^\dagger \hat{a}_0^\dagger \hat{a}_{\mathbf{k}} \hat{a}_0 + \hat{a}_0^\dagger \hat{a}_{\mathbf{k}'-\mathbf{q}}^\dagger \hat{a}_0 \hat{a}_{\mathbf{k}'} + \hat{a}_{\mathbf{k}+\mathbf{q}}^\dagger \hat{a}_0^\dagger \hat{a}_0 \hat{a}_{\mathbf{k}'} \\ &+ \hat{a}_0^\dagger \hat{a}_{\mathbf{k}'-\mathbf{q}}^\dagger \hat{a}_{\mathbf{k}} \hat{a}_0 + \hat{a}_{\mathbf{k}+\mathbf{q}}^\dagger \hat{a}_{\mathbf{k}'-\mathbf{q}}^\dagger \hat{a}_0 \hat{a}_0 + \hat{a}_0^\dagger \hat{a}_0^\dagger \hat{a}_{\mathbf{k}} \hat{a}_{\mathbf{k}'} + \hat{a}_0^\dagger \hat{a}_0^\dagger \hat{a}_0 \hat{a}_0\Big]. \qquad (3.14)\end{aligned}$$

By then applying the relations (3.13) to the above Hamiltonian and noting that by the argument of conservation of momentum (i.e., $\mathbf{k} = -\mathbf{k}$ and $\mathbf{q} = 0$) we arrive at

$$\hat{H} = \frac{g_k N_c^2}{2\Omega} - \mu + \sum_{\mathbf{k}\neq 0}\left[(\epsilon_k - \mu + 2\hat{a}_{\mathbf{k}}^\dagger \hat{a}_{\mathbf{k}}) + \frac{g_k N_c}{2\Omega}\left(\hat{a}_{\mathbf{k}}^\dagger \hat{a}_{\mathbf{k}'}^\dagger + \hat{a}_{\mathbf{k}} \hat{a}_{\mathbf{k}'}\right)\right] \qquad (3.15)$$

Next, let us consider the fact that the total number of atoms of the system N, which includes the condensate and all occupied excited states, is given as

$$N = N_c + N_D \qquad (3.16)$$

Here N_D is the number of atoms that are *depleted* from the groundstate. We can see that $N_D = \sum_{\mathbf{k}\neq 0} \hat{a}_k^\dagger \hat{a}_k$, meaning that the we have the relations

$$N_c = N - \sum_{\mathbf{k}\neq 0} \hat{a}_k^\dagger \hat{a}_k \qquad (3.17)$$

and

$$N_c^2 = N^2 - 2N \sum_{\mathbf{k}\neq 0} \hat{a}_k^\dagger \hat{a}_k + \mathcal{O}(\hat{a}_{\mathbf{k}}^2), \qquad (3.18)$$

where we have excluded terms of quadratic and higher order. The Hamiltonian can then be expressed self-consistently as

$$\hat{H}_{\mathbf{k}} = E_g + \sum_{\mathbf{k}\neq 0}\left[(\epsilon_k + \frac{g_k N_c}{\Omega})\hat{a}^\dagger_{\mathbf{k}}\hat{a}_{\mathbf{k}} + \frac{g_k N_c}{2\Omega}\left(\hat{a}^\dagger_{\mathbf{k}}\hat{a}^\dagger_{\mathbf{k}'} + \hat{a}_{\mathbf{k}}\hat{a}_{\mathbf{k}'}\right)\right]. \tag{3.19}$$

The ground state energy $E_g = \frac{g_k N^2}{2} - \mu N$ can be neglected from this point in the calculation as it is just a constant energy shift. The Hamiltonian now reads

$$\hat{H}_{\mathbf{k}} = \frac{1}{2}\sum_{\mathbf{k}\neq 0}\left[(\epsilon_k + g_k n_c)(\hat{a}^\dagger_{\mathbf{k}}\hat{a}_{\mathbf{k}} + \hat{a}^\dagger_{-\mathbf{k}}\hat{a}_{-\mathbf{k}}) + g_k n_c(\hat{a}^\dagger_{\mathbf{k}}\hat{a}^\dagger_{-\mathbf{k}} + \hat{a}_{\mathbf{k}}\hat{a}_{-\mathbf{k}})\right], \tag{3.20}$$

where $n_c = N_c/\Omega$ is the density of condensed atoms. The prefactor of $1/2$ comes from separating the momentum states of the kinetic energy terms above and below $\mathbf{k} = 0$. This can be further simplified by performing a canonical transformation on these operators such that they become new operators that act only on momentum states where $\mathbf{k} \neq 0$, as opposed to acting on the ground state of the condensate itself. This is known as the Bogoliubov transformation and can be concisely given as

$$\begin{pmatrix} \hat{a}_{\mathbf{k}} \\ \hat{a}^\dagger_{-\mathbf{k}} \end{pmatrix} = \begin{pmatrix} \bar{u}_{\mathbf{k}} & \bar{v}_{\mathbf{k}} \\ -\bar{v}_{\mathbf{k}} & -\bar{u}_{\mathbf{k}} \end{pmatrix}\begin{pmatrix} \hat{b}_{\mathbf{k}} \\ \hat{b}^\dagger_{-\mathbf{k}} \end{pmatrix}. \tag{3.21}$$

The operator $\hat{b}_{\mathbf{k}}$ is the annihilation operator for quasiparticles above the zero momentum state. These obey the standard bosonic commutation relations $[\hat{b}_{\mathbf{k}}, \hat{b}^\dagger_{\mathbf{k}'}] = \delta_{\mathbf{k},\mathbf{k}'}$, so long as the condition $|\bar{u}_{\mathbf{k}}|^2 - |\bar{v}_{\mathbf{k}}|^2 = 1$ is held. The form of these Bogoliubov amplitudes can be determined by substituting Eq. (3.21) into the effective Hamiltonian (3.20), which gives

$$\begin{aligned} \bar{u}_k &= + \sqrt{\frac{1}{2}\left(\frac{\epsilon_k + g_k n_c}{\bar{E}_k} + 1\right)} \\ \bar{v}_k &= - \sqrt{\frac{1}{2}\left(\frac{\epsilon_k + g_k n_c}{\bar{E}_k} - 1\right)}. \end{aligned} \tag{3.22}$$

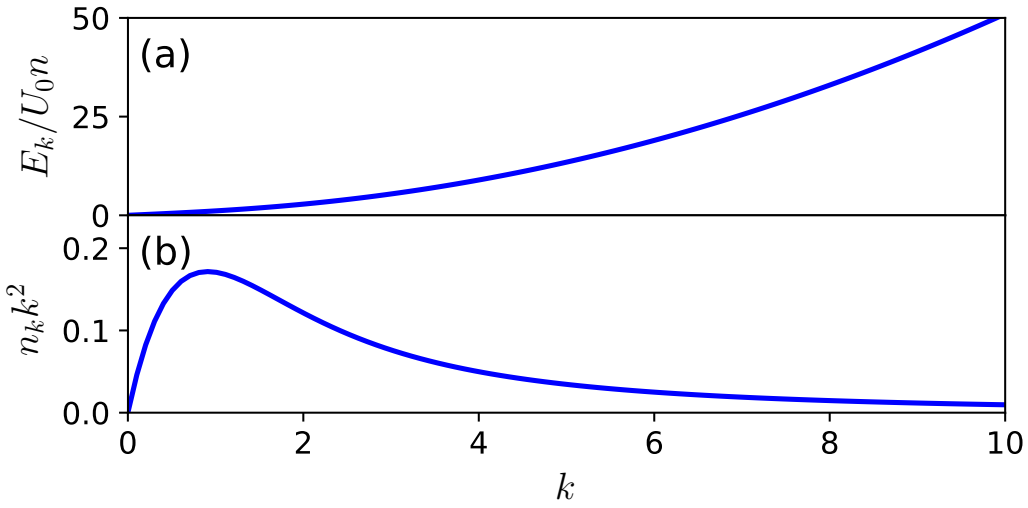

Figure 3.2: ***Bogoliubov excitations and momentum density.*** *(a) The Bogoliubov eigenspectrum is shown as a function of momentum, while the momentum density is shown in (b). Linear phonon modes cause excitations in the momentum of quasiparticles. In this scenario, only short-range interactions are examined, implying that* $\tilde{V}(\mathbf{q}) = 0$.

where

$$\bar{E}_k = \sqrt{\epsilon_k(\epsilon_k + 2g_k n_c)} \tag{3.23}$$

is the Bogoliubov energy eigenspectrum. In this new basis, the Hamiltonian is now diagonal with respect to the quasiparticles and takes the form

$$\hat{H}_{\mathrm{B}} = \sum_{\mathbf{k}\neq 0} \bar{E}_k \hat{b}^\dagger_{\mathbf{k}} \hat{b}_{\mathbf{k}}. \tag{3.24}$$

3.2.3 Elementary excitations

The total particle density in the system is given as $n = n_c + \sum_{\mathbf{k}\neq 0} \hat{a}^\dagger_{\mathbf{k}} \hat{a}_{\mathbf{k}}/\Omega$, assuming a fixed atom number in the system. Here, in the basis of Bogoliubov quasiparticles, this expands as

$$n = n_c + \sum_{\mathbf{k}\neq 0} |v_k|^2 + \sum_{\mathbf{k}\neq 0} (|u_k|^2 + |v_k|^2) \hat{b}^\dagger_{\mathbf{k}} \hat{b}_{\mathbf{k}}. \tag{3.25}$$

This means that when a particle with non-zero momentum is created, the total number of condensate atoms must decrease. A powerful outcome of this is that there is always loss of atoms from the condensate in an interacting Bose gas. These are known as elementary excitations and their distribution of momentum values can be mapped by evaluating the groundstate expectation value

$$n_k = \langle \hat{a}^\dagger_{\mathbf{k}} \hat{a}_{\mathbf{k}} \rangle = |v_k|^2. \tag{3.26}$$

Let us assume that atom-atom interactions are s-wave in nature, and therefore are controlled by Eq.(2.12), meaning that $g_k \equiv U_0$. We can plot the Bogoliubov excitation spectrum $\bar{E}_k$ [Fig. 3.2(a)] and the momentum density $n_k k^2$ [Fig. 3.2(b)]. The momentum density can be used to more easily visualise the density of excited states. For this section the momentum is scaled by the condensate coherence length $\zeta = (mU_0 n)^{1/2}$, such that $k \equiv k\zeta$. For small values of k, $\bar{E}_k$ is linear, meaning that these amount to low energy phonon modes. At larger values of k, the dispersion becomes quadratic.

The total density of excited particles is called the *quantum depletion* of the con-

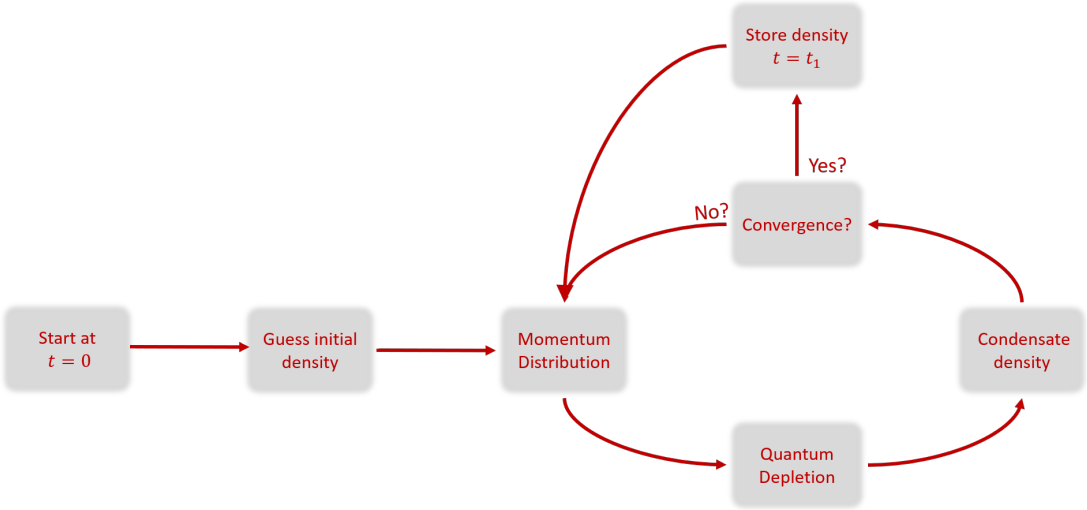

Figure 3.3: ***Self-consistent Bogoliubov Algorithm.*** *The algorithm is laid out for the reader. An initial guess of the condensate density is used to calculate the quantum depletion. If the corresponding density is equal to the initial guess, the density is stored and the simulation moves onto the next time step.*

densate and is given by

$$n_d = \frac{1}{\Omega}\sum_{\mathbf{k}\neq 0} n_k, \tag{3.27}$$

The quantum depletion is the summation of all the nonzero momentum states that are under the curve in Fig. 3.2(b). This means the condensate fraction is simply given by

$$n_c = n - n_d. \tag{3.28}$$

When the interactions are limited to short-range contact interactions, the quantum depletion can be found analytically to be

$$n_d = \frac{8(a_s n_c)^{3/2}}{3\sqrt{\pi}}. \tag{3.29}$$

For a system with very weak interactions the depletion will be small, meaning the condensate fraction will remain fixed near $n_c \approx n$. However, when we increase the value of U_0 the total depletion begins to rapidly rise, leading to substantial loss of the condensate [see Fig. 3.4].

This raises an issue however. The excitation spectrum and momentum distribution depend on n_c. This means to be completely accurate, we must calculate the depletion self-consistently [64], using an iterative algorithm [see Fig. 3.3]. At $t = 0$ we begin with an initial guess of the density. This is used to calculate the momentum distribution of the atoms; integration then provides the quantum depletion, and therefore yields the density. This is iterated until the input density is the same as the output density. Once a consistent result is found, we move to the next time-step. This method is crucial in the coming chapter. 3.4. For stronger interactions, this self-consistent method is vital in calculating the correct quantum depletion.

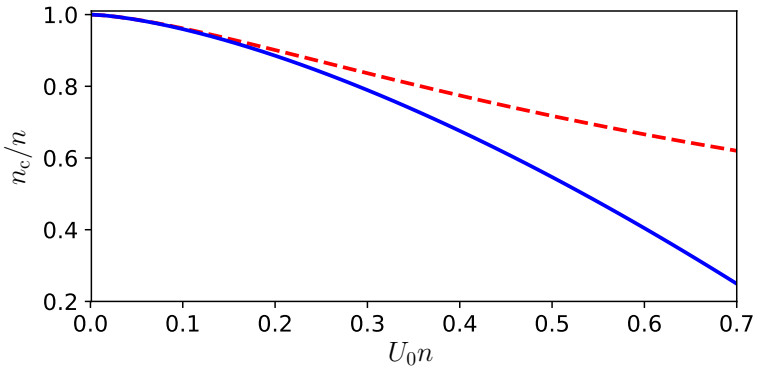

Figure 3.4: ***Condensate fraction vs interaction strength.*** *The blue curve shows the depletion assuming $n_c = n$. This is in stark contrast to the self-consistent calculation given by the red curve. As with 3.2, we only examine the short-range interacting scenario.*

3.2.4 Hamiltonian of the Rydberg-dressed BEC

We consider a uniform 3D Bose gas of N atoms that interact through both s-wave and soft-core interactions, described by the second quantization Hamiltonian $\hat{H} = \hat{H}_0 + \hat{H}_s + \hat{H}_l$ [see Chapter 2]. The interaction potential is described by $V(\mathbf{r}-\mathbf{r}') = U_0\delta(\mathbf{r}-\mathbf{r}') + \Lambda(\mathbf{r}-\mathbf{r}')$. Using the method described in the previous section, the Hamiltonian in a momentum basis is given by Eq. (3.12), where the Fourier transformation of the atomic interaction $\tilde{g}(\mathbf{r}-\mathbf{r}')$ is now given by $g_k = U_0 + \tilde{\Lambda}(k)$. Here we have replaced the generic long-range interaction with the soft-core interaction, introduced in Sec 2.2.2.

$\tilde{\Lambda}(k)$ is the Fourier transformation of the soft-core potential where $\tilde{\Lambda}(k) = \lambda_0 f(k)$. $\Lambda_0 = C_0/R^6$ determines the strength and $f(k)$ has an analytical form

$$f(k) = \frac{2\pi^2 \mathrm{e}^{-\frac{kR}{2}}}{3kR}\left[\mathrm{e}^{-\frac{kR}{2}} - 2\sin\left(\frac{\pi}{6} - \frac{\sqrt{3}kR}{2}\right)\right], \tag{3.30}$$

which characterizes the momentum dependence of the interaction. Though the interaction is repulsive in real space, i.e. $\Lambda(\mathbf{r}-\mathbf{r}') > 0$, it contains negative regions in momentum space, as shown in Fig. 3.1(b). The negative part of $\tilde{\Lambda}(k)$ appears at momentum around $kR \sim 5\pi/3$. Previously, it was shown that the attractive interaction in momentum space is crucially important to the formation of roton instabilities when employing a Bogoliubov approximation on such a system [71], as is the case with the coming sections.

3.2.5 Self-consistent Bogoliubov approach for the quench dynamics

The quench of the soft-core interaction consists of two steps. The system is initially in the ground state of a weakly interacting BEC, i.e. $\Lambda_0 = 0$ when $t \leq 0$. At time $t > 0$ the Rydberg dressing is switched on immediately. The scheme is depicted in Fig. 3.1(c). The time dependence of the atomic interaction

is described by a piecewise function as follows,

$$g_k = \begin{cases} U_0 & \text{when } t \leq 0 \\ U_0 + \Lambda_0 f(k) & \text{when } t > 0. \end{cases} \tag{3.31}$$

We assume that the s-wave interaction is not affected during the quench. Hence we use parameter $\alpha = \Lambda_0/U_0$ to characterize the strength of the soft-core interaction with respect to the s-wave interaction.

A time-dependent Bogoliubov approach is applied to study the dynamics induced by the interaction quench. It is an extension of the conventional Bogoliubov approximation from Sec. 3.2.2, where the canonical transformation becomes time-dependent, $\hat{a}_{\mathbf{k}\neq 0}(t) = u_k(t)\hat{b}_{\mathbf{k}} - v_k(t)^*\hat{b}^\dagger_{-\mathbf{k}}$ where $u_k(t)$ and $v_k(t)$ are time-dependent amplitudes with the relation $|u_k(t)|^2 - |v_k(t)|^2 = 1$, which preserves the bosonic commutation relation. This approach has been widely used to study excitation dynamics in BECs with or without long-range interactions [56–58, 62, 64]. It provides a good approximation when the condensate has not undergone significant depletion.

Using the Heisenberg equation for the bosonic operators, we obtain equations of motion of $u_k(t)$ and $v_k(t)$,

$$i \begin{bmatrix} \dot{u}_k(t) \\ \dot{v}_k(t) \end{bmatrix} = \begin{bmatrix} \epsilon_k + g_k n_c(t) & g_k n_c(t) \\ -g_k n_c(t) & -\epsilon_k - g_k n_c(t) \end{bmatrix} \begin{bmatrix} u_k(t) \\ v_k(t) \end{bmatrix}, \tag{3.32}$$

where $n_{\mathrm{c}}(t)$ is the time-dependent condensate density. The total density consists of the condensate and depletion densities as $n = n_c(t) + n_d(t)$ with the total density of the excitation, i.e. quantum depletion given as

$$n_d(t) = \frac{1}{\Omega}\sum_{\mathbf{k}} n_k(t), \tag{3.33}$$

where $n_k(t) \equiv \langle \hat{a}^\dagger_{\mathbf{k}}\hat{a}_{\mathbf{k}}\rangle = |v_{\mathrm{k}}(t)|^2$ is the distribution of all possible momentum states.

For a particle conserving system, both the depleted density and the condensate density are time dependent. In practice, the quantum depletion as a function of time is difficult to calculate, as the differential equations (3.32) become non-autonomous. Here we will apply the self-consistent procedure as used in Sec. 3.2.2. First, we force the pre-quench density to be the total density, meaning $n_c(0) = n$, i.e. assuming that the non-condensed occupation is negligible. This is a valid assumption so long as the s-wave interaction is weak. The evolution of coefficients $u_k(t)$ and $v_k(t)$ depends on the dispersion relation $E_k(t) = \sqrt{\epsilon_k[\epsilon_k + 2g_k n_c(t)]}$, which is assumed to change adiabatically with time through the condensate density $n_c(t)$.

Eqs. (3.32) are solved exactly, yielding solutions

$$\begin{aligned}\begin{bmatrix} u_k(t) \\ v_k(t) \end{bmatrix} &= \left[\cos(E_k(t)t)\mathbb{I} - \mathrm{i}\frac{\sin(E_k(t)t)}{E_k(t)}\right. \\ &\times \left.\begin{pmatrix} \epsilon_k + g_k n_c(t) & g_k n_c(t) \\ -g_k n_c(t) & -\epsilon_k - g_k n_c(t) \end{pmatrix}\right] \begin{bmatrix} u_k(0) \\ v_k(0) \end{bmatrix},\end{aligned} \tag{3.34}$$

where $\mathbb{I}$ is the identity matrix, and the initial values of $u_k(t)$ and $v_k(t)$ are [9],

$$\begin{aligned} u_k(0) &= \sqrt{\frac{1}{2}\left[\frac{\epsilon_k + U_0 n}{E_k(0)} + 1\right]} \\ v_k(0) &= -\sqrt{\frac{1}{2}\left[\frac{\epsilon_k + U_0 n}{E_k(0)} - 1\right]}. \end{aligned} \tag{3.35}$$

We can then calculate the momentum distribution function as

$$n_k(t) = |v_k(0)|^2 + g_k n_c(t)\left[g_k n_c(t) - U_0 n\right]\frac{\epsilon_k\left[1 - \cos(2E_k(t)t)\right]}{2E_k(t)^2 E_k(0)}. \tag{3.36}$$

Taking into account all of the momentum components, the quantum depletion is

evaluated through,

$$n_d(t) = \frac{1}{2\pi^2} \int_0^\infty n_k(t) k^2 \, \mathrm{d}k, \tag{3.37}$$

where we have replaced the summation by the integration over momentum space. The angular part in the integration has been integrated out in the above equation. With the quantum depletion at hand, the condensate fraction is found to be $n_c(t) = n - n_d(t)$. We then reinsert the result back into Eq. (3.36) and iterate the procedure until the calculation converges self-consistently.

In the following calculations, we will scale the energies, lengths, and times with respect to the interaction energy $U_0 n$, coherence length $\zeta = (m U_0 n)^{-1/2}$, and coherence time $\tau = t U_0 n$ of the initial condensate. The zero range interaction strength is fixed by the s-wave scattering length, which is set to $a_\mathrm{s} = 0.1 n^{-1/3}$ throughout this chapter.

3.3 Results and discussions

3.3.1 Stationary dispersion relation

The soft-core interaction drastically alters the dispersion relation of the Bogoliubov excitations. To illustrate this, we first examine dispersion relations of a static BEC by assuming that the soft-core interaction is present. When the soft-core interaction is weak, i.e. α is small, the dispersion relation resembles that of a weakly interacting BEC. To do this, we utilise the stationary dispersion relation, given by Eq. (3.23). The excitation energies increase monotonically with momentum k [9] [see Fig. 3.5(a)]. By increasing α, the shape of the Bogoliubov spectra changes significantly. A local maximum and minimum can be seen in the dispersion relation [Fig. 3.5(a)]. At the maximum, special modes called maxon modes form, while roton modes emerge around the minima [71]. In the following, we will denote the energies of the maxons and rotons with γ_m and γ_r, as the local

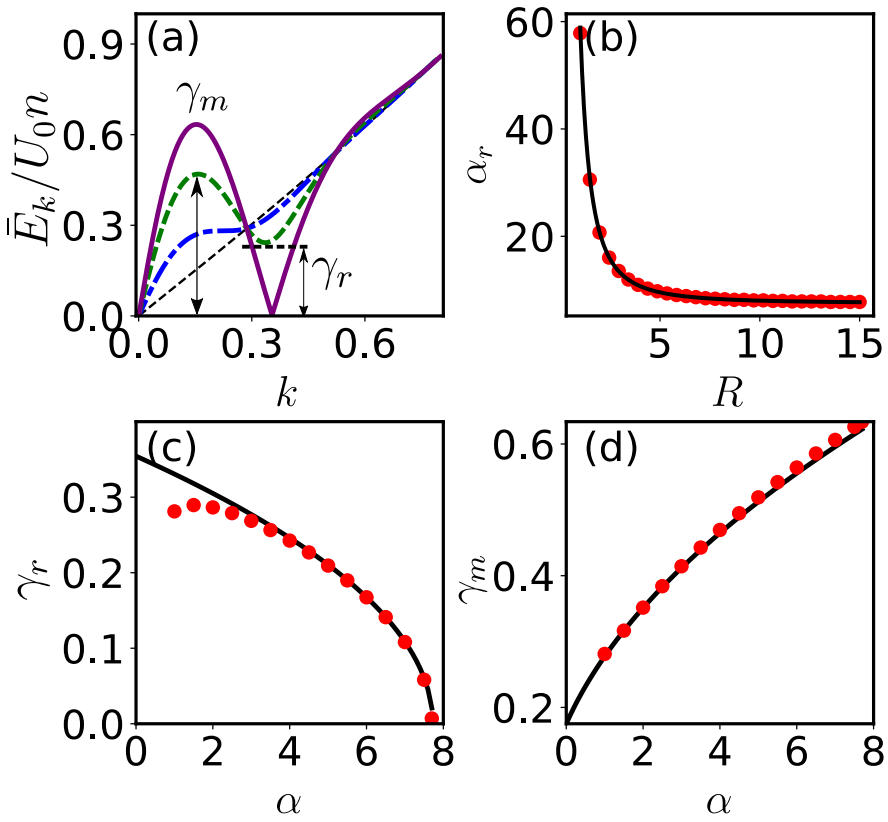

Figure 3.5: ***Roton and maxon mode****. (a) Bogoliubov spectra in the stationary state for $\alpha = 0$ (black dashed), 1 (blue dot-dashed), 6 (green dashed), and 7.7 (solid purple), when $R = 15$. The energy gaps γ_r and γ_m indicating respectively the roton and maxon energies are marked for the green curve. For $\alpha > 7.7$, the spectrum becomes unstable. (b) The critical value α_r vs R. Analytical calculations (black) agree with the numerical data (red dots). (c) Roton energy γ_r. Increasing α, the roton energy decreases. For large α, the analytical (black solid) and numerical (dot) results agree. At small α, roton minima become weak and eventually disappear, which leads to the deviation. The data points in red are the energies taken numerically from the dispersion. (d) Maxon energy γ_m increases with α. The analytical (black solid) and numerical data agree nicely. In (c) and (d) $R = 15$.*

maximal and minimal values of the dispersion relation.

The roton and maxon modes depend on the soft-core interaction non-trivially. When increasing α, γ_r decreases while γ_m increases, as given by the examples shown in Fig. 3.5(a). For sufficiently large α, the roton gap vanishes as the energies become complex, i.e. the roton is unstable. The roton instability can drive the system out of a uniform condensate, leading to the formation of supersolids [27, 78, 79]. It should be noted that the instability here is induced

by stronger, isotropic interactions. In dipolar BECs, instabilities are caused by angular dependent interactions [66].

It is important to obtain the critical value at which the roton mode becomes unstable. From Fig. 3.1(b), the Fourier transform of the soft-core potential has the most negative value around $k_r \approx 5\pi/3R$. The roton minimum takes place around this momentum. By substituting k_r into the dispersion relation, we can identify the critical α at which the roton energy becomes complex,

$$\alpha_r = \frac{5\mathrm{e}^{5\pi/3}\left(36R^2+25\pi^2\right)}{72\pi R^2\left[2\mathrm{e}^{5\pi/6}\sin\left(\frac{\pi}{6}-\frac{5\pi}{2\sqrt{3}}\right)-1\right]}. \tag{3.38}$$

To check the accuracy of this critical value, we numerically find the instability point from the dispersion relation for various α values. Both numerical and analytical values are shown in Fig. 3.5(b). The analytical result agrees with the numerical values very well. This supports the assumption that the roton minimum happens around momentum k_r.

Knowing the momentum k_r, we can obtain the roton energies by inserting it into Eq. (3.23). It is found that the roton energy γ_r decreases with increasing α [see Fig. 3.5(c)]. The roton energy from the numerical calculations agrees with the analytical data, especially when the soft-core interaction is strong. Decreasing the soft-core interaction, the roton modes disappear for sufficiently small α, as our numerical calculations indicate. We notice large deviations between the two methods in this regime.

On the other hand, the location of the maxon modes in momentum space is difficult to find. By analyzing the dispersion relation, the momentum corresponding to the maxon mode is approximately given by $k_m \approx k_r/2$. Using this approximation, we substitute this momentum value into Eq. (3.23) and calculate the maxon energy. The result is shown in Fig. 3.5(d), where the approximate value matches the numerical values with a high degree of accuracy.

Recently, the stationary state of 2D and 3D Rydberg-dressed BECs have been

examined [80]. It was shown that the increased occupation around the roton modes leads to instabilities in the groundstate in the form of density waves. It was also seen that the strong interparticle interactions lead to a large depletion of the condensate.

3.3.2 Roton and maxon excitation

Depending on parameters of the soft-core interaction, the stationary dispersion relation could support roton and maxon modes. One example is displayed in Fig. 3.6(a). Now if we quench the interaction, the dispersion relations of the initial and final states are different. The system is driven out of equilibrium, such that the momentum distributions $n_k(\tau)$ evolve with time. In Fig 3.6(b), snapshots of the momentum density $n_k(\tau)k^2$ are shown. At $\tau = 0$, the BEC is in a stationary state, which depends on the initial condition, $\bar{v}_k$. The respective momentum density is a smooth function of k. At later times, different momentum components are excited by the presence of the soft-core interaction. The appearance of the maxon modes can be seen in the momentum density as the boundary between the phonon modes oscillating, and the dip in the excited momentum density. This additional occupation causes exotic dynamics of the quantum depletion.

The dynamics of the quantum depletion depends vitally on the parameter R and α in the soft-core interaction. After switching on the interaction, the excitation of the Bogoliubov modes significantly affects the momentum distribution. We will first investigate the oscillatory behavior of the quantum depletion. For moderate soft-core interactions, many momentum modes are excited by the soft-core interaction, as shown in Fig. 3.6(b). As a result, the quantum depletion increases rapidly with time, and then oscillates around a constant value [Fig. 3.6(c)]. The Fourier transformation $\tilde{n}_d(\nu)$ of the quantum depletion, characterizes the spectra of the dynamics, shows a sharp peak [Fig. 3.6(d)]. The peak's position, i.e. the frequency of the oscillation, decreases gradually when increasing the soft-core radius.

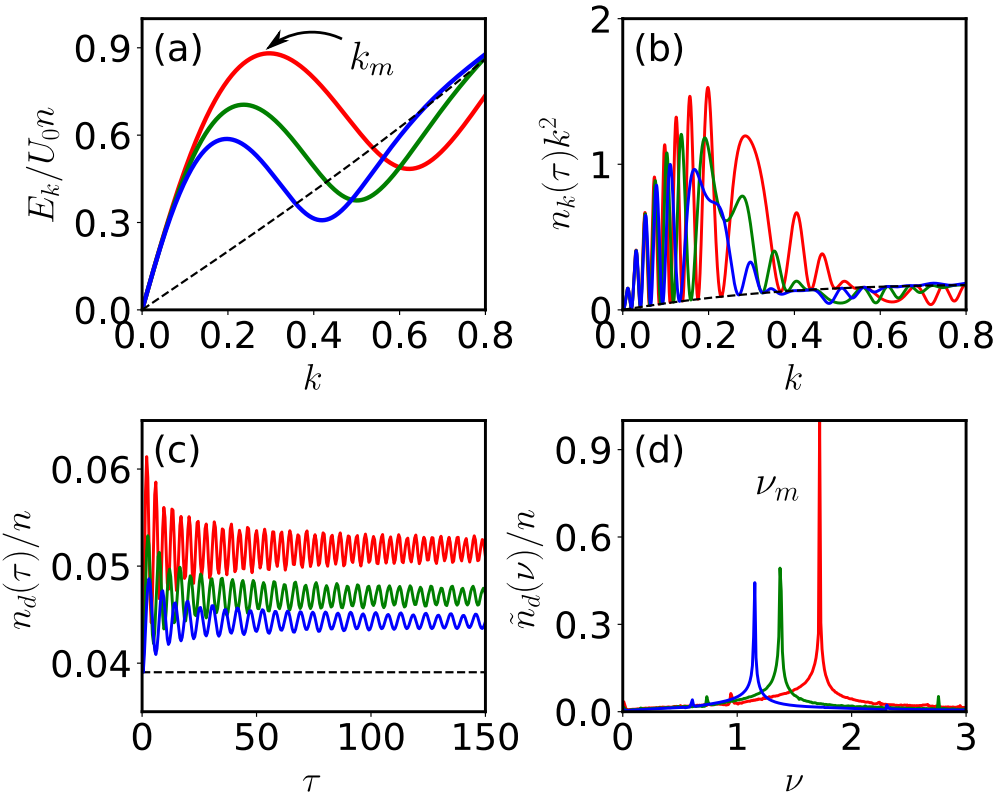

Figure 3.6: ***Excitation of the roton and maxon mode, with changing soft-core interaction.*** *In(a) the dispersion for a static BEC is given. The momentum of the roton and maxon modes decreases with increasing soft-core radius R. Without soft-core interactions, the excitation energy monotonically increases with momentum (dashed). The location of the maxon modes for the red curve is highlighted it the arrow. In (b)-(c), the interaction quench is applied. Momentum densities $n_k k^2$ at time $\tau = 30$ are shown in (b). The black dashed curve shows the momentum distribution of the initial state. Fast oscillations are found in the quantum depletion (c), which leads to sharp peaks in the respective Fourier transformation (d) The non-zero width of the peaks results from the simulation running over a finite time. The frequency ν_{m} at the major peaks is determined by the maxon frequency. Minor peaks corresponding to other frequencies are almost invisible. For the above, three different soft-core radius $R = 8$ (red), 10 (green), and 12 (blue) are considered, while the interaction strength is fixed at $\alpha = 4$.*

For stronger soft-core interactions, the roton mode moves towards the instability point [see Fig. 3.7(a)]. In this case, higher momentum components can be excited during the interaction quench [Fig. 3.7(b)]. As the interaction strength approaches α_{r}, the momentum density develops a large occupation at momentum values matching k_{r}. Exact maxon momenta again prove elusive to find. However, we instead see that the phonon modes matching the linear momentum values in the excitation spectra are excited in a similar linear-like fashion up to the

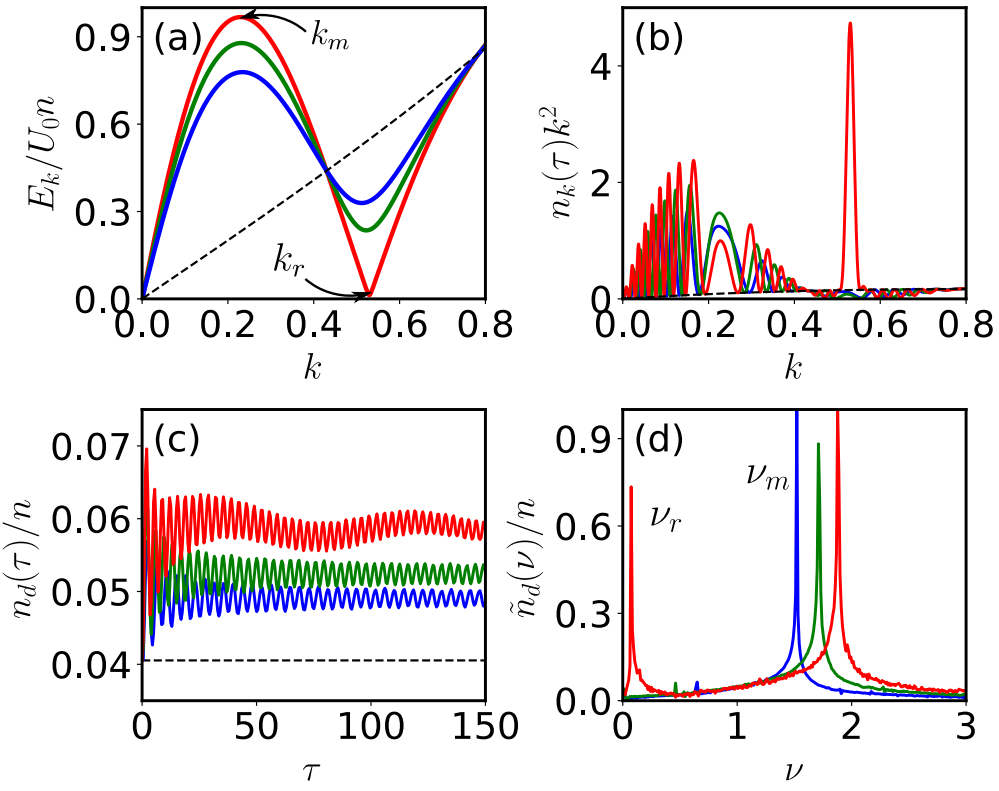

Figure 3.7: ***Excitation of the roton and maxon mode, with changing interaction strength.*** *The dispersion (a), momentum distribution (b), quantum depletion (c) and Fourier transformation of the quantum depletion (d) for* $R = 10$ *and* $\alpha = 5$ *(blue),* 6.5 *(green), and* 7.99 *(red) are shown. Approaching to the roton instability, the momentum density distribution develops a large occupation around modes at* k_r *at* $\tau = 30$*. Both the roton and maxon momenta are highlighted with arrows. The depletion dynamics maintains a slower oscillation as the interaction strength is increased, which can be seen from the Fourier transformation of the quantum depletion. The lower peak frequency* ν_{r} *is determined by the roton mode. The major peaks at higher frequencies are due to the excitation of maxons. When* $\alpha = 7.99$*, both the roton and maxon mode are dynamically stable, giving narrow Fourier spectra.*

expected value of k_{m}, as shown.

In this case, a new, lower frequency pattern develops on top of the fast oscillation in the quantum depletion [Fig. 3.7(c)]. This changes the Fourier spectra of the quantum depletion, where a new peak is found at a lower frequency [Fig. 3.7(d)]. It is important that the peak positions in $\tilde{n}_d(\nu)$ are determined by the roton and maxon energies. In the quantum depletion, the fast oscillations are due to the excitations of the maxon modes, while slow oscillations are due to the roton modes. To verify this, we first obtain the maxon and roton frequencies by substituting the corresponding momentum k_{m} and k_{r} into Eq. (3.23). We then

compare them with the frequency at the peak positions in the Fourier spectra. Note that the oscillation frequency (i.e. peak frequency of the Fourier spectra) in the quantum depletion is twice the Bogoliubov energy, as can be seen in Eq. (3.36). As shown in Fig. 3.8, the numerical data for both the maxon mode (a-b) and roton mode (c-d) agree with the analytical calculations. When varying the interaction strength, the maxon (roton) frequency increases (decreases) with increasing α. If we increase the soft-core radius, frequencies of both modes decrease.

The agreement between numerical and analytical calculation confirm that both roton and maxon modes are excited via quenching the soft-core interaction. The dynamically excited modes are stable, as both the fast and slow oscillations are *persistent* for a long time. In our numerical simulations, the oscillations will not dampen even when the simulation time $\tau > 1000$. Such persistent oscillatory dynamics also leads to the sharp peaks in the Fourier transformation of the quantum depletion.

We want to emphasize that the quench dynamics in the dressed BEC is in sharp contrast to BECs with either s-wave or dipolar interactions. In a weakly interacting BEC, the quantum depletion grows exponentially to a steady value $\propto \zeta^{-\frac{1}{3}}$, while oscillatory patterns are not present in the depletion [57], due to the fact that low energy phonon modes dominate the quench dynamics. In dipolar BECs [64, 68, 72, 81, 82], on the other hand, roton modes are formed due to the interplay between long-range dipolar and s-wave interactions [64, 68, 72, 81, 82]. These roton modes can be excited by quenching the dipolar interaction, while maxon modes are typically unstable in the dynamics. This will be explored in Sec. 3.3.6.

3.3.3 Quantum depletion in the long time limit

In the long time limit $\tau \gg 1$, the quantum depletion oscillates rapidly around a mean value [Fig. 3.6(c) and 3.7(c)]. In the following, we will evaluate the asymptotic mean value of the quantum depletion. First we will derive an analytic

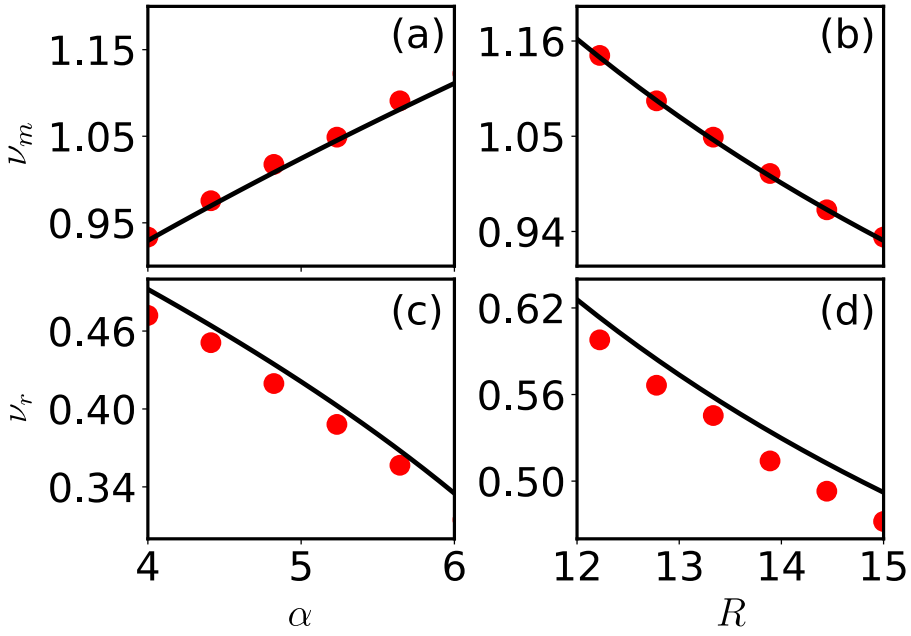

Figure 3.8: ***Maxon frequency (a-b) and roton frequency (c-d).*** *The dots are numerical data from the Fourier spectra. The solid curves are the analytical results* $2\gamma_{\mathrm{m}}$ *in (a)-(b) and* $2\gamma_{\mathrm{r}}$ *in (c)-(d) obtained from the Bogoliubov dispersion. The maxon (roton) frequency increases (decreases) with increasing interaction strength. At the critical point* α_{r}*, the roton mode loses stability. Frequencies of both modes tends towards* 0 *for larger* R *values as the soft-core interaction becomes weaker. In (a) and (c)* $R = 15$*. In (b) and (d)* $\alpha = 4$*.*

expression using the following approximations. In the long time limit, the time averaged quantum depletion is largely determined by the low momentum modes. Moreover, we will neglect the oscillation term in Eq. (3.36), as they are related to the roton and maxons. Using these approximations, the asymptotic form of the momentum distribution n_k^∞ is obtained,

$$n_k^\infty \approx \frac{1}{2}\left(\frac{k^2+1}{\sqrt{k^2(k^2+4)}} - 1\right) + \frac{\alpha f(k)}{4k}\frac{n_c^\infty}{n}, \tag{3.39}$$

where n_{c}^∞ is the asymptotic condensate density. After carrying out the integral over momentum space, the approximate quantum depletion when $\tau \to \infty$ is obtained,

$$\frac{n_{\mathrm{d}}^\infty}{n} \approx 2\Gamma\left(\frac{R^2+\alpha\pi}{3R^2+2\pi\alpha\Gamma}\right), \tag{3.40}$$

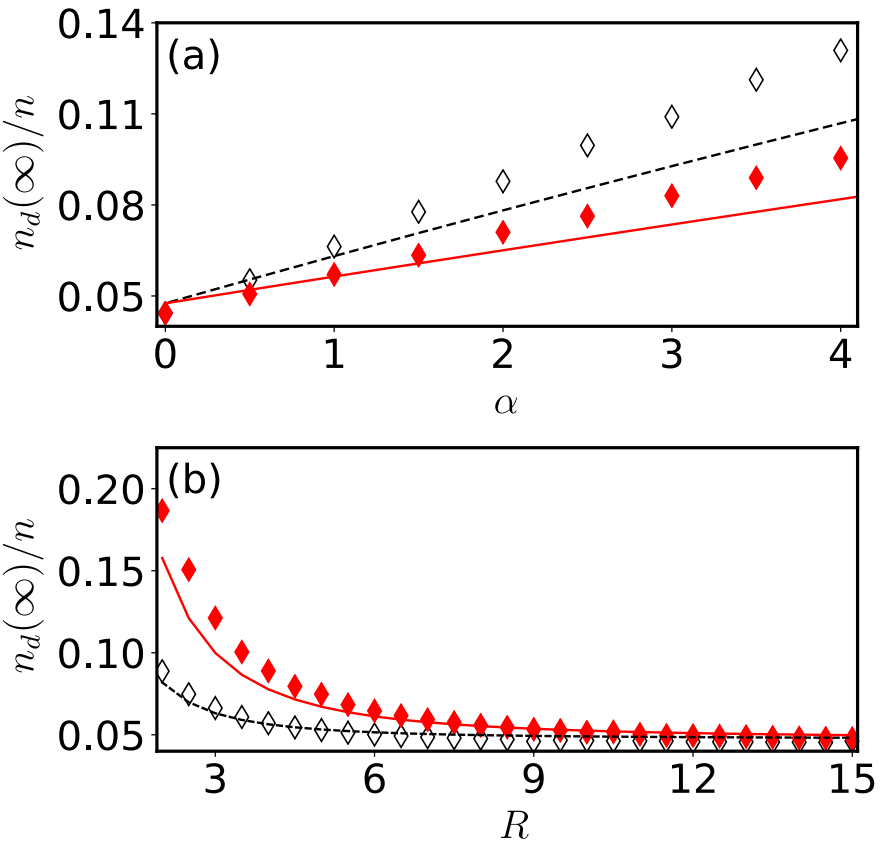

Figure 3.9: ***Asymptotic quantum depletion.*** *The asymptotic quantum depletion increases with increasing α (a), which is seen from both the analytical and numerical calculations. The quantum depletion n_d^∞ decreases with increasing soft-core radius (b). The solid line is found analytically using Eq. (3.40), while the data points are found by numerically solving Eq. (3.37) and taking the mean value at later times between $\tau \approx 50 \to 150$. Parameters in (a) are $R = 3$ (open black) and 4 (solid red). Parameters in (b) are $\alpha = 1$ (open black) and 3.5 (solid red).*

where $\Gamma = (2\pi^2\zeta^3 n)^{-1}$. This result predicts that the quantum depletion approaches a constant value $n_d^\infty/n \to 2\Gamma/3$ in the limit $R \to \infty$. This resembles the result of the weakly interacting BEC, i.e. the soft-core interactions plays no role in the dynamics. To verify the analytical calculation, we numerically find the mean value of the quantum depletion when time is large. Both the numerical and analytical results are shown in Fig. 3.9. For small α, low momentum states are populated by switching on the soft-core interaction. This is the regime where the approximation works. Here we find a good agreement between the numerical and analytical calculations. Increasing the interaction strength, more and more higher momentum components are populated [see Fig. 3.7(b)], causing larger de-

pletion. A clear deviation between the numerical and analytical data is found, as the approximations we made in evaluating Eq. (3.40) become less accurate. On the other hand, the quantum depletion becomes smaller by increasing the soft-core radius, as the strength of the soft-core interaction reduces. In this case the numerical and analytical results agree well [see Fig. 3.9(b)].

3.3.4 Condensate fluctuation

In this section, we evaluate the fluctuation of the condensate for the Rydberg-dressed BEC. The condensate fluctuation is defined as

$$\begin{aligned}\Delta n_c &= \sqrt{\langle n_c^2\rangle - \langle n_c\rangle^2} \\ &= \sqrt{\langle n_d^2\rangle - \langle n_d\rangle^2} \\ &= \frac{1}{\Omega}\sqrt{\sum_{\mathbf{k}\mathbf{k}'\neq 0}\left[\langle \hat{a}^\dagger_{\mathbf{k}}\hat{a}_{\mathbf{k}}\hat{a}^\dagger_{\mathbf{k}'}\hat{a}_{\mathbf{k}'}\rangle - \langle \hat{a}^\dagger_{\mathbf{k}}\hat{a}_{\mathbf{k}}\rangle\langle \hat{a}^\dagger_{\mathbf{k}'}\hat{a}_{\mathbf{k}'}\rangle\right]},\end{aligned}$$

where we have assumed the total density n is a constant. Using the Bogoliubov transformation, the fluctuation of the condensate is obtained,

$$\Delta n_{\mathrm{c}} = \frac{1}{\Omega}\sqrt{2\sum_{\mathbf{k}\neq 0} n_k(1+n_k)} \tag{3.41}$$

One can numerically evaluate the fluctuation by inserting Eq. (3.36) into the above equation. For convenience, the relative fluctuation, $\sqrt{N}\Delta n_{\mathrm{c}}/n$, will be calculated. Some examples are shown in Fig. 3.10(a). The fluctuation increases rapidly, and then saturates at an asymptotic value when time is large. The fluctuation oscillates around the asymptotic value. The maxon modes lead to fast oscillations. When the roton mode is significantly populated, a slower oscillation is found.

The asymptotic value of the fluctuation depends on the soft-core interaction. Increasing α, the asymptotic value increases [see Fig. 3.10(a) and (b)]. We can estimate the asymptotic value of the density fluctuation by replacing n_k with its

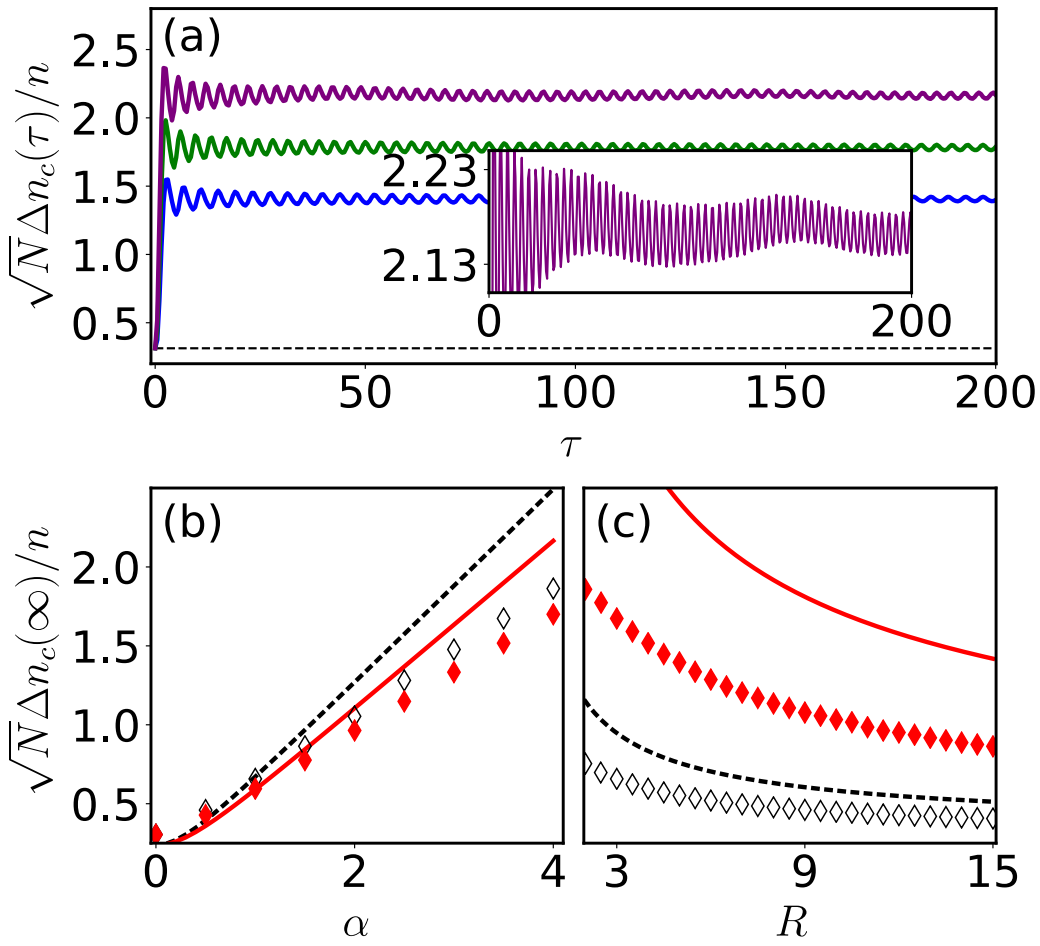

Figure 3.10: ***Condensate fluctuation.*** *(a) Dynamics of the condensate fluctuation. We fix $R = 10$, and evolve the system for $\alpha = 5$ (blue), 6.5 (green), and 7.99 (purple). The dashed line is the fluctuation without the soft-core interaction, i.e. $\alpha = 0$. The inset shows fluctuations when $\alpha = 7.99$ to highlight the low frequency oscillations due to rotons. The axes of the inset is same as panel (a). Mean values of the fluctuations for different α (b) and R (c) when time $\tau \to \infty$ are shown. We have considered $R = 3$ (open black) and 4 (solid red) in (b) and $\alpha = 1$ (open black) and 3.5 (solid red) in (c). Other parameters can be found in Fig. 3.9 in the main text.*

asymptotic value Eq. (3.39), in Eq. (3.41), which yields

$$\frac{\sqrt{N}\Delta n_c^{\infty}}{n} = \sqrt{2\Gamma \int_0^{\infty} n_k^{\infty}\left[1 + n_k^{\infty}\right] k^2 \, \mathrm{d}k}. \tag{3.42}$$

Further assuming the fluctuation depends solely on low momentum states, we

obtain the approximate result of the fluctuation when $\tau \to \infty$,

$$\frac{\sqrt{N}\Delta n_c^{\infty}}{n} \approx \sqrt{\frac{2\Gamma\pi^2\left[1+\pi^2\alpha\left(6\sqrt{3}+\pi\alpha C\right)\right]}{27R}}, \tag{3.43}$$

with the constant $C = \left[4\sqrt{3}\pi - 3\log\left(\frac{27}{16}\right)\right]$. The approximation result shows that fluctuations of the condensate decreases (increases) with increasing R (α). In Fig. 3.10(b) and (c), numerical and approximate results are both shown. The two calculations agree when α is small or R is large, where the depletion and fluctuation are both small. Though large discrepancy is found when α is large or R is small, the trend found from both numerical and analytical calculations are the same.

3.3.5 Density-density Correlation

Lastly we evaluate the density-density correlation function [56, 57]

$$g^{(2)}(\mathbf{r},t) = \sum_{\mathbf{k},\mathbf{k}',\mathbf{q}} e^{i\mathbf{k}.\mathbf{r}}\frac{1}{\Omega^2}\left\langle \hat{a}^{\dagger}_{\mathbf{k}+\mathbf{q}}(t)\hat{a}_{\mathbf{k}}(t)\hat{a}^{\dagger}_{\mathbf{k}'-\mathbf{q}}(t)\hat{a}_{\mathbf{k}'}(t)\right\rangle . \tag{3.44}$$

Within the Bogoliubov transformation, this can then be expressed in terms of the condensate density as $\langle 1/\Omega^2 \sum_{\mathbf{k},\mathbf{k}'} \hat{a}^{\dagger}_{\mathbf{k}+\mathbf{q}}(t)\hat{a}_{\mathbf{k}}(t)\hat{a}^{\dagger}_{\mathbf{k}'-\mathbf{q}}(t)\hat{a}_{\mathbf{k}'}(t)\rangle = n^2 + n/\Omega \sum_{\mathbf{k}}[4|v_k|^2 - u_k^* v_k - u_k v_k^*]$. Defining $D = |\mathbf{r}-\mathbf{r}'|/\zeta$ as the scaled interatomic distance, the correlation function is given as [57]

$$g^{(2)}(D,\tau) - 1 = \frac{4\Gamma}{D}\int_0^{\infty} k\,\mathrm{d}k \sin(kD)\left[n_k - \mathrm{Re}[u_k^*(\tau)v_k(\tau)]\right]. \tag{3.45}$$

The first term is the correlations that develop between condensed atoms while the second term describes the correlations between the condensate and excited states. We see from Fig. 3.11(a) that the correlations immediately develop both slow and fast oscillations. The slow oscillation corresponds to the excitation of roton

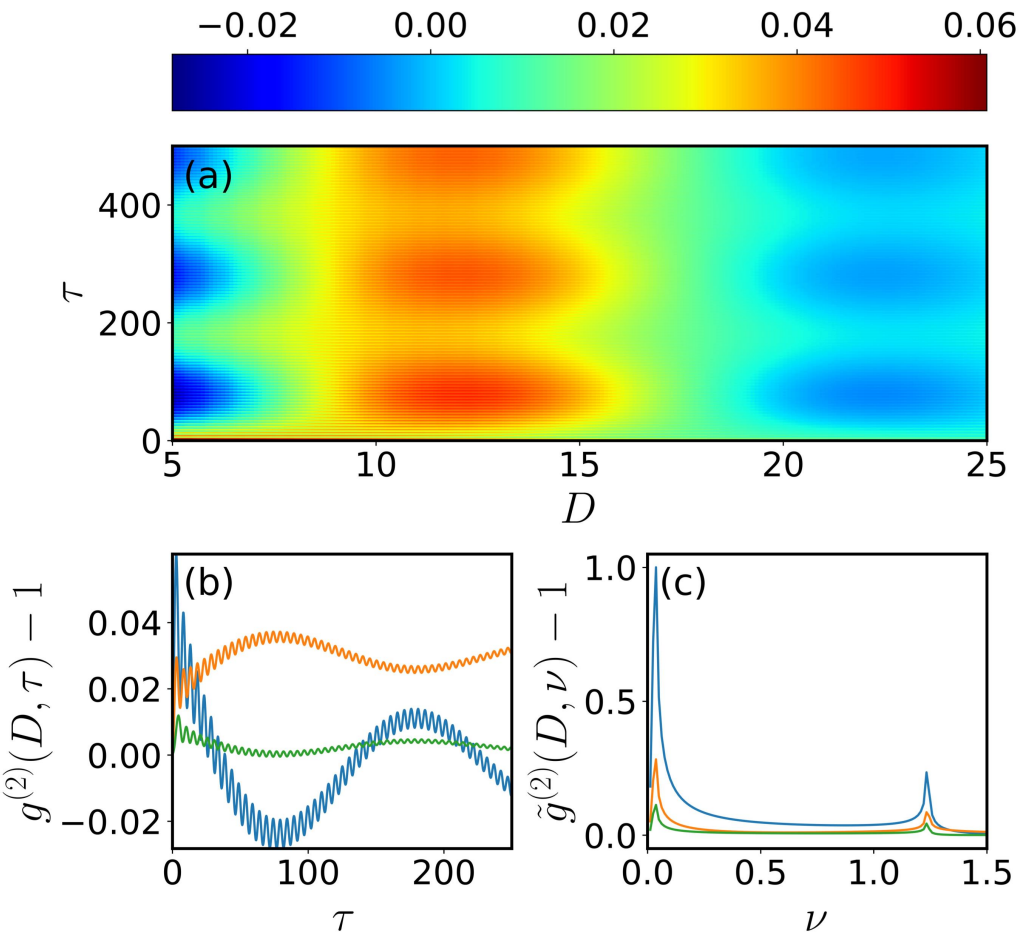

Figure 3.11: ***Density-density correlation.*** *(a) The density-density correlations as a function of D and τ, when $R = 15$ and $\alpha = 7.7$. Correlations at $D = 5$ (blue), 15 (orange), and 25 (green) are shown in (b). The corresponding Fourier spectrum of the correlation function is shown in (c). In the Fourier spectra, the peaks at lower and higher frequencies are due to the excitation of roton and maxon modes.*

modes, when γ_r is small. The fast oscillations attributed to the maxon occupation are more easily observed when looking at a specific value of D [Fig. 3.11(b)]. The corresponding Fourier transformation $\tilde{g}^{(2)}(D,\nu) - 1$ clearly show the associated frequency peaks. When the distance $D < R$, $g^{(2)}(D,\tau) - 1$ oscillates with large amplitudes and can have negative values, i.e. strong repulsive interactions lead to anti-correlations. The correlations are seen to increase in amplitude in this regime. Around the soft-core radius, the correlations are positive, and reach their maximal values, after which they begin to decrease with D. The formation of the roton minima inhibits larger scale correlations from developing.

3.3.6 Dynamics of two dimensional dipolar systems

Quench dynamics in BECs with dipolar interactions are drastically different. The dipolar interaction is given by

$$\tilde{V}_{\rm dd}(\mathbf{r}-\mathbf{r}') \;=\; g_0\delta(\mathbf{r}) + \frac{d^2}{|\mathbf{r}-\mathbf{r}'|^3}[1-3\cos^2(\theta)], \tag{3.46}$$

where d is the dipole moment, θ is the angle between the dipoles and molecular axis, and g_0 is the short-range contact interaction as before. In 3D, the Fourier transform of the dipolar interaction has no momentum dependence [68]. In a 2D trapped dipolar Bose gas [65, 67], the interaction potential displays a strong momentum dependence [64].

We consider a quasi-2D setup [64], where a strong confinement is applied in the perpendicular z-direction while leaving atoms free to move in the $x-y$ plane. The dipoles are polarized along this z-axis. This leads the axial confinement as l_z, which provides a natural rescaling of $\mathbf{r} \mapsto \mathbf{r}/l_z$ [64, 65, 67, 69, 70]. After integrating Eq. (3.46) in the z-axis, we obtain the Fourier transformation of the quasi-2D dipolar interaction [64]

$$g_{\rm dd}(k) = g_0 + d^2\left[2 - 3k\sqrt{\pi}\mathrm{Erfc}(k)\mathrm{e}^{k^2}\right], \tag{3.47}$$

where $\mathrm{Erfc}(k)$ is the complimentary error function. Here we define the dimensionless parameter $\alpha_d = d^2/g_0$ to characterizing the strength of the dipolar interaction, such that the interaction after the quench is given as $g_{\rm dd}(k)/g_0 = 1 + \alpha_d\left[2 - 3k\sqrt{\pi}\mathrm{Erfc}(k)\mathrm{e}^{k^2}\right]$. The quench scheme for the dipolar case is similar to the procedure outlined in the main text. We switch on the dipolar interaction instantaneously, while keeping the s-wave interaction unchanged.

The dispersion relation for the dipolar BEC is shown in Fig. 3.12(a), where both roton and maxon modes can be seen.

When the dipolar interaction is compared to the Rydberg-dressed BEC [e.g Fig. 3.5(a)], the energies of the low momentum modes remain small, as seen by directly

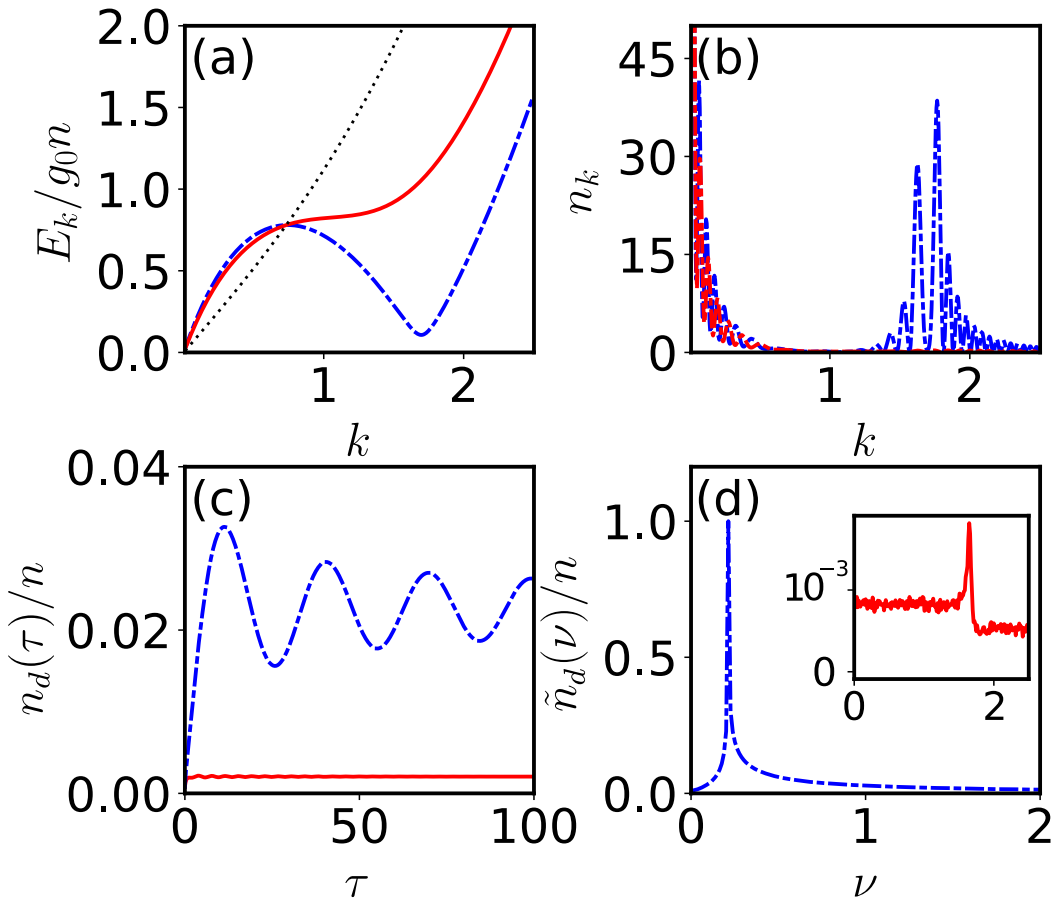

Figure 3.12: ***Quantum depletion in a dipolar BEC.*** *Red curves are for* $\alpha_{\rm d} = 2.1$ *and blue curves are for* $\alpha_d = 2.7$*. The axial confinement is set to* $l_z = 0.1n^{-1/2}$*. We show the dispersion relation in (a) while the momentum distribution at time* $\tau = 30$ *is shown for (b). The quantum depletion and corresponding Fourier spectra are shown in (c) and (d) respectively. The inset shows a maxon mode is excited for* $\alpha_{\rm d} = 2.1$*. However the signal is very weak and almost invisible. The axes of the inset is same as panel (d).*

comparing the dispersion relations. The absence of these large maxon energies means that the mechanism behind the dipolar interactions prevent the oscillations that we previously attributed to the maxon modes from reaching large amplitudes [Fig. 3.12(b)][64, 69, 83].

We follow the same self-consistent process to obtain the condensate fraction. We calculate the quantum depletion as before as $n_{\rm d}/n = 1/(2\pi l_z^2 n)\int_0^\infty n_k k\,{\rm d}k$. When $\alpha_{\rm d}$ is small, the dynamics develops maxon oscillations, which dampens in short time scales, as shown in Fig. 3.12(c). When $\alpha_{\rm d}$ is large, the roton frequency completely overpowers the maxon frequency in the dynamics. The absence of a

stable maxon mode is also seen in the Fourier spectra [Fig. 3.12(d)].

3.3.7 Baliaev dampening

A minor subtlety is the fact that the maxon modes are found at a local maximum of the dispersion relation. This should imply that maxons are inherently unstable due to the energetically favoured roton modes. What we can show however is that, at least qualitatively, this decay channel is closed leading to the stable maxon modes. We can explain this in what follows [69, 84, 85].

For a 3D Bose gas, the dispersion relation can be expanded (up to third-order in momentum) as

$$E_k \approx ck + bk^2 + dk^3 + \mathcal{O}[k^4] \tag{3.48}$$

As pointed out by Maris [85], it is possible for quasiparticles, with momentum $\mathbf{k}$ to decay into two phonon modes, if and only if, both energy and momentum conservation is conserved. For this, the energy of $\mathbf{k}$ must lie above the phonon dispersion energy ($E_p = ck$).

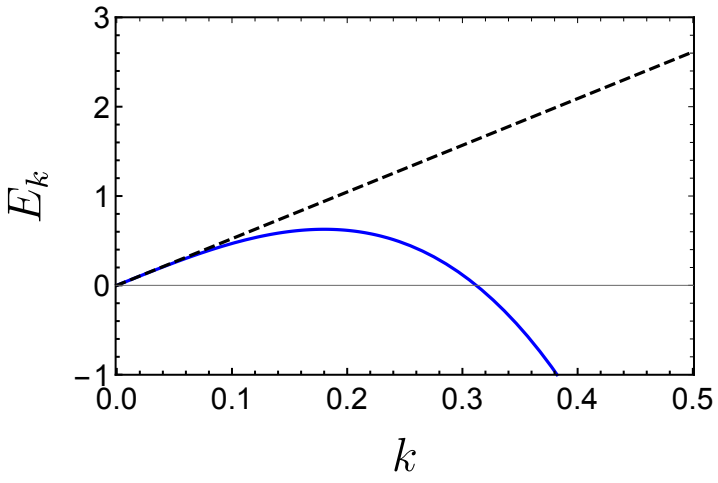

Figure 3.13: ***Taylor Expansion of Rydberg-dressed BEC phonon modes.*** *Black-dashed curves show the phonon component of the Rydberg-dressed condensate. The red curve is that of the coefficients of the quadratic momentum components. The parameters used are* $\alpha = 4$ *and* $R = 8$

For the Rydberg-dressed interaction, the dispersion is given by

$$E_k^{rd} \approx c_{rd}k \left[1 + k^2 \frac{9 - 8n_c\pi^2 R^2 \alpha}{72g_0 n_c + 48n_c\pi\alpha}\right] + \mathcal{O}[k^4], \tag{3.49}$$

where the phonon velocity is

$$c_{rd} = \sqrt{\frac{(2\pi^2\alpha + 3g_0)\, n_c}{3}}. \tag{3.50}$$

As can be seen in Fig. 3.13, the dispersion has no quadratic component at low momenta. We see that the dispersion bends downwards as we increase the momentum value. This means that a maxon cannot decay into a two photons. This explains why the maxon modes are stable for Rydberg-dressed BECs.

In comparison, we can also calculate the phonon velocity for the dipolar BEC [69, 84]. The expanded dispersion in this case is given by

$$E_k^{dd} \approx c_d k \left[1 - \frac{3\sqrt{\pi} n_c \alpha_d^2}{2c_d} k + \frac{n_c^2 \alpha_d \left(\frac{2+g_0}{n_c} + 24g_0 + 48 - 9\pi\right) k^2}{8c_d^4} + \mathcal{O}[k^3]\right] \tag{3.51}$$

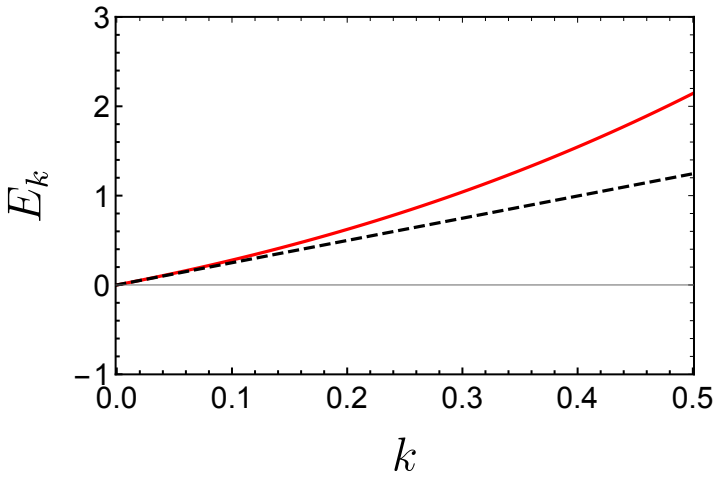

Figure 3.14: ***Taylor Expansion of Dipolar BEC phonon modes.*** *In this example, the quadratic dispersion beaches the linear phonon modes, meaning that this decay channel is open.*

with a phonon velocity

$$c_d = \sqrt{n_c \left(g_0 + 2\alpha_d\right)} \tag{3.52}$$

3.4 Summary and discussion

We have studied dynamics of 3D BECs in free space, with Rydberg-dressed soft-core interactions. An interaction quench is implemented through turning on the soft-core interaction instantaneously, starting from a weakly interacting BEC. The Bogoliubov spectrum of the BEC displays local maxima and minima, which are identified as maxon and roton modes. Through a time-dependent Bogoliubov approach, we have calculated dynamics of the quantum depletion self-consistently. Our results show that both roton and maxon modes are excited by switching on the soft-core interaction. The excitation of roton and maxon modes generate slow and fast oscillatory dynamics in the quantum depletion. Our simulations show that the excited roton and maxon modes are stable in the presence of the soft-core interaction, which are observed from the persistent oscillations of the quantum depletion. We have found the frequencies of the roton and maxon modes approximately, which are confirmed by the numerical simulations.

Our study shows that exotic roton and maxon excitations can be created in Rydberg-dressed BECs through the interaction quench. Properties of the maxons and rotons can also been seen from condensate fluctuations and density-density correlations. Additionally we briefly explained some reasoning as to why the Rydberg-dressed interactions produce stable maxon modes, a feature not seen in its dipolar counterpart. The results studied in this work might be useful in identifying the soft-core interaction, through measuring the frequencies and strength of the quantum depletion. In the future, it is worth studying the formation of droplets and spatial patterns in Rydberg-dressed BECs, which could be affected by the presence of roton or maxon modes.

Chapter 4

Nonlinear dynamics of Rydberg-dressed Bose-Einstein condensates in a triple-well potential

This chapter is the first of two that studies the dynamics of Rydberg-dressed Bose-Einstein condensates trapped in a triple-well potential in the semiclassical limit. The Rydberg-dressed BECs experience a long-range soft-core interaction, giving rise to strong nearest and next-nearest neighbor interactions in the triple-well system. Using mean-field Gross-Pitaevskii equations [see Chapter 2], we show that lower branches of the eigenspectra exhibit loops and level-crossings when the soft-core interaction is strong. The direct level-crossings eliminate the possibility of adiabatic Landau-Zener transitions when tilting of the triple-well potential. We demonstrate that the long-range interaction allows for self-trapping in one, two, or three wells, in a far more controllable manner than BECs with short-range or dipolar interactions. Exact quantum simulations of the three-well Bose-Hubbard model indicate that self-trapping and nonadiabatic transition can be observed with less than a dozen bosons. Our study is relevant to current

research into collective excitation and nonlinear dynamics of Rydberg-dressed atoms. Several sections of the following chapter have been transcribed verbatim, along with the accompanying data and figures, from the following publication:

"Nonlinear dynamics of Rydberg-dressed Bose-Einstein condensates in a triple-well potential"

G. McCormack, R. Nath, and W. Li

Physical Review A: **102** 063329 (2020) [86]

4.1 Introduction

The understanding of the dynamics of interacting Bose-Einstein condensates has been a fruitful field of research in the past three decades [6, 9, 51, 87–89]. With modern experimental techniques that allow for controlling properties of ultracold atomic gases, such as atom-atom interactions [90], trapping potentials and spatial dimensions [91–93], along with long coherence times [94], stationary and dynamical properties of atomic BECs have been explored in great detail [51]. The dynamics of trapped atomic BECs are typically described by the mean-field, Gross-Pitaevskii equation [90, 95, 96], with which many interesting properties and novel dynamics have been revealed [43, 97–104]. In optical lattices [2], bosons can undergo the well-known superfluid-Mott insulator transition [105]. It has been proposed that BECs [106–108] and atoms trapped in optical lattices [109] can be used for carrying out quantum computation.

Substantial work has also been carried out in finite-sized double-well and triple-well potentials. For technical specifications see Chapter 4.2. In the quantum regime, the dynamics of atoms in double well potentials are affected by the on-site (short-range) interactions, causing wave-packet collapse and revivals [110]. In the semiclassical regime, strong onsite interactions introduce interesting nonlinear effects. One striking feature is that the eigenspectrum of the nonlinear

system develops a loop structure due to strong onsite interactions [111, 112]. Chapter 4.2 discusses these in great detail. The loop causes the breakdown of the adiabatic theorem and self-trapping dynamics, which has been examined experimentally [113, 114]. In triple-well configurations, static and dynamical properties depend on boundary conditions and spatial profiles of two-body interactions. With closed boundaries and bare onsite interactions [115–117], multiple loop structures are found in the spectra of the coupled nonlinear system. These complicated spectra lead to turbulent phase spaces [118–120] and produce oscillatory dynamics beyond the typical Josephson or self-trapping behavior [115, 116, 121]. Population transfer between energy levels has been found via Landau-Zener tunneling [115, 118, 119]. Additionally, resonance generation within a triple-well was explored [122]. Ring-shaped triple-well setups (i.e. periodic boundary conditions) have also been examined, in which eigenenergies intersect even for the noninteracting case [123].

When long-range dipolar interactions are present, the dynamics of BECs are changed dramatically in triple-well potentials. The ground state shows exotic behavior, such as mesoscopic quantum superpositions [124] and macroscopic first-order coherence between the outer sites [125]. Recently, quantum population [126] and entanglement [127] dynamics of dipolar BECs in triple wells have also been examined. However, dipolar interactions decay rapidly with distance r as r^{-3}, which leads to weak nearest-neighbor and much weaker next-nearest-neighbor interactions in a triple-well potential.

Long-range interactions can be realized alternatively by means of Rydberg-dressing. In contrast with the previous chapter, here we are motivated by a number of theoretical studies on the static and dynamical properties of Rydberg-dressed atoms confined in traps [23, 24, 47, 50, 128–130] and optical lattices [19, 30, 45, 131–134]. In this chapter, we study BECs interacting with long-range soft-core interactions trapped in a triple-well potential [see Fig. 4.1]. A key feature is that the long-range Rydberg-dressed interaction allows us to explore dynamics in a regime

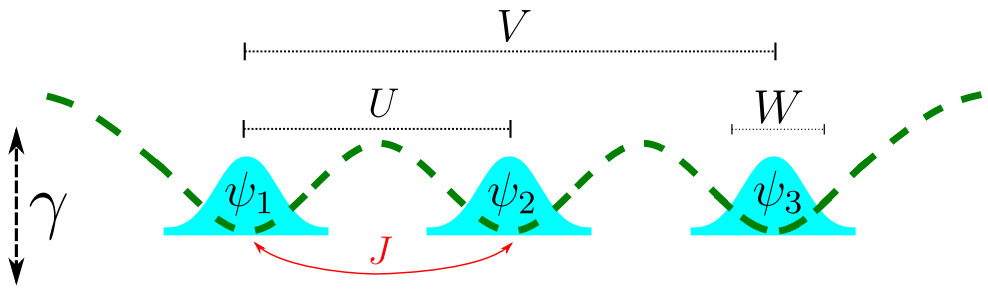

Figure 4.1: *Schematic of a triple-well lattice potential. The potential height (zero-point energy) γ of each trap may be adjusted dynamically. Atoms may interact via onsite (W), nearest (U) or next-nearest (V) neighbour interactions, while the tunneling J is restricted to nearest-neighbor sites, forming a chain setup.*

where nearest-neighbor and next-nearest-neighbor interactions are strong, due to the large soft-core radius. When the traps are tilted, the system undergoes nonadiabatic Landau-Zener transitions due to complicated loops and level-crossings on the lower branches of the eigenspectra. This results in dynamical instability and hence leads to the breakdown of the adiabatic theorem. This is in stark contrast to systems with short-range interactions, where tunneling from the ground state is not prevented from adiabatic population dynamics, as the level-crossings emerge in the higher energy branches [see Section 4.2]. By tuning the profile of Rydberg-dressed interactions, we can also control self-trapping of BECs [92, 135] to a high degree of accuracy, which is typically difficult if considering only onsite interactions. We propose that the nonlocal interactions allow for precise manipulation of the final states, such that we can control whether the trapping is localized in a one, two, or even all three wells simultaneously. We also carry out simulations of the quantum dynamics which takes into account the inter-well correlations. The comparison with the mean-field results show that the transporting dynamics can be found in mesoscopic systems with tens of atoms.

The chapter is organized as follows. We begin by discussing the mean field dynamics of coupled BECs with two and three potential wells. This provides us with a gateway to discussing relevant physics, such as adiabatic Landau-Zener transitions and self-trapping. In Sec. 4.3 the Hamiltonian of the Rydberg-dressed system is introduced. The corresponding mean-field approximation is presented

and the resulting equations of motion are given. We examine the eigenspectrum and discuss new features in our system. In Sec 4.4, we explore nonadiabatic transitions for both weak and strong nonlinear interactions. The Landau-Zener transition probability is also examined. By analysing the Poincaré sections for different energy values, we show that the system can move towards highly chaotic regions when the nonlinear interactions are strong. We then examine self-trapping of bosons in different sites. The dynamics depend on initial conditions and long-range interactions. We moreover compare the mean-field results to quantum dynamics. We summarise and discuss some implications of our work in Sec. 4.5.

4.2 Multi-well BECs with short-range mean-field interactions

It is common in the study of quantum systems to consider only a small, finite number of energy levels, that have strong coupling strengths between each level. As such, a natural extension to a uniform Bose gas is coupling multiple condensates in a single system. In this section we discuss the concepts of Landau-Zener transitions between neighbouring states (sites). We then discuss the nonlinear dynamics that develop where there are onsite and offsite density-density interactions present.

4.2.1 Landau-Zener transitions

A particularly interesting phenomenon for two isolated neighbouring states is that of Landau-Zener (LZ) transitions. Energy spectrum anti- and avoided-level crossings have since been well described since their inception by Laudau and Zener in 1932 [136, 137].

Adiabatic theorem

Landau-Zener population transfer between states arises by means of the adiabatic theorem of quantum mechanics, which states that eigenstates of a system remain as instantaneous eigenstates when the system is slowly varied with respect to the level spacing.

Suppose that a state $\psi_n(t)$ is found, such that the following eigenvalue equation is satisfied

$$H(t)\left|\psi_n(t)\right\rangle = \epsilon_n(t)\left|\psi_n(t)\right\rangle . \tag{4.1}$$

Then $\psi_n(t)$ is an instantaneous eigenstate for the time-dependent $\mathcal{Q}\times\mathcal{Q}$ Hamiltonian $H(t)$, for $n = 1, 2, 3, ..., \mathcal{Q}$. The corresponding energies are therefore $\epsilon_n(t)$. However, it should be made clear that, in general, an instantaneous eigenstate is not a solution to the time-dependent Schrödinger equation

$$i\frac{\mathrm{d}}{\mathrm{d}t}\left|\Psi(t)\right\rangle = H(t)\Psi(t). \tag{4.2}$$

The relationship between $\psi(t)$ and $\Psi(t)$, the solution to the Schrödinger equation, is not trivial. What should be clear from the adiabatic theorem however is that if at time $t = 0$, the true eigenstate is $\left|\Psi(0)\right\rangle = \left|\psi_n(0)\right\rangle$, then the Hamiltonian $H(t)$ must be varying slowly in time. Meaning that for an arbitrary time τ, $0 \leq t \leq \tau$, the true eigenstate of the Schrödinger equation will remain $\left|\Psi(\tau)\right\rangle \approx \left|\psi_n(\tau)\right\rangle$, up to a global phase factor. This means that population transfers between energy states are highly suppressed.

While the global phase is irrelevant to any dynamics seen, the relative phase factors between the instantaneous eigenstates are not. This means that for

$$\left|\Psi(t)\right\rangle = \sum_{n=1}^{\mathcal{Q}} c_n(t)\left|\psi_n(t)\right\rangle \tag{4.3}$$

the time evolution of the phases $c_n(t)$ will matter.

Acting the Schrödinger equation onto Eq. (4.3) gives

$$i\sum_{n=1}^{\mathcal{Q}}\left(\dot{c}_n\left|\psi_n(t)\right\rangle + c_n|\dot{\psi_n}(t)\rangle\right) = \sum_{n=1}^{\mathcal{Q}} c_n(t)\epsilon_n(t)\left|\psi_n(t)\right\rangle. \tag{4.4}$$

Then we can act $\langle\psi_m(t)|$ onto the above equation, $m \neq n$, to yield

$$i\dot{c}_m = \left(\epsilon_m - i\left\langle\psi_m(t)|\dot{\psi_m}(t)\right\rangle c_m(t) - i\sum_{m\neq n}\left\langle\psi_m(t)|\dot{\psi_n}(t)\right\rangle c_n(t)\right). \tag{4.5}$$

The term $\langle\psi_m(t)|\dot{\psi_n}(t)\rangle$ can be related to a matrix element of the time-dependent Hamiltonian in the space of instantaneous eigenstates by first taking the time derivate of Eq. (4.1), which gives

$$\dot{H}(t)\left|\psi_n(t)\right\rangle + H(t)|\dot{\psi_n}(t)\rangle = \dot{\epsilon}_n(t)\left|\psi_n(t)\right\rangle + \epsilon_n(t)|\dot{\psi_n}(t)\rangle. \tag{4.6}$$

Again acting with $\langle\psi_m(t)|$, and with a bit of algebra we arrive at

$$\left\langle\psi_m(t)|\dot{\psi_n}(t)\right\rangle = \frac{\dot{H}_{m,n}}{\epsilon_n - \epsilon_m}, \tag{4.7}$$

where $\dot{H}_{m,n}$ is the derivative of a matrix element of the time-dependent Hamiltonian. Plugging this result back into Eq. (4.5) we get

$$i\dot{c}_m = \left(\epsilon_m - i\left\langle\psi_m(t)|\dot{\psi_m}(t)\right\rangle c_m(t) - i\sum_{m\neq n}\frac{\dot{H}_{m,n}}{\epsilon_n - \epsilon_m}c_n(t)\right). \tag{4.8}$$

If the final term vanishes, it can be shown that $|c_m| = 1$, meaning that $\psi_n(t) = \psi_n(\tau)$. Finally, by ignoring this last term we can see that

$$c_m(t) = c_m(0)\mathrm{e}^{-i\int_o^t \epsilon_m(t')\,\mathrm{d}t'}\mathrm{e}^{-\int_o^t\left\langle\psi_m(t)|\dot{\psi_n}(t)\right\rangle\mathrm{d}t'}. \tag{4.9}$$

From this we can see that final state depends not only on dynamical phase, but also on a geometric phase; linking adiabatic processes with Berry phases [138, 139].

Avoided-level crossings

We imagine a two state system, separated by an energy gap 2γ. The states are coupled via the parameter J. The Schrödinger equation for ψ_1 and ψ_2 is

$$i\frac{\mathrm{d}}{\mathrm{d}t}\begin{pmatrix}\psi_1\\ \psi_2\end{pmatrix} = H(t)\begin{pmatrix}\psi_1\\ \psi_2\end{pmatrix}, \tag{4.10}$$

where the time-dependent Hamiltonian is

$$H(t) = \begin{bmatrix}\gamma(t) & -J\\ -J & -\gamma(t)\end{bmatrix} \tag{4.11}$$

One finds that the corresponding eigenvalues for the Hamiltonian above are

$$\epsilon = \pm\sqrt{\gamma^2 + J^2} \tag{4.12}$$

As is illustrated in Fig. 4.2, the smaller the parameter J, the smaller the gap between the energy levels becomes, $2J$ for $J = 0$. Now let us return to the statement that this level bias γ is a time varying quantity. For simplicity we assume it is linear in time as $\gamma = \alpha t$, where α is a rate parameter, governing how

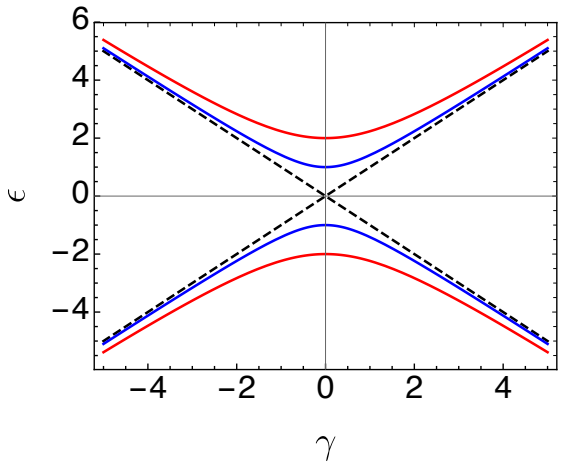

Figure 4.2: ***Eigenenergies as a function of level bias.*** *The energies are plotted as a function of the level bias γ for $J = 0$ (black dashed) , $J = 1$ (blue), and $J = 2$(red). As the hopping amplitude decreases, the distance between the upper and lower branch of the spectrum closes to* 0.

fast the levels move past each other.

For a sufficiently large gap, the adiabatic theorem [111] says that the time evolution of the original energy eigenstate will remain an energy eigenstate of the changing Hamiltonian so long as this gap value is comparable to $\sqrt{\alpha}$. If not, we expect that other states will be excited by a quench in γ.

Landau-Zener transition formula

We now calculate the population transfer between the states ψ_1 and ψ_2. From Eq. (4.10), we get the coupled equations

$$\begin{aligned} i\dot{\psi}_1 &= \gamma\psi_1 - J\psi_2 \\ i\dot{\psi}_2 &= -J\psi_1 - \gamma\psi_2 \end{aligned} \tag{4.13}$$

To be technical, we need to reintroduce $c_1(t)$ and $c_2(t)$, as described in the previous section. These are the probability amplitudes of the states $|\psi_1\rangle$ and $|\psi_2\rangle$, which are defined in the diabatic limit, meaning they are eigenstates of the time-dependent Hamiltonian (4.11).

The equations of motion are now given as

$$\begin{aligned} i\dot{c}_1 &= \gamma c_1 - J c_2 \\ i\dot{c}_2 &= -J c_1 - \gamma c_2. \end{aligned} \tag{4.14}$$

Combining both equations yields the second order equation

$$\ddot{c}_1 + c_1 \left[i\alpha + J^2 + \gamma^2 \right] = 0. \tag{4.15}$$

The probability amplitude c_1 can then be decomposed into

$$c_1(t) = \xi(t) \exp\left(-i \int_{t_0}^{t} \mathrm{d}\alpha t' \right). \tag{4.16}$$

Here the wavefunction has been divided into its time dependent component [$\xi(t)$] and its phase. By inserting Eq. (4.16) into Eq. (4.15) we arrive at the second order differential equation

$$\ddot{\xi}(t) - 2i\alpha t\dot{\xi}(t) + J^2\xi(t) = 0 \tag{4.17}$$

A "common" method for solving this ODE is by utilising parabolic cylindrical polar coordinates [137]. This method is highly complex with some non-intuitive steps. As a work around we employ a method first described in [140]. This method involves the use of the complex plane, and some relatively basic complex analysis. To begin, we make some observations about the above ODE. In the limit of $\xi(t \to \infty)$, $\dot{\xi}(t)$ and $\ddot{\xi}(t)$ must vanish as we have made the statement that the system will have undergone a complete adiabatic crossover in the long-time limit, yielding no change in the function. In order to balance the ODE, this implies $\dot{\xi}(t)$ must be finite. Hence we can neglect $\ddot{\xi}(t \to \infty)$ yielding

$$2i\alpha t\dot{\xi}(t) = J^2\xi(t). \tag{4.18}$$

The solution to this first-order ODE is found to be

$$\xi(t) = \xi(t_0)\exp\left[-iJ^2/2\alpha\ln\left(\frac{t}{t_0}\right)\right], \tag{4.19}$$

where t_0 is the initial starting time. Taking the derivative of the above yields

$$\frac{\dot{\xi}(t)}{\xi(t)} = \left(\frac{-iJ^2}{2\alpha t}\right) \tag{4.20}$$

and

$$\frac{\ddot{\xi}(t)}{\xi(t)} = \frac{J^2}{2\alpha t^2}\left(\frac{J^2}{2\alpha} - i\right). \tag{4.21}$$

We can see that the second derivative depends on t^{-2}, which justifies neglecting

the second derivative at large times. In the limit of $t \to 0$, Eq.(4.21) is simply

$$\frac{\ddot{\xi}(0)}{\xi(0)} = -J^2. \tag{4.22}$$

Returning to Eq. (4.19), we can re-write it as

$$\frac{\ddot{\xi}(t)}{\xi(t)} - 2i\alpha t\frac{\dot{\xi}(t)}{\xi(t)} + J^2 = 0. \tag{4.23}$$

We see that this is now a well defined ODE across all time as $\xi(t)$ tends to be a complex function, unless the system is pushed into a regime with unrealistic parameters, i.e., $J \to \infty$. Applying the Cauchy principal value integral with the limits $t = (-\infty, +\infty)$ yields

$$⨍_{-\infty}^{+\infty} \frac{\ddot{\xi}(t)\,\mathrm{d}t}{\xi(t)t} - 2i\alpha ⨍_{-\infty}^{+\infty} \frac{\dot{\xi}(t)\,\mathrm{d}t}{\xi(t)} + J^2 ⨍_{-\infty}^{+\infty} \frac{\mathrm{d}t}{t} = 0. \tag{4.24}$$

The final term within this limit goes to 0, while the second term is

$$⨍_{-\infty}^{+\infty} \frac{\dot{\xi}(t)\,\mathrm{d}t}{\xi(t)} = \lim_{t\to 0^+} ⨍_{\epsilon}^{+\infty} \frac{\dot{\xi}(t)\,\mathrm{d}t}{\xi(t)} = \ln[\xi(t \to 0)]. \tag{4.25}$$

This means we can express $\xi(t \to 0)$ as

$$\ln[\xi(t \to 0)] = \frac{-i}{2\alpha} ⨍_{-\infty}^{+\infty} \frac{\ddot{\xi}(t)\,\mathrm{d}t}{\xi(t)t}. \tag{4.26}$$

Equation (4.26) encloses a contour in the complex t-plane, with a residue located at $t = 0$. An illustration of the contour is shown in Fig.4.3.

The movements along the contour are:

1. $-R \to \epsilon$
2. A semicircle of radius ϵ above the real t-axis
3. $\epsilon \to R$

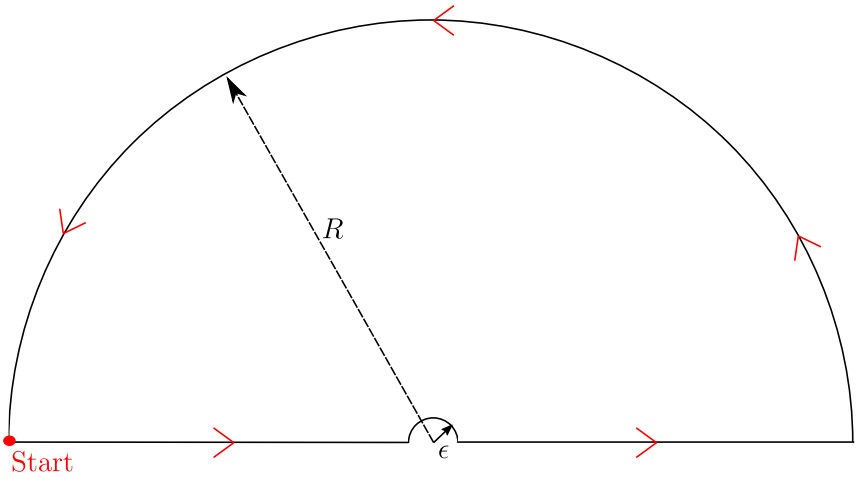

Figure 4.3: ***Complex t-plane.*** *An illustration of the complex plane with a singularity at $t = 0$.*

4. A semicircle of radius R above the real axis

Decomposing the integral via these constraints yields

$$\oint_{\mathrm{C}} \frac{\ddot{\xi}(t)\,\mathrm{d}t}{\xi(t)t} = \int_{-R}^{-\epsilon} \frac{\ddot{\xi}(t)\,\mathrm{d}t}{\xi(t)t} + \int_{\epsilon}^{R} \frac{\ddot{\xi}(t)\,\mathrm{d}t}{\xi(t)t} + \oint_{\epsilon} \frac{\ddot{\xi}(t)\,\mathrm{d}t}{\xi(t)t} + \oint_{R} \frac{\ddot{\xi}(t)\,\mathrm{d}t}{\xi(t)t}. \quad (4.27)$$

In the limit where $\epsilon \to 0^+$ and $R \to \infty$,

$$\oint_{\mathrm{C}} \frac{\ddot{\xi}(t)\,\mathrm{d}t}{\xi(t)t} = \fint_{-\infty}^{\infty} \frac{\ddot{\xi}(t)\,\mathrm{d}t}{\xi(t)t} + \oint_{\epsilon\to 0^+} \frac{\ddot{\xi}(t)\,\mathrm{d}t}{\xi(t)t} + \oint_{R\to\infty} \frac{\ddot{\xi}(t)\,\mathrm{d}t}{\xi(t)t}. \quad (4.28)$$

Within the imposed limits, the integral over t from -∞ to ∞ contains no singularities, and therefore is 0. We also note that the integral as $R \to \infty$ decays as t^{-3}, and can also be set to 0. By utilising the residue theorem, we can express the remaining integral as

$$\oint_{\epsilon\to 0^+} \frac{\ddot{\xi}(t)\,\mathrm{d}t}{\xi(t)t} = -i\pi \mathrm{Res}\left[\frac{\ddot{\xi}(t)}{\xi(t)t}, t = 0\right]. \quad (4.29)$$

Using Eq. (4.22) we find that

$$\ln[\xi(t \to 0)] = \frac{-i}{2\alpha}\left[-i\pi J^2\right] \quad (4.30)$$

$$\Rightarrow \xi(t \to 0) = \exp\left(\frac{-\pi J^2}{2\alpha}\right). \quad (4.31)$$

Or in other words,

$$P(\alpha) = |\xi(t \to 0)|^2 = \exp\left(\frac{-\pi J^2}{\alpha}\right) \tag{4.32}$$

which describes the transition probability between two states as a function of the rate α. This is the Landau-Zener transition probability, where the resulting dynamics [136, 137] has produced a vast field of research and is still lucrative in terms of its modern day applications.

4.2.2 Bose-Einstein condensates in a double well potential

Consider a similar scenario as the Landau-Zener model where now the interaction terms depend nonlinearly on the densities [92, 110–112, 141, 142]. The model consists of two levels as the previous section, except now the interaction terms depend of the occupation of the states. The total system density is normalised by $|c_1|^2 + |c_2|^2 = 1$, where c_1 and c_2 are probability amplitudes for sites 1 and 2. The hopping parameters between the sites is J, which is again taken to be negative. The level bias γ is the amount each site is offset by with respect to the zero-point energy. The evolution of the system is tracked by varying the level bias with time as $\gamma = \alpha t$, where α is a sweeping rate. When $\alpha \gg 1$ we imagine a very rapid sweep while for $\alpha \ll 1$ we imagine a slow sweep.

Beginning with the BHM, Eq. (2.21), we restrict the number of sites to $L = 2$. From here, the creation and annihilation operators can be replaced with classical fields as $\hat{a}_j \approx c_j$ and $\hat{a}_j^\dagger \approx c_j^*$, which are normalised by the total atom number $N \gg 1$. The resulting mean-field Hamiltonian is

$$\tilde{H} = \gamma c_1 - \gamma c_2 - J(c_1^* c_2 + c_2^* c_1) + \frac{W}{2}\left[|c_1|^2(|c_1|^2 - 1) + |c_2|^2(|c_2|^2 - 1)\right], \tag{4.33}$$

where $W = U_0 N$ is the mean-field interaction parameter. The nonlinear Schrödinger equation for a double-well potential is then

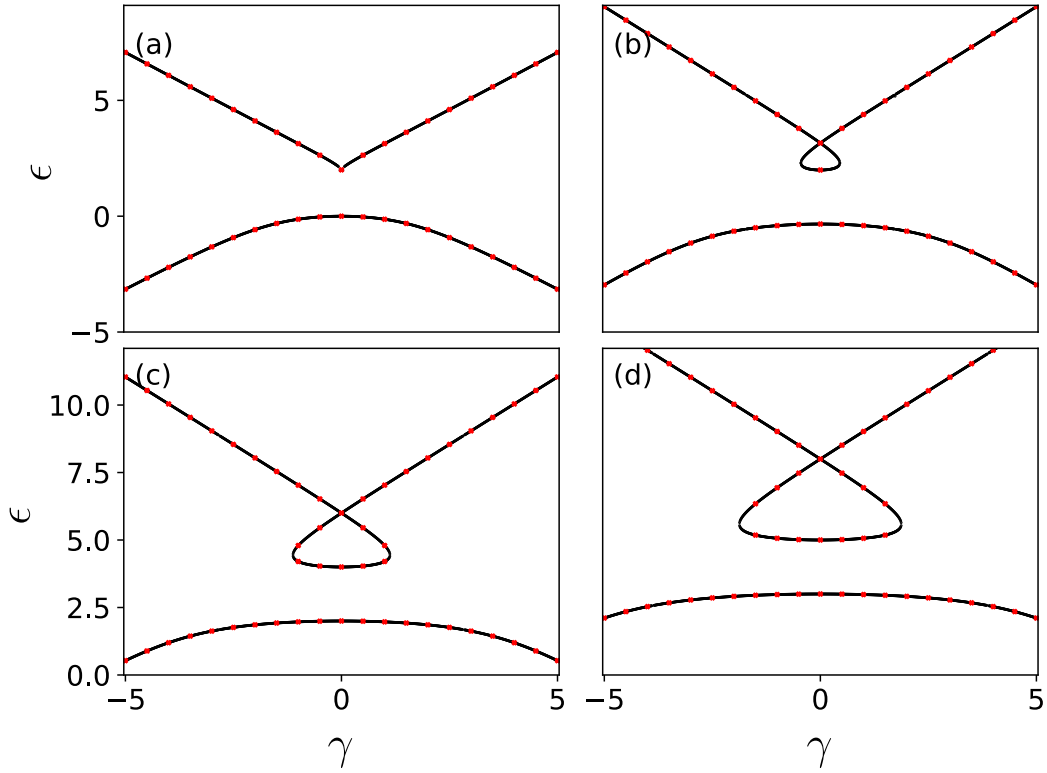

Figure 4.4: ***Double-well eigenspectrum vs level bias*** *The eigenspectrum is shown as a function of the level bias γ when the interaction strength is (a) $W = 2$, (b) $W = 4$, (c) $W = 6$, and (d) $W = 8$. The analytic results from Eq. 4.37 is shown in black while the red dots are found by numerically solving the Schrödinger equation. The numerics and analytics overlap perfectly.*

$$\mathrm{i}\frac{\mathrm{d}}{\mathrm{d}t}\begin{pmatrix} c_1 \\ c_2 \end{pmatrix} = \begin{bmatrix} \gamma + W|c_1|^2 & -J \\ -J & -\gamma + W|c_2|^2 \end{bmatrix} \begin{pmatrix} c_1 \\ c_2 \end{pmatrix}, \tag{4.34}$$

For a nonlinear system, the total number of eigenenergies is not necessarily restricted by the number of states in the system. In particular, for two sites the total number of eigenvalues can be four. When $L = 2$ there does exist an analytical solution. First we can exploit the eigenvalue equations for the Schrödinger equation by replacing $\mathrm{i}\frac{\mathrm{d}}{\mathrm{d}t}$ with the eigenvalue ϵ yielding

$$\begin{aligned} \epsilon c_1 &= \left[\gamma + W|c_1|^2\right] c_1 - J c_2 \\ \epsilon c_2 &= -\left[\gamma + W|c_2|^2\right] c_2 - J c_1. \end{aligned} \tag{4.35}$$

Multiplying both sides by their respective conjugates and subtracting yields

$$|c_2|^2 - |c_1|^2 = -\frac{\gamma}{\epsilon - W}. \tag{4.36}$$

This is then reinserted into the deterministic equation $\det[H - \epsilon\mathbb{I}] = 0$, which produces a fourth order eigenvalue equation as

$$\begin{aligned}\epsilon^4 - 3W\epsilon^3 \;&+\; \epsilon^2\left(\frac{13W^2}{4} - J^2 - \gamma^2\right) \\ &+\; \epsilon W\left(2J^2 + \gamma^2 - \frac{3^2}{2}\right) - W^2\left(J^2 - \frac{\gamma^2}{4} + \frac{W^2}{4}\right) = 0.\end{aligned} \tag{4.37}$$

The solutions to Eq. (4.37) are shown in Fig. 4.4. Additionally, we have solved Eqs. (4.34) numerically, and plot it along side the analytic results where we see great agreement. To do this, we employ a shooting method, where we self-consistently scan the solutions for a given initial condition $Y^\intercal = [\bar{c}_1, \bar{c}_2]$. Once an eigenvector is found to be a true eigenvector of the Hamiltonian, the associated eigenvalue is stored. The numerics will be important in the coming chapters as large systems sizes where $L > 2$ tend to be far too difficult to solve analytically. When $W = 2$, the eigenspectrum deformation on the upper level leads to the beginning of a bifurcation in the energy levels. This can be seen in Fig. 4.4(a). We show that this deformation develops in to a full looping structure for increasing interaction strength [see Figs. 4.4(b-d)]. The location of the deformation however is in stark contrast to simulations carried about by [111, 112]. Here they used the relative densities between sites. This created bifurcations on the lower energy levels. This means that due to the splitting in the groundstate energy level, the system was prevented from undergoing a complete adiabatic crossover when the nonlinear interaction strength was strong. This is simply a consequence of the symmetry between short-range and long-range interactions. In Refs [111, 112], the densities depend on the nonlinear interaction term as $W(|c2|^2 - |c_1|^2)$. By applying

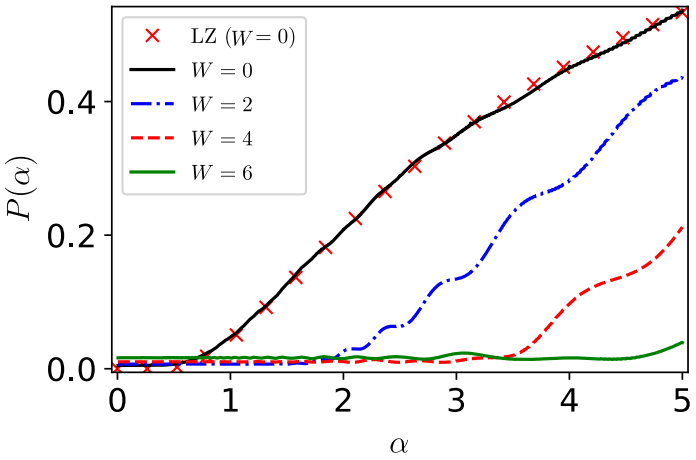

Figure 4.5: ***Retention Probability.*** *The tunnelling probability is shown for various interaction strengths. The $W = 0$ case is compared with the Landau-Zener formula from Eq. (4.32).*

the conservation condition, we see this can be expressed as $W(1 - 2|c_1|^2) = W - 2W|c_1|^2$. The constant term is simply a shift in the global energy of the system. The negative sign produces an attractive interaction over a repulsive interaction, leading to the formation of the single loop on the lowest energy level. In Fig. 4.5, the probability of the population being retained in the initial state is shown for different interaction strengths. This is calculated by using Eq. (4.32). When $\alpha \ll 1$, we see that tunnelling to the adjacent site is suppressed

We show the population dynamics between the energy levels for $W = 1$ in Fig. 4.6 for (a) $\alpha = 1$ and (b) $\alpha = 0.001$. As expected the fast quench leads to minor excitations of higher states as $\sqrt{\alpha} \sim \Delta E$. For the slow quench, we see almost full adiabatic population transfer. When we increase the interaction strength further, to $W = 5$ [Fig. 4.7 for (a) $\alpha = 1$ and (b) $\alpha = 0.001$], we see that for both the fast and slow quenches the system exhibits a complete crossover. From the eigenspectra, we see that for stronger interaction strengths, the groundstate energy level enters a plateau-like region. This fixes the energy to a near constant, meaning that any changes to the time-dependent Hamiltonian result in minute changes in the density.

Another fascinating feature attributed to the nonlinear interactions is self-trapping

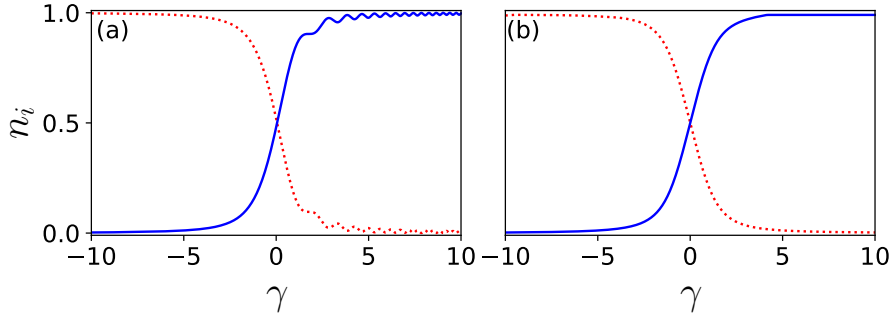

Figure 4.6: ***Landau-Zener Dynamics for weak nonlinear coupling.*** *The dynamics of the densities n_1 (dotted red) and n_2 (solid blue) is shown for tilting rates (a) $\alpha = 1$ and (b) $\alpha = 0.0001$ for $W = 1$.*

where the densities of one (or more) of the sites become fixed, even when the interaction strength is increased. We calculate this by finding the time-averaged densities in each well for a static trap ($\gamma = 0$), defined as

$$\langle n_i \rangle = \lim_{\tau \to \infty} \left[\frac{\int_0^\tau |c_i(t)|^2 \, \mathrm{d}t}{\tau} \right] \tag{4.38}$$

In practice, we take $\tau = 100$ which is more than sufficient. The loops create new avoided level crossings, leading to the nontrival tunnelling dynamics. When the energy gap between the lowest state and the first excited state is less than the tunnelling strength $\Delta E < 2J$ we see Josephson oscillations between the two states. When $\Delta E > 2J$ we enter the self-trapping regime. In Fig 4.8(a) we plot different interaction strengths which shows the difference between both regimes. For a double-well system we find that there are two dynamical regions present.

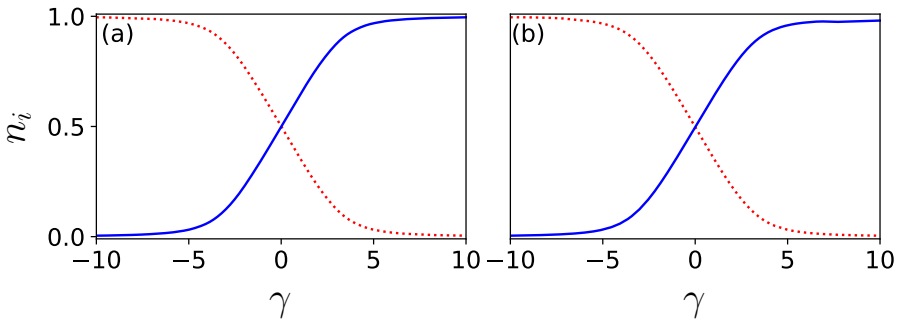

Figure 4.7: ***Landau-Zener Dynamics for strong nonlinear coupling.*** *The same dynamics as shown in Fig .4.6, now using $W = 5$.*

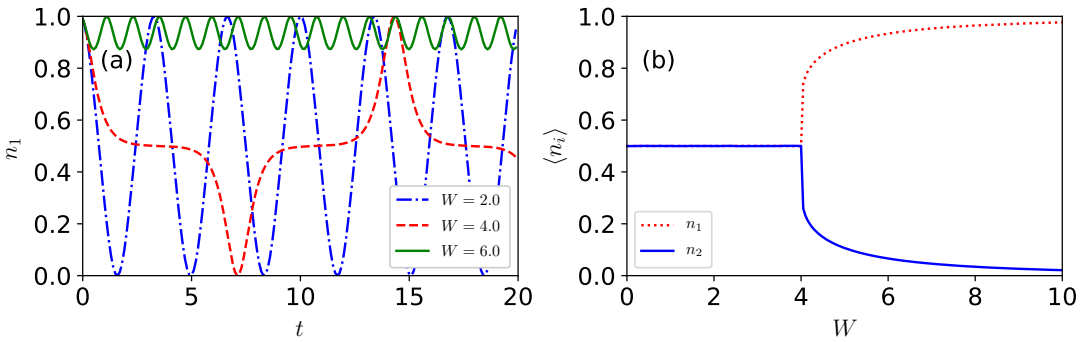

Figure 4.8: ***Dynamics and Self-trapping.*** *(a) The oscillatory dynamics for the population of site one is shown for various interaction strengths. (b) The time averaged population of both wells, with an initial condition $n_1(0) = 1$. At a critical interaction strength $W = 4$ we see the population sharply transitions to localisation in well one.*

When the nonlinear coupling is weak, i.e $W = 2$, we see Josephson oscillations between the two states. For $W = 4$, we reach a critical interaction strength where we begin to enter the regime of self-trapping. This is clearly illustrated for $W = 6$ in Fig. 4.8(a). The transition is prominent when looking at the self-trapping as a continuous function of the interaction strength, which is shown in Fig 4.8(b). After $W = 4$ the localisation follows a logarithmic scaling [111].

4.2.3 Bose-Einstein condensates in a triple well potential

We move our attention now to a system with three trapped BECs. The mean-field Hamiltonian for this scenario is

$$\tilde{H} = \sum_{j}^{3} \Gamma_j |c_j|^2 - J \sum_{\langle i,j \rangle}^{3} c_i^* c_j + \frac{W}{2} \sum_{j}^{3} |c_j|^2 (|c_j|^2 - 1). \tag{4.39}$$

The local trapping operator is $\Gamma_j = -(j-2)\gamma$.

The nonlinear Schrödinger equation for this system is

$$\mathrm{i}\frac{\mathrm{d}}{\mathrm{d}t} \begin{pmatrix} c_1 \\ c_2 \\ c_3 \end{pmatrix} = \begin{bmatrix} \gamma + W|c_1|^2 & -J & 0 \\ -J & W|c_2|^2 & -J \\ 0 & -J & -\gamma + W|c_3|^2 \end{bmatrix} \begin{pmatrix} c_1 \\ c_2 \\ c_3 \end{pmatrix}, \tag{4.40}$$

where c_1, c_2, and c_3 are the mean-field amplitudes for the respective sites; defined

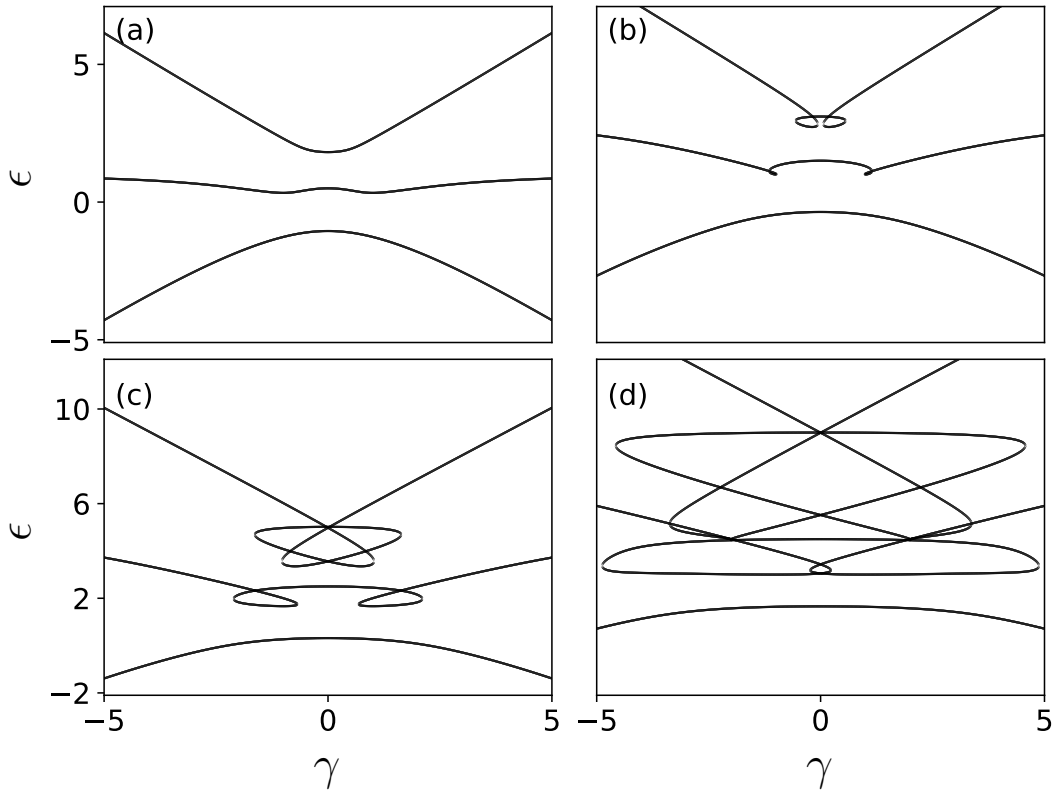

Figure 4.9: ***Triple-well eigenspectrum vs level bias.*** *The eigenspectrum is shown as a function of the level bias γ when the interaction strength is (a) $W = 1$, (b) $W = 3$, (c) $W = 5$, and (d) $W = 9$.*

in the adiabatic regime as with the double-well potential. W and γ are again the mean-field interaction strength and level bias respectively. The three sites are connected as a Bose-Hubbard chain with closed boundaries. As mentioned in the previous section, it becomes excessively difficult to analytically calculate the eigenspectrum for a system where $L > 2$. As such, we rely on numerically solving the coupled ODEs given by the Schrödinger equation, Eq. (4.40), along with the conservation equation $\sum_j |c_j|^2 = 1$.

The eigenspectra for various interaction strengths are shown in Fig. 4.9. We see striking differences between the double-well model, from Fig. 4.4. We notice the emergence of a star structure on the highest energy level, and additional loops on the middle energy levels. In total, there can be up to 9 eigenvalues for certain values of γ.

As with the double-well system, the adiabatic passage of the initial Hamiltonian

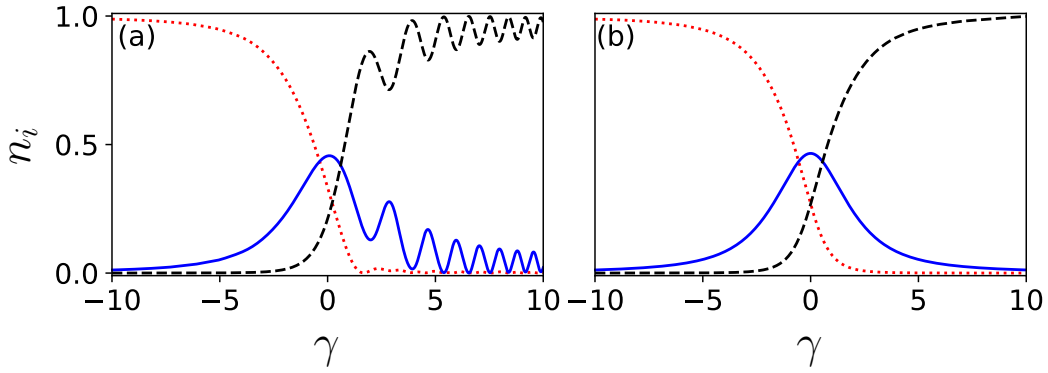

Figure 4.10: ***Landau-Zener Dynamics for weak nonlinear coupling*** *The dynamics of the densities n_1 (dotted red), n_2 (solid blue), and n_3 (dashed black) is shown for tilting rates (a) $\alpha = 1$ and (b) $\alpha = 0.001$ for $W = 1$.*

towards the final Hamiltonian remains intact even for strong nonlinear coupling, as the topology of the groundstate energy level remains the same throughout the tilting process. This can be seen in both Figs 4.10 and 4.11, where both fast ($\alpha = 1$) and slow ($\alpha = 0.001$) are shown for weak and strong nonlinear interactions respectively.

Self-trapping is also possible for triple-well BECs. Figure 4.12 shows the self-trapping dynamics for a symmetric system (i.e., $\gamma = 0$), initialised in the left site $[n_1(0) = 1]$, while Fig. 4.13 shows the same for the initial condition $n_2(0) = 1$. Here we note that the initial conditions play a major role in the dynamics seen. This will be a pivotal concept in Chapters 4 and 5, when we discuss a triple-well system with long-range interactions.

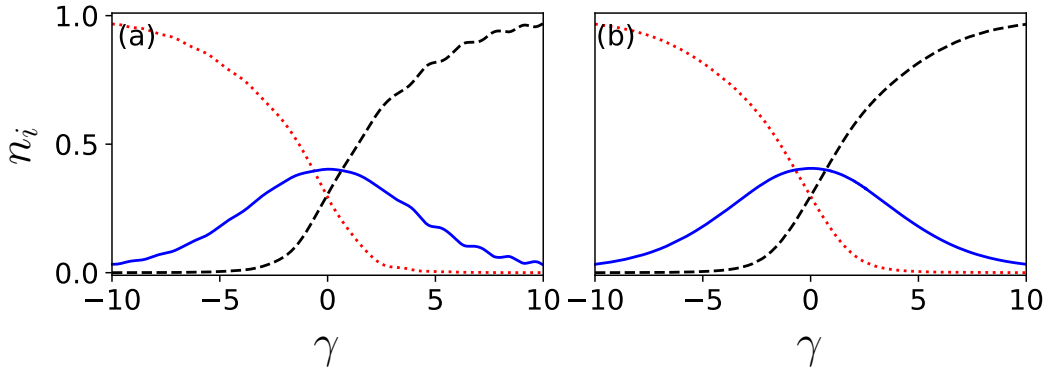

Figure 4.11: ***Landau-Zener Dynamics for strong nonlinear coupling.*** *The same dynamics as shown in Fig .4.6, now using $W = 5$.*

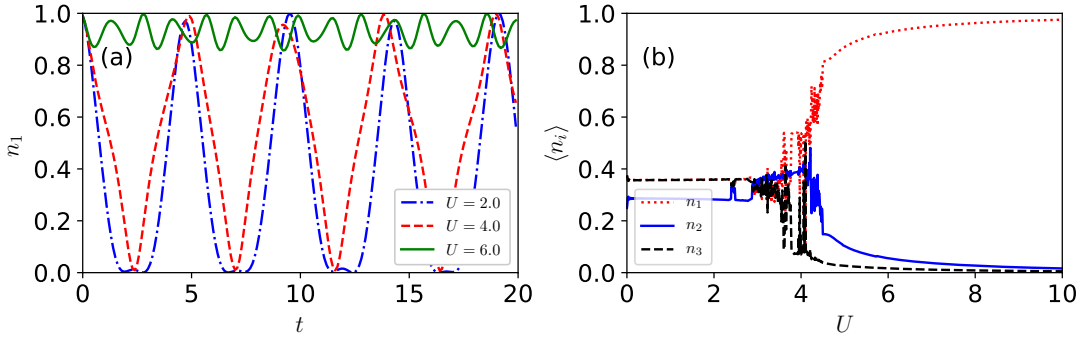

Figure 4.12: ***Oscillations and self-trapping dynamics*** $n_1(0) = 1$**.** *Here* n_1 *refers to the leftmost well. (a) Oscillatory dynamics of the left well for various interaction strengths showing the Josephson Oscillations for weak coupling and self-trapping oscillations for strong coupling. (b) Averaged-time dynamics as a function of the interaction strength*

4.3 Mean-field Hamiltonian with Rydberg-dressed interactions.

We consider N bosonic atoms in a one-dimensional trap array, whose dynamics is governed by an extended Bose-Hubbard Hamiltonian

$$\hat{H} = \sum_{j}^{3} \Gamma_j \hat{n}_j - J \sum_{\langle i,j \rangle}^{3} \hat{a}_i^\dagger \hat{a}_j + \frac{U_0}{2} \sum_{j}^{3} \hat{n}_j(\hat{n}_j - 1) + \frac{1}{2} \sum_{i,j}^{3} \Lambda_{i,j} \hat{n}_i \hat{n}_j, \quad (4.41)$$

where we have omitted the chemical potential in Eq. (2.29) and set the number of sites $L = 3$. Additonally, the generic long-range interaction term is replaced with that discrete soft-core interaction, given by Eq. (2.43). Here we imagine a

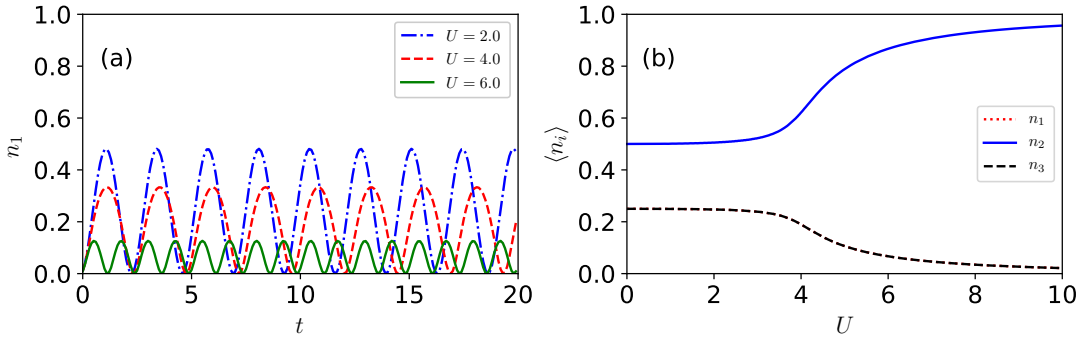

Figure 4.13: ***Oscillations and self-trapping dynamics with*** $n_2(0) = 1$*. Here* n_2 *refers to the centre well. (a) and (b) show the same dynamics as in Fig. 4.12, now with the initial condition* $n_2(0) = 1$

triple-well chain setup, i.e., closed boundary conditions. The bosonic annihilation (creation) operator at site j is given by $\hat{a}_j(\hat{a}_j^\dagger)$. Γ_j and $\hat{n}_j = \hat{a}_j^\dagger\hat{a}_j$ are the local tilting potential and number operator, respectively. The parameter $U_0 = 4\pi a_s/m$ characterizes the onsite (s-wave) interaction.

In the limit of $N \gg 1$, we employ the mean-field approximation to replace the bosonic operator with a classical field ψ_j, i.e. $\hat{a}_j \approx \psi_j$, $\hat{a}_j^\dagger \approx \psi_j^*$ and $\sum_j |\psi_j|^2 = N$ [90]. This yields the mean-field Hamiltonian

$$\begin{aligned}\tilde{H} &= \sum_j^3 \Gamma_j|\psi_j|^2 - J\sum_{\langle i,j\rangle}^3 \psi_i^*\psi_j \\ &\quad + \frac{U_0}{2}\sum_j^3 |\psi_j|^2(|\psi_j|^2 - 1) + \frac{1}{2}\sum_{i,j}^3 \Lambda_{i,j}|\psi_i|^2|\psi_j|^2. \end{aligned} \tag{4.42}$$

The dynamics of the classical field ψ_i is derived via the canonical equation $id\psi_j/dt = \partial\tilde{H}/\partial\psi_j^*$. For convenience, we define the normalized field $c_j = \psi_j/\sqrt{N}$ with the normalization condition $\sum_j |c_j|^2 = 1$. For the triple-well system, we obtain the following coupled nonlinear GP equations

$$i\dot{c}_1 = \left(W|c_1|^2 + U|c_2|^2 + V|c_3|^2\right)c_1 + \gamma c_1 - Jc_2, \tag{4.43a}$$

$$i\dot{c}_2 = \left[W|c_2|^2 + U(|c_1|^2 + |c_3|^2)\right]c_2 - J(c_1 + c_3), \tag{4.43b}$$

$$i\dot{c}_3 = \left(W|c_3|^3 + U|c_2|^2 + V|c_1|^2\right)c_3 - \gamma c_3 - Jc_2, \tag{4.43c}$$

where we have defined $W = N(\Lambda_{11} + U_0)$, $U = N\Lambda_{1,2}$ and $V = N\Lambda_{1,3}$ to be the onsite, nearest-neighbor and next-nearest-neighbor mean-field interactions, respectively. The short-range interaction W accounts for contributions from the s-wave and onsite soft-core interaction. The local potential Γ_j is antisymmetric, given by $\Gamma_j = -(j-2)\gamma$, i.e. $\Gamma_1 = \gamma$, $\Gamma_2 = 0$, and $\Gamma_3 = -\gamma$. Here γ is a bias field to create a potential height difference between neighboring traps. In Sec. 4.4.1, the potential wells are linearly biased through $\gamma = \alpha t$, with α being the sweep rate. In Sec. 4.4.2, we will consider a fixed γ. To be convenient, we will scale time and energy with respect to $1/J$ and J in the following unless stated

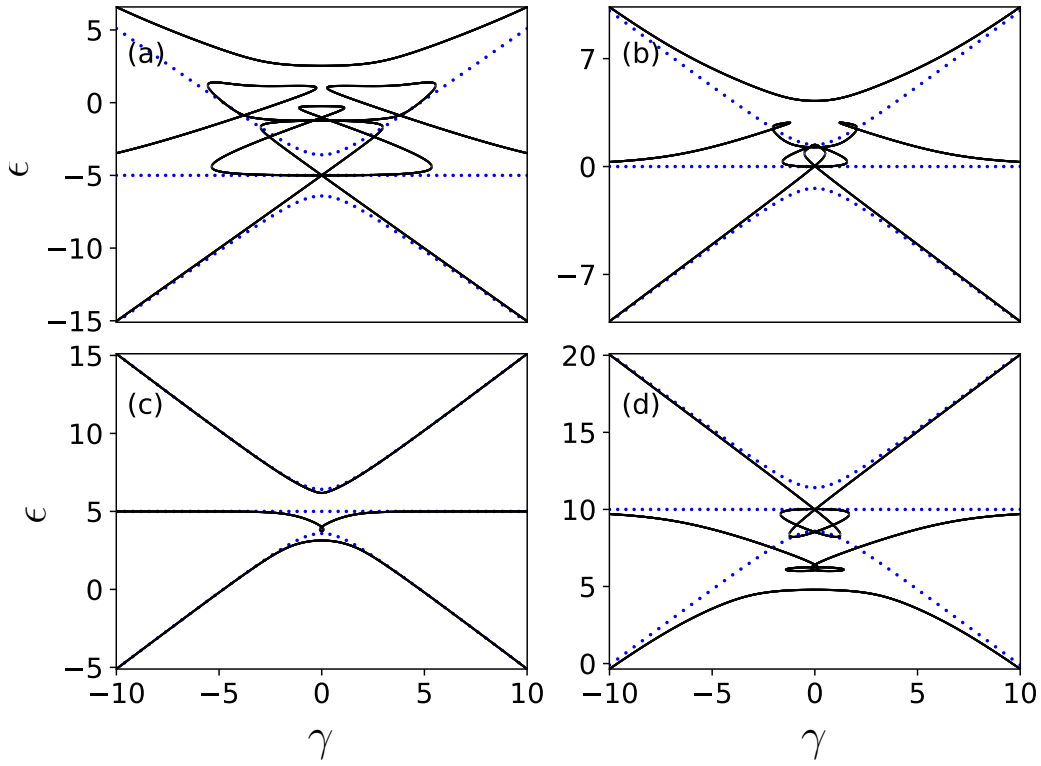

Figure 4.14: ***Energy spectra with different short-range interactions.*** *We show the adiabatic eigenspectra as a function of γ for (a) $W = -5$, (b) $W = 0$, (c) $W = 5$, and (d) $W = 10$ while fixing $U = 2V = 5$. When the short-range interaction is attractive or vanishing, loops and direct level-crossings are found in the lower branches. These structures disappear when $W = U$. When the short-range interaction dominates, the structures are found in the upper branches of the levels. The linear case ($W = U = V = 0$) is shown for reference in each panel (blue dotted). To compare with the nonlinear spectra, the linear spectra are shifted vertically by W.*

explicitly.

4.3.1 Adiabatic eigenspectra of the GP equation

When analyzing the adiabatic spectra of the system through Eqs. (4.43a-4.43c), the presence of the nonlinear interactions implies that standard methods (i.e. diagonalization of the Hamiltonian) are not valid. We adapt the method applied to treat nonlinear equations corresponding to interacting BECs in double-well potentials [111]. The basic idea is to convert the nonlinear equations into a high-order L^2 polynomial equation of eigenvalue ϵ, and additionally applying the normalization condition [143]. For $L = 3$, it becomes difficult to solve the resulting polynomial equation even numerically. As such, we employ a shooting

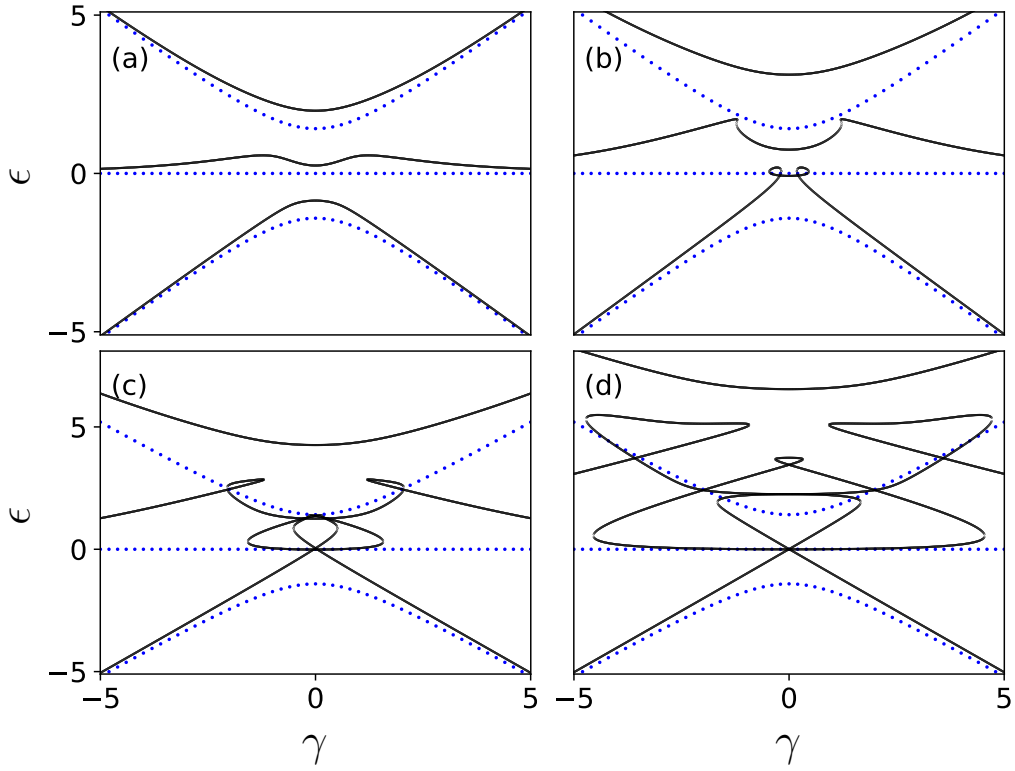

Figure 4.15: ***Energy spectra with different long-range interactions.*** *By turning off the short-range interactions ($W = 0$), the adiabatic eigenspectra are shown as a function of γ for $U = 2V$ with (a) $U = 1$, (b) $U = 3$, (c) $U = 5$, and (d) $U = 9$. When the long-range interactions are strong, loops and direct level-crossings emerge on the lower branches, as shown in panels (b)-(d). The linear case ($W = U = V = 0$) is shown for reference in each panel (blue dotted).*

method that is similar to obtaining bound states of the Schrödinger equation. A trial energy ϵ_t is fed into the nonlinear GP equations, allowing us to calculate eigenvectors $[c_1, c_2, c_3]$ and eigenenergy ϵ_n. An eigenstate is identified if the calculated and trial energy are equal, i.e., $\epsilon_t = \epsilon_n$. This is carried out for a fine grid of trial energies to obtain all eigenenergies.

We first investigate the interplay between short-range (W) and long-range (U and V) interactions. When both the short and long-range interaction are perturbative with respect to J, the eigenspectra are separated and display avoided level-crossings only, even when $\gamma \sim 0$ [see demonstration in Sec. 4.2.3]. To highlight the roles played by the nonlinear interaction, we calculate the eigenspectra of the GP equation by varying W while fixing $U = 2V = 5$, shown in Fig. 4.14. When the tilting is large, i.e., $|\gamma| > |W|$, U, and V the eigenspec-

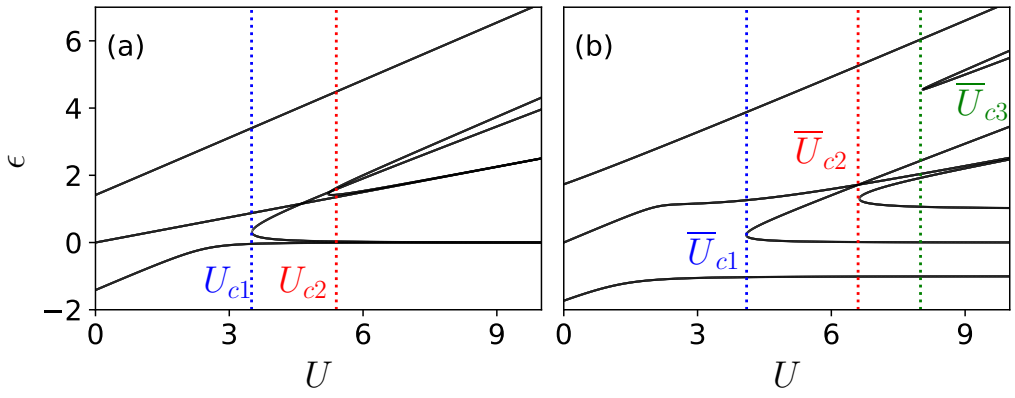

Figure 4.16: ***Energy spectra vs the long-range interactions.*** *Increasing the interaction strength leads to the creation of new energy levels in (a) symmetrical traps ($\gamma = 0$) and (b) titled traps ($\gamma = 1$). Location of the critical interaction strengths can then be extrapolated. In (a) the critical values are $U_{c1} \approx 3.5$ and $U_{c2} \approx 5.4$. In (b) the critical values are $\overline{U}_{c1} \approx 4.1$, $\overline{U}_{c2} \approx 6.6$, and $\overline{U}_{c3} \approx 8$.*

trum approaches the linear spectrum. When $W = -10$ (i.e., attractive onsite interactions), we find direct level-crossings between the lowest three branches at $\gamma = 0$. Slightly away from $\gamma = 0$, large loop structures are found, as shown in Fig. 4.14(a). When $W = 0$ similar structures are found, where the sizes of the loops shrink [Fig. 4.14(b)]. When $W = U = 2V = 5$, the loops disappear and the spectrum is similar to the linear spectrum This set of parameters largely gives a global energy shift. Due to the normalization condition, only Eq. (4.43a) and Eq. (4.43c) have a single nonlinear term proportional to V while Eq. (4.43b) has no nonlinear interaction term anymore. When $W = 10$ [Fig. 4.14(d)], the loop and level crossings re-appear in the higher energy branches. In this case the spectra are dominated by the short-range interaction. This structure is similar to previous studies in systems with bare onsite interactions [116, 117, 117] where the loops and level-crossings form star-like structures.

In the remainder of this work, we will focus on a regime where only *long-range interactions* are present (i.e., $W = 0$). For soft-core interactions where $R \gg 1$, the nearest and next-nearest neighbor interactions are the same as $U = V$. The resulting spectra can be obtained from BECs with bare short-range interactions [see details in Sec. 4.2.3]. This can be understood since the particle conservation maps the long-range interaction to an attractive short-range interaction.

To violate this symmetry, we will focus on a condition $U = 2V$, which will be used for the remainder of this chapter. This restriction can move the loop and level-crossings to the central region, leading to interesting dynamics. For weak long-range interactions, the eigenenergies are slightly modified from the linear counterpart [Fig. 4.15(a)]. When the long-range nonlinear interaction is strong (i.e., U, $V \gg 1$), the energy levels are pushed upwards by increasing U and V, as can be seen in Fig. 4.15(b). The spectrum develops a loop structure on the lowest level when $U = 2V = 3$. By further increasing the long-range interactions [see Figs. 4.15(c) and (d)], the loops become larger and more complicated level-crossings emerge in higher energy states.

In Fig. 4.16(a) we plot the energy levels as a function of U with $\gamma = 0$. At a critical interaction strength $U_{c1} \approx 3.5$, a new branch of levels emerges. Further increasing U to $U_{c2} \approx 5.4$, a second branch appears at higher energies. Note that explicit values of U_{c1} and U_{c2} depend on γ. Fig. 4.16(b) shows another example for a tilted trap with $\gamma = 1$. The levels are more separated in the low energy region. Here the two critical values are $\overline{U}_{c1} \approx 4.1$ and $\overline{U}_{c2} \approx 6.6$. Furthermore we see the emergence of a third energy level at $\overline{U}_{c3} \approx 8$. In the following sections, we will show that the critical values of the long-range interaction strongly relate to dynamical behaviors of the system.

4.4 Results

4.4.1 Landau-Zener and nonadiabatic transitions

In this section we study the dynamics of the long-range interacting BEC when the traps are tilted at different rates α. Without nonlinear interactions ($U = V = 0$), the level spacing is determined by the tunneling rate J. In the diabatic regime where $\sqrt{\alpha}$ is large and comparable to the typical level spacing ΔE [see dashed curve in Fig. 4.15], the system does not have enough time to respond to the change of the tilting. Starting from the ground state, higher energy levels will

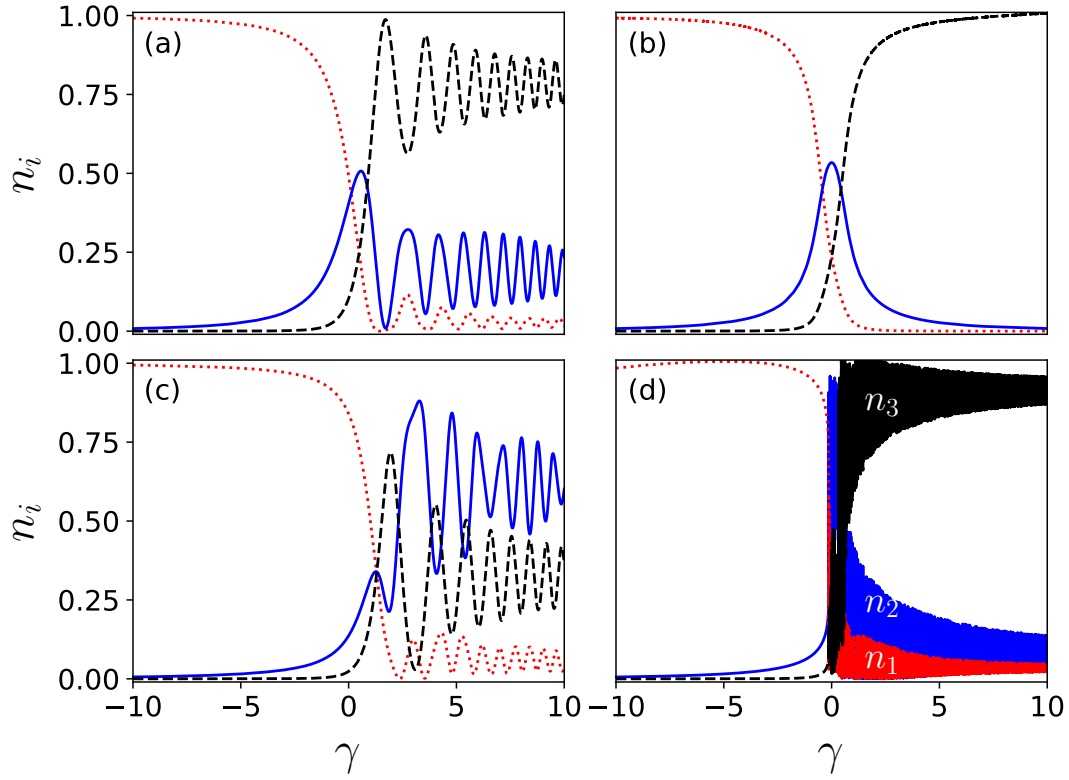

Figure 4.17: ***Landau-Zener transitions with weak and strong interactions.*** *The bias potential is tilted with a fast rate $\alpha = 1$ in (a) and (c), and a much slower rate $\alpha = 0.001$ in (b) and (d). The interaction is $U = 2V = 1$ in the upper panels and $U = 2V = 3$ in the lower panels. For rapid tilting, higher energy modes are excited such that oscillatory dynamics are observed in (a) and (c). For slow tilting, the dynamics depends strongly on the nonlinear interactions. When the interaction is strong, the adiabatic condition is broken [see Fig. 4.16(b)]. The densities n_1, n_2, and n_3 are given by the dotted red, solid blue, and dashed black lines.*

be excited. In the adiabatic regime where $\sqrt{\alpha}$ is small, the adiabatic theorem states that the system will remain in an instantaneous eigenstate under variation of α [144, 145]. This has been studied extensively with two-state (well) systems, where the transition probability from $t \to -\infty$ to $t \to \infty$ is given analytically by Eq. (4.32)

In Fig. 4.17, the population evolution of the BECs in the three wells is shown in the presence of weak interactions. Initially all atoms are in the left well $[n_1(0) = 1]$. When the trap is tilted rapidly at rate $\alpha = 1$ [Fig. 4.17(a)], the population undergoes fast oscillations when the tilting is reversed, i.e., $\gamma > 0$. This case corresponds to the diabatic regime where the lowest energy gap is $\Delta E = 0.6$, comparable to $\sqrt{\alpha} = 1$. The level spacing ΔE now depends on the nonlinear

interaction strengths, in addition to the hopping. In Fig. 4.17(b), we show the population evolution for slow tilting with $\alpha = 0.001$. The dynamics is in the adiabatic limit, as $\sqrt{\alpha} \approx 0.03 \ll \Delta E$, leading to smooth population changes among the three wells. The system follows the ground state adiabatically, where the population tunnels from the leftmost to rightmost well.

For sufficiently strong nonlinear interactions, the lower levels develops loop structures near $U > U_{c1}$. Due to the nonlinearity, the number of eigenvalues available is now greater than the dimension of the Hilbert Space. Dynamically, the system undergoes multiple avoided and direct level-crossings, when increasing γ from $-\infty \to +\infty$. As a result, oscillations are seen in the diabatic regime due to the excitation of higher energy eigenstates [see Fig. 4.17(c)]. In the adiabatic limit, the loop structures play vital roles as many eigenstates are excited, giving rise to extremely fast oscillations with multiple frequencies, as seen in Fig. 4.17(d).

To show the influence of the long-range interaction on the dynamics, we show the probability of the population being retained in the initial state (left well) for different tilting rate α in Fig. 4.18. The excitation probability is largely captured by the Landau-Zener transition probability Eq.(4.32) when the nonlinear interaction vanishes. When $U = 1$ the retention probability of the initial well increases. It approaches the non-interacting case in the adiabatic limit when $\alpha \ll 1$. Note that there are no simple power laws present in the tunneling probability as a function of α, which is different from the double-well potentials [111]. For even stronger interactions $U = 3$, the excitation probability depends on α non-monotonically. The retention probability is large when $\alpha < 1$, and becomes dramatically larger when $\alpha > 1$. As shown in Fig. 4.15, the presence of the loop and level-crossings breaks the adiabatic condition. Violating the Landau-Zener prediction in the adiabatic limit has also been shown for both double-well [111–114] and triple-well system with short-range interactions [115, 123].

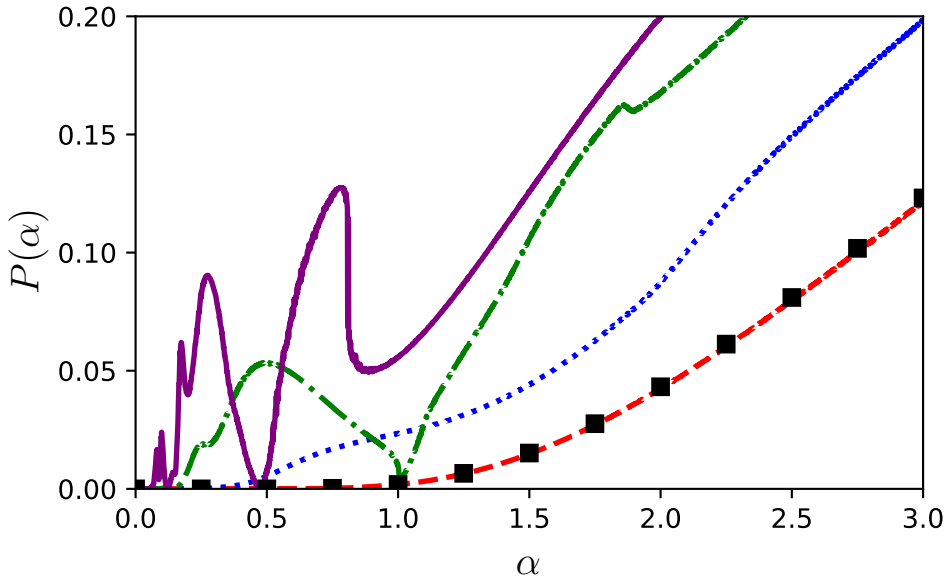

Figure 4.18: ***Retention probability of the initial state.*** *The analytical Landau-Zener probability for $U = 0$ is given by the black squares. The other curves correspond to the numerical calculations for $U = 0$ (red dashed), $U = 1$ (blue dotted), $U = 2$ (green dot-dashed), and $U = 3$ (purple solid). The parameter γ is varied from $-10 \to +10$ in calculating the probability.*

4.4.2 Self-trapping and chaotic dynamics

The retention probability in Fig. 4.18 indicates the emergence of self-trapping when the long-range interaction is strong. Self-trapping has been extensively studied in double-well potentials [110, 111]. BECs with short-range interactions can localize in a single well as the densities scale logarithmically with the interaction strength, above a certain critical value. Self-trapping is also studied with short-range interacting BECs in triple-well potentials [115, 116]. Here, we will discuss the differences between both short and long-range interactions, and how we can control the final distribution of atoms by manipulating the initial conditions.

Without nonlinear interactions ($U = 0$), the mean-field Eqs. (4.43a-4.43c) are analytically solvable, yielding solutions

$$\begin{aligned} c_1(t) &= \frac{1}{\omega^2}\Big\{ J\left[J\bar{c}_1 + \gamma\bar{c}_2 - J\bar{c}_3\right] \\ &+ \left[\gamma^2\bar{c}_1 - J\gamma\bar{c}_2 + J^2\left[\bar{c}_1 + \bar{c}_3\right]\right]\cos\omega t \\ &+ \mathrm{i}\omega\left[J\bar{c}_2 - \gamma\bar{c}_1\right]\sin\omega t\Big\}, \end{aligned} \tag{4.44a}$$

$$
\begin{aligned}
c_2(t) &= \frac{1}{\omega^2}\Big\{\gamma\left[J\bar{c}_1+\gamma\bar{c}_2-J\bar{c}_3\right] \\
&+ \left[2J\bar{c}_2+\gamma[\bar{c}_3-\bar{c}_1]\right]\cos\omega t \\
&+ \mathrm{i}\omega[\bar{c}_1-\bar{c}_3]\sin\omega t\Big\}, \qquad (4.44b)\\
c_3(t) &= \frac{1}{\omega^2}\Big\{-J\left[J\bar{c}_1+\gamma\bar{c}_2-J\bar{c}_3\right] \\
&+ \left[J\gamma\bar{c}_2-\gamma^2\bar{c}_3+J^2\left[\bar{c}_1+\bar{c}_3\right]\cos\omega t\right] \\
&+ +\mathrm{i}\omega\left[J\bar{c}_2+\gamma\bar{c}_3\right]\sin\omega t\Big\}, \qquad (4.44c)
\end{aligned}
$$

where $\omega=\sqrt{2J^2+\gamma^2}$ and $Y^\intercal=[\bar{c}_1,\bar{c}_2,\bar{c}_3]$ denotes the eigenvectors at $t=0$.

In the presence of nonlinear interactions, the mean-field equations are solved numerically with a given set of parameters and initial conditions. To characterize dynamics in the long time limit, we calculate the time averaged densities in individual wells by Eq. (4.38). In the numerical simulations, we integrate the nonlinear GP equations from $t=0$ up to $t=100$. We have checked that consistent results can be obtained when integrating the GP equations up to this time.

In the following we consider several different cases for both the symmetric and antisymmetric trap setups, to demonstrate the importance that the initial conditions have on the dynamics. We begin by looking at the symmetric case where $\gamma=0$.

Case I: $Y^\intercal=[1/2,1/\sqrt{2},1/2]$

The lowest energy eigenstate when $U=0$ is given by $Y^\intercal=[1/2,1/\sqrt{2},1/2]$. Using this as the initial state, the corresponding atomic densities in each wells are obtained by using Eq. (4.38),

$$\langle n_1\rangle=\langle n_3\rangle=\frac{1}{4},\ \langle n_2\rangle=\frac{1}{2}.$$

The majority of the particles are found in the middle well. Using the same initial state, we numerically solve the GP equations for different U. In Fig. 4.19(a), the average density decreases in the two outer wells while increasing in the middle site,

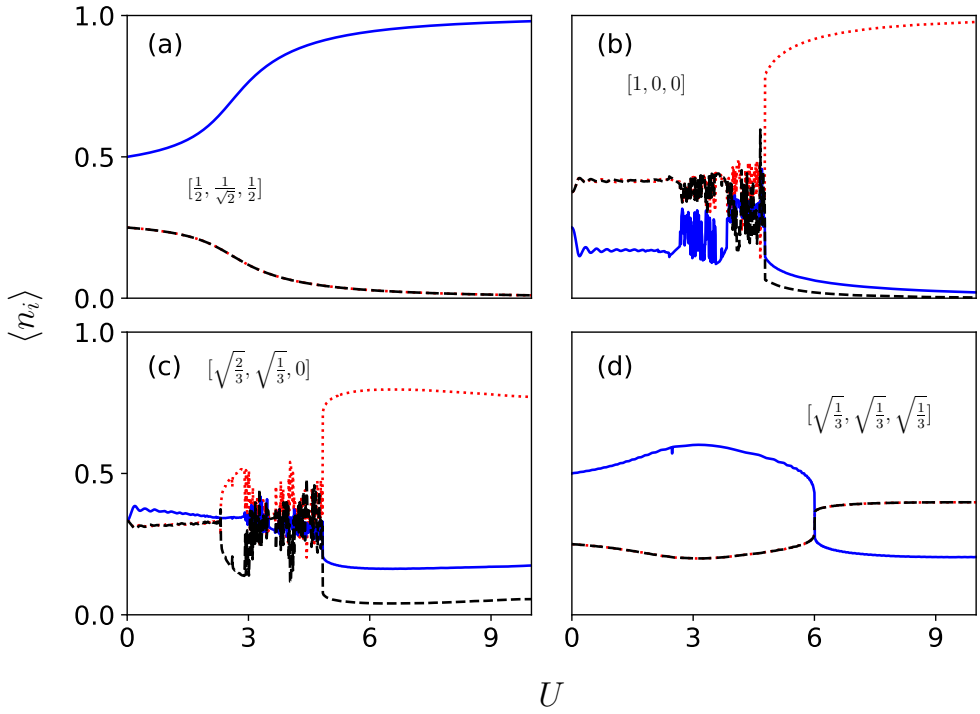

Figure 4.19: ***Self-trapping of the populations with different initial conditions with symmetric wells.*** *The time-averaged densities of each site are shown as a function of the interaction strength U for $\gamma = 0$. The initial conditions $Y^\intercal = [\bar{c}_1, \bar{c}_2, \bar{c}_3]$ are shown as insets in each panel. The densities of the left, middle and right wells are denoted with red dotted, blue solid, and black dashed curves. The average density is obtained by evolving the GP equations to time $\tau = 100$.*

as U increases. When $U \gg 1$, the population tends to fully localize in the middle site. Due to strong nearest-neighbor and next-nearest-neighbor interactions, the lowest energy corresponds to all atoms sitting in one well, as we show in the numerical simulation. Here we see a smooth transition from the initial densities towards the self-trapping regime. From Fig 4.16 (a) we see that when $U > U_{c1}$ the lowest energy level is largely independent of U. The next excited level has also merged with the lowest level, preventing any occupation of higher energy modes. This accounts for the smooth increase in the densities as each the energy gap separating any higher levels is larger than the hopping strength, i.e $\Delta E > J$.

Case II: $Y^\intercal = [1, 0, 0]$

When changing the initial state to $Y^\intercal = [1, 0, 0]$, the dynamics of the population changes drastically. Without interactions, the time-average populations are

obtained again with the help of Eq. (4.38),

$$\langle n_1 \rangle = \langle n_3 \rangle = \frac{3}{8},\ \langle n_2 \rangle = \frac{1}{4}.$$

Increasing U, the average densities of the middle well decreases slightly and then stays at a lower value [Fig. 4.19(b)]. The populations then become turbulent as the interaction strength passes $U = U_{c1}$, where the dynamics can not be categorized by standard Josephson or self-trapping regimes. Due to the complicated energy levels [see Fig. 4.16(a)], chaotic dynamics is produced as particles tunnel between each site within the range of $U_{c1} < U < U_{c2}$. This chaotic dynamics continues until the interaction strength passes $U = U_{c2}$. The self-trapping re-emerges such that the BECs localize in the left well when $U > U_{c2}$.

Case III: $Y^\intercal = [\sqrt{2/3}, \sqrt{1/3}, 0]$

Fig 4.19(c) shows the system being initialized in the state $Y^\intercal = [\sqrt{2/3}, \sqrt{1/3}, 0]$. Without interactions (i.e. $U = 0$), the average densities in each well are

$$\langle n_1 \rangle = \langle n_2 \rangle = \langle n_3 \rangle = \frac{1}{3}.$$

As with the previous case, the dynamics is turbulent within the region of $U_{c1} < U < U_{c2}$ due to the superposition of energy levels. What is interesting is that the densities are no longer localized in a single well in the limit when $U \to \infty$. Here the weighting of the initial conditions have allowed for approximately 17 % of the atoms to occupy the middle well, with the remainder almost all in the left well.

Case IV: $Y^\intercal = [\sqrt{1/3}, \sqrt{1/3}, \sqrt{1/3}]$

Next we examine the initial condition $Y^\intercal = [\sqrt{1/3}, \sqrt{1/3}, \sqrt{1/3}]$. The time-average density with $U = 0$ is

$$\langle n_1 \rangle = \langle n_3 \rangle = \frac{1}{4},\ \langle n_2 \rangle = \frac{1}{2}.$$

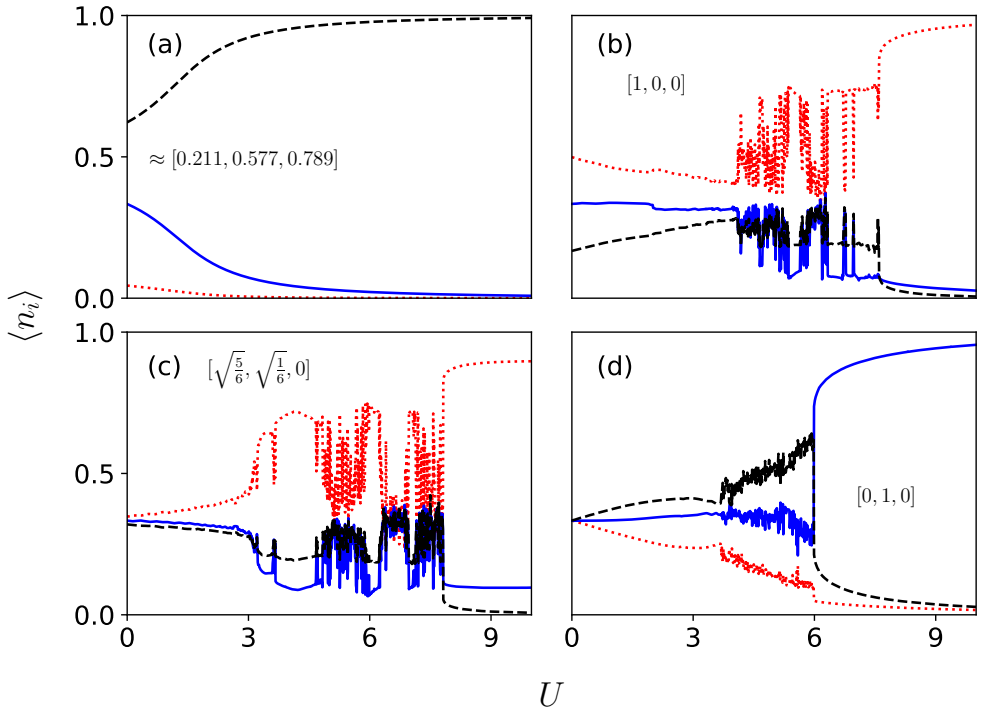

Figure 4.20: ***Self-trapping of the populations with different initial conditions with antisymmetric wells.***. *The same as Fig. 4.19, except now* $\gamma = 1$

For this case we see drastically different dynamics in Fig. 4.19(d). First, we note that in the intermediate region $U_{c1} < U < U_{c2}$, the system bypasses any chaotic dynamics. This will be examined in more detail in the coming section, however we can attribute this to the structure of phase space that the fixed points travel through. Moreover, this case provides an example of self-trapping in three wells simultaneously, as $n_i > 0 \; \forall \; i$, when $U \gg 1$.

Case V: $Y^\intercal \approx [0.221, 0.577, 0.789]$

We now move on to examine the antisymmetric case by focusing on $\gamma = 1$. In Fig. 4.20(a), we begin by examining the lowest energy eigenvector $Y^\intercal \approx [0.221, 0.577, 0.789]$. When $U = 0$ the time-average densities of each well are

$$\langle n_1 \rangle \approx 0.045, \; \langle n_2 \rangle = \frac{1}{3}, \; \langle n_3 \rangle \approx 0.622.$$

As with the symmetric case, the system is prepared in an eigenstate of the initial Hamiltonian, meaning that there is a smooth transition as the state follows the

constant energy past $U \gtrsim 3$. From Fig. 4.16(b) we see that the energy difference between the lowest energy state and the upper states is far larger than the hopping strength, i.e $\Delta E > J$, preventing coupling to higher energy states.

Case VI: $Y^\intercal = [1, 0, 0]$

We begin to see more interesting dynamics when the initial condition $Y^\intercal = [1, 0, 0]$ is again chosen. For the tilted wells this gives the noninteracting densities

$$\langle n_1 \rangle = \frac{1}{2},\ \langle n_2 \rangle = \frac{1}{3},\ \langle n_3 \rangle = \frac{1}{6}.$$

At first glance these initial values may seem uninteresting, however they imply that even though the trap is orientated such that the rightmost well has the lowest overall level bias, the densities are still localized mainly in the leftmost well. This phenomenon is extremely counter-intuitive as one would expect a large proportion of the densities to tunnel to the lowest available state. When we numerically solve the nonlinear GP equation [see Fig. 4.20(b)], we see this feature persist for strong nonlinear interaction strength $U > \overline{U}_{c3}$. The intermediate chaotic region now spans the entire range of $\overline{U}_{c1} < U < \overline{U}_{c3}$, as the tilted orientation produce a further energy level at much larger interaction strengths [see Fig. 4.16(b)]. As $U \to \infty$, we see that the localization is almost fully in the leftmost well, with the highest level bias energy. Similar phenomena where reported for the short-range interacting system in Ref. [116].

Case VII: $Y^\intercal = [\sqrt{5/6}, \sqrt{1/6}, 0]$

The noninteracting density for this case can be obtained by using Eq. (4.38),

$$\langle n_1 \rangle = \frac{17 - 2\sqrt{5}}{36},\ \langle n_2 \rangle = \frac{1}{3},\ \langle n_3 \rangle = \frac{17 + 2\sqrt{5}}{36}.$$

Similar to the previous case in Fig. 4.20(c), we see that this initial condition yields highly chaotic dynamics, where the range of the chaos extends the region

$\overline{U}_{c1} < U < \overline{U}_{c3}$. When the nonlinear interaction is strong, and the system enters the self-trapped regime ($U > \overline{U}_{c3}$) we see that self trapping occurs in the leftmost and middle wells, with roughly 10% of the particles occupying the middle site.

Case VIII: $Y^\intercal = [0, 1, 0]$

In this case, the time-average density when $U = 0$ is

$$\langle n_1 \rangle = \langle n_2 \rangle = \langle n_3 \rangle = \frac{1}{3}.$$

In Fig. 4.20(d) we see self-trapping dynamics once the interaction passes $U > \overline{U}_{c2}$, as only the lowest energy level is occupied. When $\overline{U}_{c1} < U < \overline{U}_{c2}$ the dynamics is unstable such that the average density fluctuates drastically when varying U.

4.4.3 Poincaré sections and chaotic dynamics

Figs. 4.19 and 4.20 show that regular and chaotic dynamics can be triggered by varying the initial state, even when the long-range interactions are the same. This dependence comes from the fact that energies of the system are changed when considering different initial states. As the energy is a conserved quantity, the system will show vastly different trajectories in phase space. We now illustrate this dependence using Poincaré sections [116, 146].

To obtain the Poincaré section, Hamiltonian (4.42) is converted to a classical Josephson-like analogue, where the resulting equations of motion define a 4-dimensional phase space in terms of the canonical variables $\{n_1, \theta_1\}$ and $\{n_3, \theta_3\}$ The amplitudes of each site can be expressed in terms of the total density and a phase factor as $c_i = \sqrt{n_i}\mathrm{e}^{i\phi_i}$. Importantly, only the relative phase between each site is an observable, meaning we can define the relative phase factors $\theta_1 = \phi_2 - \phi_1$ and $\theta_3 = \phi_2 - \phi_3$. The conservation condition means that the densities of the second site is defined by $n_2 = 1 - n_1 - n_3$. Using these, the mean-field Hamiltonian (4.42) can be expressed similarly to a classical Josephson Hamiltonian of the form

$$\begin{aligned}\mathcal{H} = &- 2J\sqrt{1-n_1-n_3}\left[\cos(\theta 1)\sqrt{n1}+\cos(\theta 3)\sqrt{n3}\right] \\ &+ U(1-n_1-n_3)(n_1+n_3)+Vn_1n_3+\gamma(n_1-n_3) \end{aligned} \tag{4.45}$$

The resulting Lagrangian equations of motion for conserved momenta then read

$$\dot{n}_1 = -2J\sqrt{n_1}\sqrt{1-n_1-n_3}\sin(\theta_1) \tag{4.46}$$

$$\dot{n}_3 = -2J\sqrt{n_3}\sqrt{1-n_1-n_3}\sin(\theta_3) \tag{4.47}$$

$$\begin{aligned}\dot{\theta}_1 = &\; U\left(1-2n_1-2n_3\right)+Vn_3+\gamma-\frac{J\sqrt{1-n_1-n_3}\cos(\theta_1)}{\sqrt{n_1}} \\ &+ \frac{J\left[\sqrt{n_1}\cos(\theta_1)+\sqrt{n_3}\cos(\theta_3)\right]}{\sqrt{1-n_1-n_3}}\end{aligned} \tag{4.48}$$

$$\begin{aligned}\dot{\theta}_3 = &\; U\left(1-2n_1-2n_3\right)+Vn_1-\gamma-\frac{J\sqrt{1-n_1-n_3}\cos(\theta_3)}{\sqrt{n_3}} \\ &+ \frac{J\left[\sqrt{n_1}\cos(\theta_1)+\sqrt{n_3}\cos(\theta_3)\right]}{\sqrt{1-n_1-n_3}}\end{aligned} \tag{4.49}$$

These equations provide an alternate way of calculating the dynamics, which can also be used to explore how the relative phase of each site changes as a function of time. For a given set of initial condition $\{n_1(0), \theta_1(0)\}$, conservation of energy allows us to find the initial $n_3(0)$ for a given energy value E where $E = \mathcal{H}$, while looking along the plane of $\theta_3 = 0$. The intersection of n_1 and θ_1 along the plane of $\theta_3 = 0$ in the $\dot{\theta}_3 < 0$ are recorded to produce the Poincaré section.

In Fig. 4.21(a) we show the Poincaré section when the average energy $E = \langle\mathcal{H}\rangle/N = -0.5$. Regular orbits mean that solutions to the dynamics will travel across phase space via smooth paths periodically. This energy is associated with the initial conditions given by Figs. 4.19(a) and (d), which do not show chaos in their time-averaged dynamics in the interplay region of $U_{c1} < U < U_{c2}$. In Fig. 4.21(c) we show dynamics of the population that corresponds to the initial

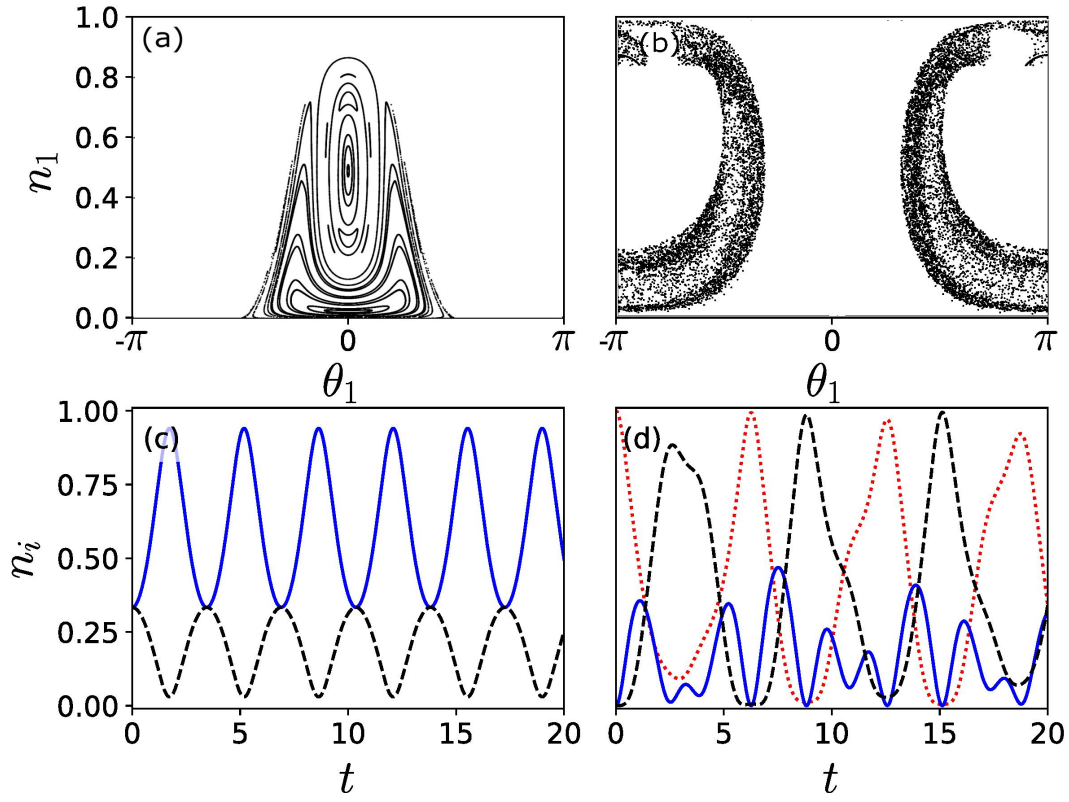

Figure 4.21: ***Poincaré Sections, regular and chaotic population dynamics.*** *The Poincaré sections for (a) $E = -0.5$ and (b) $E = 0.2$ are shown. Panels (c) and (d) show dynamics of n_1 (red dotted), n_2 (solid blue), and n_3 (black dashed) using initial conditions that would lie on the sections of (a) and (b) respectively. Other parameters are $U = 3$ and $\gamma = 0$.*

condition of Fig. 4.19(d). The periodic oscillation of the population is consistent with the regular pattern in the Poincaré section. Fig. 4.21(b) shows a very different situation where the Poincaré section at $E = 0.2$ only has localized regions of chaos, corresponding to the initial conditions of Figs. 4.19 (b) and (c). In Fig. 4.21(d), we see that the associated dynamics does not show regular periodic oscillations. Recent studies have found interesting chaotic dynamics emerging from three-state systems when nonlinear interactions become strong [118–120]. The understanding of the chaotic dynamics and its control in Rydberg-dressed BECs will be useful for future experiments.

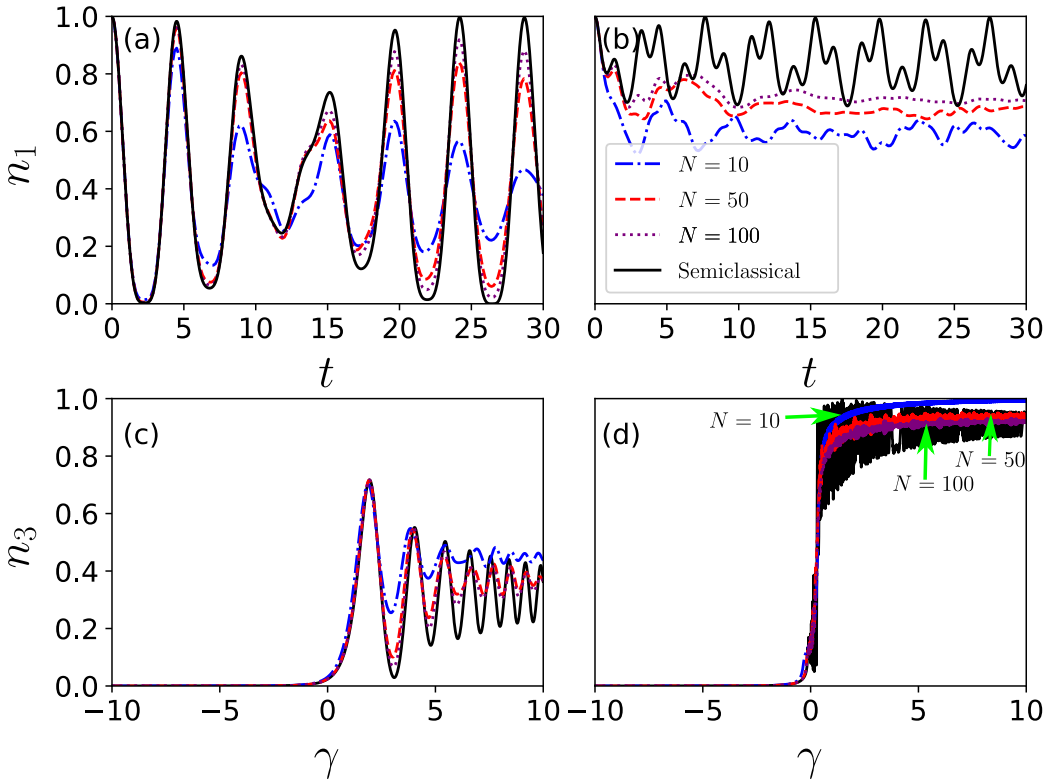

Figure 4.22: ***Quantum and semiclassical dynamics.*** *Populations obtained from the extended Bose-Hubbard Hamiltonian (4.41) using (a) $U = 1$ and (b) $U = 5$ for different atom numbers. The black solid curves show the mean-field results with same interactions. Landau-Zener transitions are shown when (c) $\alpha = 1$ and (d) $\alpha = 0.01$ with $U = 3$. Arrows are used in (d) to distinguish the different oscillations.*

4.4.4 Comparison between quantum and mean-field dynamics

The mean-field dynamics presented in previous sections is obtained in the limit $N \to \infty$. Experimentally, self-trapping of populations has been observed with BECs containing about 1000 atoms in double-well potentials, where dynamics of the BEC can be accurately described by the mean-field theory [113]. In this section, we will show that the adiabatic and nonadiabatic dynamics predicted by the mean-field theory can be also seen in relatively small systems with $N \leq 100$. To study the quantum dynamics, we numerically solve the Schrödinger equations using the three-site Bose-Hubbard Hamiltonian (4.41). We will encounter a time-dependent Hamiltonian when studying the Landau-Zener transition.

In the Josephson oscillation regime when $U < U_{c1}$, populations oscillate among

the potential wells almost completely, as shown in Fig. 4.22(a). At later times, the population partially returns to the initial well. The long-time dynamics of the population shows a relaxation, especially when N is small. Increasing N, we find that the relaxation becomes weaker, such that the quantum dynamics resembles that of the mean-field calculation. Similar dynamics has been investigated in detail in Ref [147]. When approaching the self-trapping regime ($U > U_{c1}$), only a small fraction of populations can tunnel to other potential wells. The population oscillates irregularly around a constant that is close to 1 [see Fig. 4.22(b)]. Increasing N, we find that amplitudes of the oscillation decrease rapidly, and the average population also increases. The average population, however, is smaller than the mean-field result. The difference is largely attributed to the many-body correlations between potential wells, which are neglected in the mean-field calculations

In Fig. 4.22(c) and (d) we study Landau-Zener dynamics by dynamically changing the trap bias from $\gamma = -10$ to $\gamma = 10$ in Hamiltonian (4.41). The corresponding mean-field dynamics is shown in Fig 4.17(c) and (d). When rate α is large, the right well starts to be populated once $\gamma > 0$. Further increasing γ, the population oscillates with larger amplitudes for larger N. Remarkably, such evolution agrees with the mean-field calculation well. In the adiabatic regime with $\alpha = 0.01$, the mean-field calculation shows rapid oscillations around $n_3 \sim 1$. We note that the quantum dynamics is less oscillatory than the mean-field result, especially when N is large. However, asymptotic values from both quantum and mean-field calculations agree when $\gamma \gg 1$.

4.5 Discussion

We have studied the dynamics of Rydberg-dressed BECs in a triple well potential. Within the mean-field theory, we have obtained eigenenergies of the system for different combinations of parameters. It is found that the eigenspectrum develops multiple level-crossings in the lower branches of the eigenspectra, when

the soft-core interaction is strong. The presence of level-crossings in the lower branches leads to more complicated dynamics than BECs with only short-range interactions. We have shown that it is possible to achieve self-trapping of populations in either one, two, or three wells by varying the initial conditions and the level bias. We have identified parameter regions, where dynamics is chaotic. This is demonstrated with the population evolution, and further confirmed with Poincaré sections. By numerically solving the quantum Hamiltonian for fixed particle numbers, we have shown that similar behaviour to the mean-field results can be observed even when the particle number is only $N \sim 100$. In the next chapter, study how chaos emerges in the finite trap system due to strong long-range interactions. In the future, it would be advantageous to increase the number of sites to explore mean-field and quantum mechanical effects due to the soft-core interaction on a larger scale.

Chapter 5

Hyperchaos in a Bose-Hubbard chain with Rydberg-dressed interactions

In this chapter we study chaos and hyperchaos of Rydberg-dressed Bose-Einstein condensates (BECs) in a one-dimensional optical lattice. Due to the long-range soft-core interaction between the dressed atoms, the dynamics of the BECs are described by the extended Bose-Hubbard model, similar to Chap. 4. In the mean-field regime, we analyze the dynamical stability of the BEC by focusing on the groundstate and localized state configuration. Lyapunov exponents of the two configurations are calculated by varying the soft-core interaction strength, potential bias and length of the lattice. Both configurations can have multiple positive Lyapunov exponents, exhibiting hyperchaotic dynamics. We show the dependence of the number of the positive Lyapunov exponents and the value of the largest Lyapunov exponent on the length of the optical lattice. The largest Lyapunov exponent is directly proportional to areas of phase space encompassed by the associated Poincaré sections. We demonstrate that linear and hysteresis quenches of the lattice potential and the dressed interaction lead to distinct dynamics due to the chaos and hyperchaos. Our work is relevant to current re-

search on chaos, and collective and emergent nonlinear dynamics of BECs with long-range interactions. Several sections of the following chapter have been transcribed verbatim, along with the accompanying data and figures, from the following publication:

"Hyperchaos in a Bose-Hubbard chain with Rydberg-dressed interactions"

G. McCormack, R. Nath, and W. Li

Photonics, **8** 554, 2021 [148]

5.1 Introduction

Over the past two decades, Bose-Einstein condensates (BECs) of ultracold atomic gases have become an ideal system to study both quantum and nonlinear dynamics, due to the high controllability over the two-body interactions [90], trapping potentials [9] and spatial dimensions [91, 92], along with long coherence times. The emerging nonlinear phenomena depend strongly on the two-body interactions between atoms. In the presence of s-wave interactions, BECs can form dark and bright soliton [149–156] and exhibit Newton's cradle behavior [157], which are paradigmatic examples in nonlinear physics. In trap array and optical lattice settings, self-trapping of the BEC emerges due to strong repulsive interactions [88, 111–116, 158–160], where the BEC is localized in a single site. This is in contrast to the homogeneous superfluid state, which forms the groundstate of an infinite lattice when the interaction is weak [75, 161, 162]. Both the homogeneous and self-trapped states correspond to solutions, i.e. *fixed points*, of the discrete Gross-Pitaevskii (GP) equation [96]. The stability of these fixed points depends on various parameters, such as the s-wave interaction. It has been shown that the self-trapped state in a double-well potential can only be stable when the onsite interaction strength is much stronger than the tunneling strength [111]. Nonetheless, the homogeneous state can be disturbed by the s-wave interaction and external potentials, giving rise to chaotic dynamics [163, 164]. Under strong

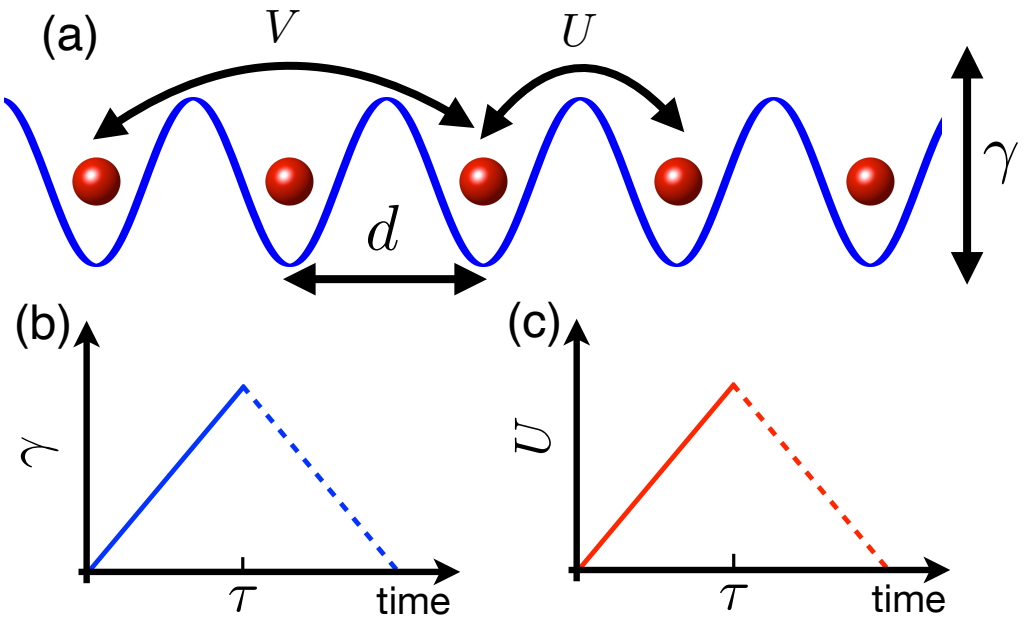

Figure 5.1: *(Color online)* ***The extended Bose-Hubbard chain and quenching schemes.*** *(a) Nearest-neighbor (U) and next-nearest-neighbor (V) interactions between atoms in a one dimensional optical lattice (lattice constant d). The tilting of the lattice is denoted by the parameter γ. We consider a linear quench in (b) γ and (c) U towards a non-zero value (solid). When γ (U) returns to the initial value (both solid and dashed), this is a hysteresis quench. The rate to quench γ (U) is α (β) . See text for details of the soft-core interaction and quenching protocols.*

periodic modulation of the hopping, extended chaotic regions are found in phase space [165].

On the other hand, long-range interactions play important roles in determining the dynamical stability of BECs. Solitons may occur in BECs in the presence of dipolar interactions [166–170]. The competition between s-wave and dipolar interactions [124, 125, 127] leads to bifurcations in the eigenspectra and to chaotic dynamics, when confined in harmonic traps [171, 172]. Self-trapping of dipolar BECs in double-well [173–176] and triple-well potentials [177–179] have been examined theoretically. Besides the dipolar interaction, one can laser-couple groundstate atoms to high-lying Rydberg states [25, 27, 34, 37, 180–183], which induces a long-range *soft-core* interaction between two dressed atoms (with a distance r) [see Chapter 2].

In chapter 4 we have shown that self-trapping dynamics of Rydberg-dressed BECs can be controlled in a triple-well potential through mean-field and quantum me-

chanical analysis. In this chapter, we investigate chaotic properties of Rydberg-dressed BECs in a one-dimensional (1D) optical lattice in which the dressed interaction leads to a multi-site density-density interaction. In the semiclassical regime, the nonlinear dynamics of the Bose-Hubbard model is captured by a discrete, coupled GP equation. Nonlinear eigenenergies, Bogoliubov spectra as well as Lyapunov exponents of the dressed BEC in the lattice are investigated. We then explore dynamical stability of the groundstate and localized state, where dependence of the largest, and total number of positive Lyapunov exponents [184, 185] on the dressed interaction and system size is explored. We probe the chaotic dynamics by employing both linear and a hysteresis quench of the potential bias and dressed interaction [120, 186, 187].

The chapter is organized as follows. In Sec. 5.2 the Hamiltonian of the Bose-Hubbard chain is introduced. The corresponding mean-field approximation and GP equations are given. Methods on calculating the eigenenergy, Bogoliubov spectra and Lyapunov exponents are briefly introduced. Quench schemes of the potential bias and nonlinear interaction are explained. We explore static (eigenenergies and Bogoliubov spectra) and dynamical properties (Lyapunov exponents) of the groundstate and localized state configurations in Sec. 5.3, and Sec. 5.4, respectively. Dynamics driven by both the linear and hysteresis quenching parameters are explored with different initial states. In Sec. 5.5 we examine the scaling of the Lyapunov exponents with the system size for the two different configurations. We demonstrate through numerical calculations that areas of the Poincaré sections scale almost linearly with the largest Lyapunov exponent. We conclude our work in Sec. 5.6.

5.2 Model and method

5.2.1 Extended Bose-Hubbard model in the semiclassical limit

Our setting consists of N bosonic atoms confined in a one-dimensional lattice with lattice constant d, as depicted in Fig. 5.1(a). The Rydberg-dressing induces long-range interactions between atoms at different sites. Taking into account the hopping between nearest-neighbor sites, we obtain an extended Bose-Hubbard Hamiltonian of L sites [181]

$$\hat{H} = -J\sum_{\langle i,j\rangle}^{L}\hat{a}_i^\dagger\hat{a}_j + \sum_{j}^{L}\Gamma_j\hat{n}_j + \frac{1}{2}\hat{H}_{\text{int}}, \tag{5.1}$$

where $\hat{a}_j(\hat{a}_j^\dagger)$ is the bosonic annihilation (creation) operator at site j. This setup is analogous to the Hamiltonian introduced in Sec 4.41, except we are no longer restricted to $L = 3$ sites. The tunneling strength J acts only on nearest-neighbor sites, denoted by $\langle\cdot\rangle$ in the summation. Here, $\hat{n}_j = \hat{a}_j^\dagger\hat{a}_j$ is the number operator, while Γ_j is the local tilting potential. A more general relation for the local tilting potential is given by $\Gamma_j = -\gamma\left(j - 1 - \lfloor L/2\rfloor\right)$, where $\lfloor\cdot\rfloor$ and γ are the floor function and level bias between neighboring sites, respectively. The onsite and long-range interactions are described by $\hat{H}_{\text{int}} = g\sum_j^L \hat{n}_j\left(\hat{n}_j - 1\right) + \sum_{i,j}^L \Lambda_{i,j}\hat{n}_i\hat{n}_j$. In this chapter, we will again restrict ourselves to the onsite, nearest-neighbor ($\Lambda_{j,j\pm1}$) and next-nearest-neighbor ($\Lambda_{j,j\pm2}$) interactions, where $R \sim d$. This approximation is valid as the soft-core interaction decays rapidly when the separation between sites is larger than the soft-core radius.3

In the semiclassical limit $N \gg 1$, we employ the mean-field approximation where the bosonic operator is described by a classical field ψ_j, i.e. $\hat{a}_j \approx \psi_j\sqrt{N}$, and $\hat{a}_j^\dagger \approx \psi_j^*\sqrt{N}$, with the normalization condition $\sum_j |\psi_j|^2 = 1$. This yields the

semiclassical Hamiltonian $\mathcal{H} \approx \hat{H}/N$,

$$\begin{aligned}\mathcal{H} &= \sum_j^L \Gamma_j|\psi_j|^2 - J\sum_j^L \left(\psi_{j+1}^*\psi_j + \psi_{j-1}^*\psi_j\right) \\ &\quad + \frac{N}{2}\sum_{i,j}^L |\psi_j|^2\left[g\left(|\psi_j|^2 - 1\right) + \Lambda_{i,j}|\psi_i|^2\right]. \end{aligned} \tag{5.2}$$

The dynamics of the classical field ψ_j is obtained via the canonical equation $id\psi_j/dt = \partial\mathcal{H}/\partial\psi_j^*$, yielding the coupled GP equations

$$\begin{aligned}i\dot{\psi}_j &= -J\left(\psi_{j+1} + \psi_{j-1}\right) + \big[\Gamma_j + W|\psi_j|^2 + \\ &\quad U\left(|\psi_{j+1}|^2 + |\psi_{j-1}|^2\right) + V\big(|\psi_{j+2}|^2 + |\psi_{j-2}|^2\big)\big]\psi_j, \end{aligned} \tag{5.3}$$

where we have defined $W = N(\Lambda_{j,j} + g)$, $U = N\Lambda_{j,j\pm1}$, and $V = N\Lambda_{j,j\pm2}$, to be the onsite, nearest-neighbor and next-nearest-neighbor interaction strength. The onsite interaction W takes into account contributions from both the s-wave and soft-core interaction. We will assume a vanishing onsite interaction, i.e. $W = 0$ which allows us to focus on effects induced by the long-range interaction part. To be concrete, we will fix the nearest-neighbor and next-nearest-neighbor interaction to be $U = 2V$ in the following discussion. Time and energy will be scaled with respect to $1/J$ and J in what follows.

It is convenient to examine the real ($\mathcal{R}_j = \mathrm{Re}[\psi_\mathrm{j}]$) and imaginary components ($\mathcal{I}_j = \mathrm{Im}[\psi_\mathrm{j}]$) of ψ_j,

$$\begin{aligned}\dot{\mathcal{R}}_j &= -J\left(\mathcal{I}_{j+1} + \mathcal{I}_{j-1}\right) + \big[\Gamma_j + W|\psi_j|^2 + \\ &\quad U\left(|\psi_{j+1}|^2 + |\psi_{j-1}|^2\right) + V\big(|\psi_{j+2}|^2 + |\psi_{j-2}|^2\big)\big]\mathcal{I}_j, \end{aligned} \tag{5.4}$$

$$\begin{aligned}\dot{\mathcal{I}}_j &= J\left(\mathcal{R}_{j+1} + \mathcal{R}_{j-1}\right) - \big[\Gamma_j + W|\psi_j|^2 + \\ &\quad U\left(|\psi_{j+1}|^2 + |\psi_{j-1}|^2\right) + V\big(|\psi_{j+2}|^2 + |\psi_{j-2}|^2\big)\big]\mathcal{R}_j, \end{aligned} \tag{5.5}$$

with $|\psi_j|^2 = \mathcal{R}_j^2 + \mathcal{I}_j^2$. Both $\mathcal{R}_j$ and $\mathcal{I}_j$ are real valued functions of time. We will calculate Lyapunov exponents and the Poincaré sections based on these real

functions. Note that $\mathcal{R}_j$ and $\mathcal{I}_j$ represent mean values of the quadrature of the operator $\hat{a}_j$. The quadrature fulfills the commutation relation similar to the position and momentum operator [188]. Hence the mean values of the quadrature allow us to obtain useful information on the dynamics of the system in phase space. For small systems, $L = 2$ or 3, one can also describe the classical field with the canonical phase and particle number decomposition [116, 189].

5.2.2 Nonlinear eigenenergies and Bogoliubov spectra

Though the Hamiltonian (5.2) is Hermitian, the density-dependent nonlinearity prevents us from calculating the eigenenergy through conventional diagonalization. To overcome this, a shooting method will be employed to numerically evaluate the eigenstate $\bar{\Psi}_j = [\bar{\psi}_1, \bar{\psi}_2, \cdots, \bar{\psi}_L]$ and corresponding eigenenergy ε_j self-consistently [86]. A trial solution is seeded into the semiclassical Hamiltonian. It is then diagonalized, leading to a new eigenstate and eigenenergy. This process is iterated until the resulting eigenstate and eigenenergy is obtained self-consistently.

For interacting systems, one can analyze the Bogoliubov spectra ϵ_B to understand the stability of the eigenstate. This is achieved by linearizing around a given state $\bar{\Psi}$ (e.g., a fixed point of the semiclassical system), where each component is given by $\psi_j = \bar{\psi}_j + u_j e^{-i\epsilon_B t} - v_j^* e^{i\epsilon_B t}$, with u_j and v_j being the probability amplitudes of the Bogoliubov quasiparticles [9]. The dynamics of u_j and v_j are described by the Bogoliubov equations [118, 119],

$$\begin{pmatrix} \mathcal{L} & \mathcal{N} \\ -\mathcal{N} & -\mathcal{L} \end{pmatrix} \begin{pmatrix} \mathbf{u} \\ \mathbf{v} \end{pmatrix} = \epsilon_B \begin{pmatrix} \mathbf{u} \\ \mathbf{v} \end{pmatrix} \tag{5.6}$$

where $\mathcal{L} = \tilde{H}_0 + 2U\mathcal{P} - \mu$, and $\mathcal{N} = -U\mathcal{P}$. $\tilde{H}_0$ and $\mathcal{P}$ are $L \times L$ block matrices. From Eq. (5.3), we obtain the matrix elements $\langle\psi_j|\tilde{H}_0|\psi_j\rangle = \Gamma_j$, $\langle\psi_j|\tilde{H}_0|\psi_{j\pm1}\rangle = -J$, $\langle\psi_j|\mathcal{P}|\psi_j\rangle = |\bar{\psi}_{j+1}|^2 + |\bar{\psi}_{j-1}|^2 + (|\bar{\psi}_{j+2}|^2 + |\bar{\psi}_{j-2}|^2)/2$, $\langle\psi_j|\mathcal{P}|\psi_{j\pm1}\rangle = 2\bar{\psi}_{j\pm1}\bar{\psi}_j$ and $\langle\psi_j|\mathcal{P}|\psi_{j\pm2}\rangle = \bar{\psi}_{j\pm2}\bar{\psi}_j$, while other matrix elements are zero. If the Bogoli-

ubov spectra are complex numbers, the state is then *dynamically unstable*, as Bogoliubov quasiparticles grow (decay) exponentially with time, at a rate that is determined by the imaginary part of the spectra.

5.2.3 Poincaré sections and Lyapunov exponents

The emergence of chaos in the dynamics can be characterized by the Poincaré sections and Lyapunov exponents. For L sites, the possible trajectories are the complete set of $\{\mathcal{R}_1, \cdots, \mathcal{R}_L, \mathcal{I}_1, \cdots, \mathcal{I}_L\}$. Due to the normalization condition, we need to solve a $2L-1$ dimensional system to obtain the dynamics. It is difficult to comprehend the stability of the trajectories in such a high dimensional phase space. Instead, we project the dynamics to a two dimensional (2D) Poincaré section to identify the dynamical properties. To calculate the 2D Poincaré section, we record trajectories of selected variables ($\mathcal{R}_j$, $\mathcal{I}_j$) as they cut through the $\mathcal{U}_k$-plane ($j \neq k$), provided that $\dot{\mathcal{U}}_k > 0$. These intersecting points form the 2D Poincaré section. To be specific, we will evaluate the Poincaré section of variable ($\mathcal{R}_2$, $\mathcal{I}_2$) on the $\mathcal{U}_1$ plane.

The strength of chaos can be measured by the Lyapunov exponents associated with the equations of motion [184, 185]. The Lyapunov exponents give the rate of separation between trajectories for a given initial state. As the Lyapunov exponents depend on the initial state, we will consider both the groundstate and a localized state initially. In a localized state, nearly all the condensate sits in a single site, which can be stable (i.e. the self-trapping state) when the nonlinear interaction is strong. In this work, the Lyapunov exponents λ_j ($j = 1, \cdots, 2L$) are calculated via DynamicalSystems.jl, a fast and reliable Julia library to determine the dynamics of nonlinear systems [190]. We have checked that it gives data consistent with the method in Ref. [184]. When there exists at least one positive Lyapunov exponent the trajectories will separate exponentially, leading to chaotic dynamics. The dynamics is classed as hyperchaotic when there are more than two positive Lyapunov exponents [185].

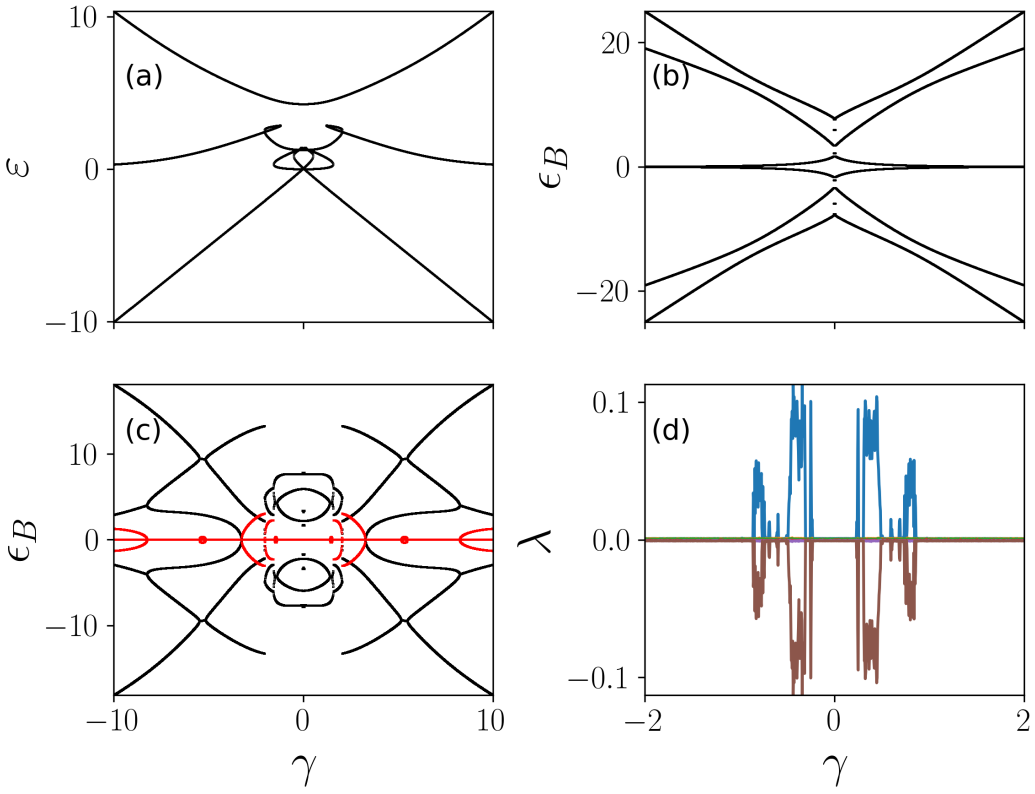

Figure 5.2: ***Eigenenergies, Bogoliubov spectra and Lyapunov exponents when varying the tilt*** γ***.*** *We show (a) the nonlinear eigenenergy, Bogoliubov spectra of (b) the groundstate and (c) the first excited state , and (d) the Lyapunov exponents of the groundstate. The nonlinearity dominates when* $|\gamma|$ *is small, leading to loops in the eigenenergy. The Bogoliubov spectra are all real when the system is in the groundstate (b). The Bogoliubov spectra have complex components (red region) when the system is in the first-excited state. Positive Lyapunov exponents indicate the system exhibits chaos dynamically, which appear mostly in the loop region of the eigenenergy. Parameters are* $L = 3$ *and* $U = 2V = 5$*.*

5.2.4 Quenching schemes

In Sections. 5.3 and 5.4 we will explore the dynamics of the system with time-dependent parameters via the following quenching schemes.

***Scheme* I**: First we consider a linear quench of the potential bias [86]. The bias between two neighboring sites is given by the function

$$\gamma_L = \gamma_i + \alpha t, \tag{5.7}$$

where γ_i and α are the initial value and quench rate, respectively. With $\gamma_i < 0$, the quench takes place from $t = 0$ to $t = 2\gamma_f/\alpha$ with $\gamma_f = -\gamma_i$, depicted by the solid curve in Fig. 5.1(b).

***Scheme* II** : Alternatively, we consider a hysteresis quench [120, 186, 187] where the system begins at γ_i and then evolves towards γ_f. At time $\tau = \gamma_f/\alpha$, the potential bias is quenched back towards γ_i. The function describing this scheme is

$$\gamma_H = \gamma_f + (\gamma_i - \gamma_f)\frac{|\tau - t|}{\tau}. \tag{5.8}$$

The corresponding scheme is shown by the solid and dashed curve in Fig. 5.1(b).

***Scheme* III** : In addition to quenching the level bias we also change the two-body interaction strength through a linear ramp,

$$U_L = U_i + \beta t \tag{5.9}$$

where U_i is the initial interaction strength and β is the quench rate. This is shown by the solid curve in Fig. 5.1(c). Note that the next-nearest-neighbor interaction V depends on time as well due to the relation $U = 2V$.

***Scheme* IV** : The hysteresis counterpart of the interaction quench is given by

$$U_H = U_f + (U_i - U_f)\frac{|\tau' - t|}{\tau}, \tag{5.10}$$

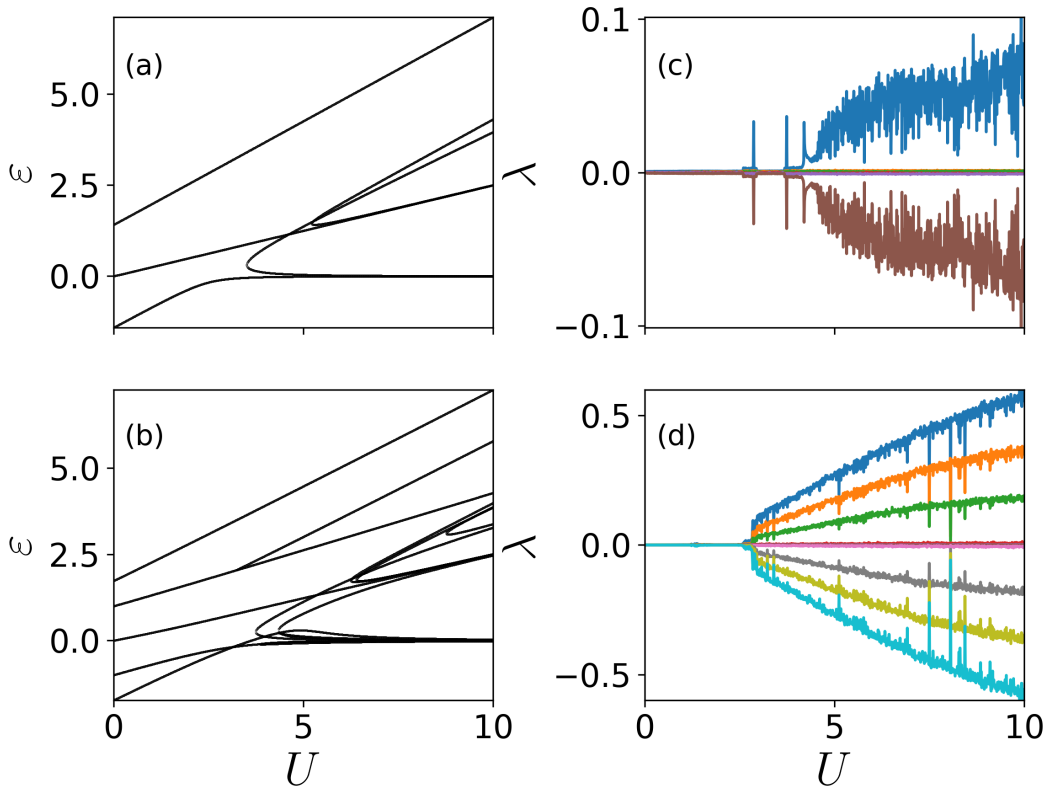

Figure 5.3: ***Eigenenergies and Lyapunov exponents as a function of*** U***.*** *We show eigenenergy for (a)* $L = 3$ *and (b)* $L = 5$ *when the trap is balanced (*$\gamma = 0$*). Level crossings are found when the interaction is strong. Starting from the groundstate, we calculate Lyapunov exponents for (c)* $L = 3$ *and (d)* $L = 5$*. For a given* U*, Lyapunov exponents of same value but opposite signs appear in pairs.*

where U_f is the final interaction strength, with $\tau' = U_f/\beta$.

5.3 Stability of the groundstate

5.3.1 Eigenenergies, Bogoliubov spectra and Lyapunov exponents

Without the nonlinearity, the number of eigenenergies N_ϵ is identical to L, the dimension of the semiclassical system. The number of eigenenergies can be larger than L when the interaction is strong. As an example, eigenenergies for $L = 3$ as a function of the bias γ are shown in Fig. 5.2(a). We find $N_\epsilon > L$ when $|\gamma| \lesssim U$, where the nonlinearity dominates. Loops and crossings appear in the eigenenergies, except in the highest energy level.

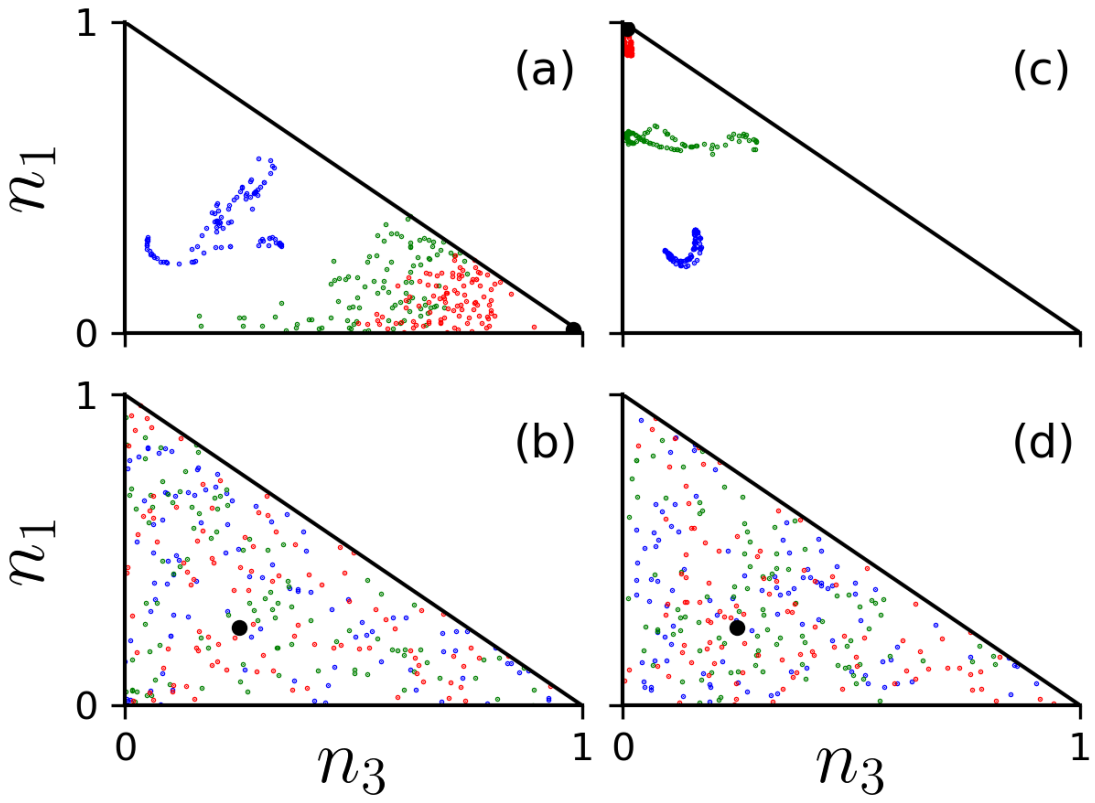

Figure 5.4: *(color online)* ***Final population distribution for the groundstate.*** *The population by quenching γ with (a) scheme* **I** *and (b) scheme* **II** *is shown for $L = 3$. In the numerical simulation, $\gamma_i = -\gamma_f = -10$ and the interaction strength is $U = 5$. The interaction U is quenched with (c) scheme* **III** *and (d) scheme* **IV** *where $U_i = 0$, $U_f = 10$ and $\gamma = 0$, respectively. In all the figures, the quench rates (α or β) are* 1 *(blue),* 0.1 *(green), and* 0.01 *(red). The total number of trajectories is $M = 100$. The target final state is shown as the large black circle.*

For a given state of the nonlinear system, one obtains $2L$ Bogoliubov spectra, whose values depend on the specific eigenstate and nonlinear interaction strength. The Bogoliubov modes are stable for all γ when the system is in the groundstate, i.e., the Bogoliubov spectra ϵ_B are real, as shown in Fig. 5.2(b). This is in contrast to excited eigenstates, whose Bogoliubov spectra have imaginary components. As an example, the Bogoliubov spectra of the first excited state is shown in Fig. 5.2(c). The corresponding Bogoliubov mode will decay (grow) exponentially, when the imaginary part is negative (positive).

The chaotic dynamics of the system is characterized by positive Lyapunov exponents. In Fig. 5.2(d) Lyapunov exponents are shown for the groundstate of the system. When increasing γ, negative and positive Lyapunov exponents are

found in regions where the eigenenergies show loops. The negative and positive Lyapunov exponents appear in pairs with the same absolute values, as our system is conservative. In this example, one positive Lyapunov exponent can be found when $|\gamma| < 1$, indicating the presence of chaos. This means that small fluctuations on the groundstate could gain exponential growth, and hence drives the system away from the groundstate.

To further understand roles played by the nonlinearity, we calculate eigenenergies as a function of the interaction strength U shown in Fig. 5.3(a) and (b), for $L = 3$ and $L = 5$, respectively. It can be seen that new branches are generated when the nonlinear interaction U is large enough. Lyapunov exponents of the groundstate of the nonlinear system are shown in Figs. 5.3(c) and 5.3(d). Positive Lyapunov exponents are found in the strongly interacting region, whose values increase with increasing U. Larger Lyapunov exponents mean that the exponential growth of the instability can be even faster. Importantly, the number of Lyapunov exponents now depends on L. For $L = 3$, one obtains a single positive Lyapunov exponent when $U \gtrsim 4$. When $L = 5$, there are 3 positive Lyapunov exponents. This indicates that the system enters the so-called *hyperchaos* regime [191–193], where more than one positive Lyapunov exponents can be found in the dynamics. In the two examples, we obtain maximally $L - 2$ positive Lyapunov exponents, as the energy and particle number is conserved in the Bose-Hubbard chain.

5.3.2 Quench dynamics

In the linear regime, dynamics of the system will follow the eigenstate adiabatically when slowly quenching the tilt potential. However the dynamics may deviate from the adiabatic eigenstate in the nonlinear regime, especially when positive Lyapunov exponents are found. This will be illustrated through quenching the tilt potential and interaction strength given by Eqs. (5.7)-(5.10). To trigger the instability in the dynamics, we consider a thermal mixed state $\bar{\Psi}'_j = [\bar{\psi}_1 e^{i\theta_1}, \bar{\psi}_2 e^{i\theta_2}, \cdots, \bar{\psi}_L e^{i\theta_L}]$ around a given state $\bar{\Psi}_j$ (the groundstate), where θ_j

is a random phase distributed uniformly between 0 and 2π [120]. In numerical simulations, we typically consider an ensemble of $M = 100$ realizations with a given set of parameters.

We first examine a linear quench of the bias γ when the system is prepared in the groundstate at $\gamma_i = -10$ and $L = 3$. The majority of the condensate is located on the first (leftmost) site $[n_1(0) = |\psi_1|^2 \approx 1]$ initially [Fig. 5.4(a)]. In the adiabatic limit and without the nonlinear interaction, the condensate will move to the third well, $n_3(\tau) \approx 1$, after the quench [86]. The population at this adiabatic limit is shown with a black dot in each panel. The quench dynamics however depend on the finite quench rate and the interaction strength. When the interaction is weak the condensate can be in any of the three sites, since the tunneling strength between neighboring sites plays the dominant role. The distribution of the final population is affected by the noise on the initial state and also depends on the final time in the simulations. Increasing U, the population is distributed into a larger region of phase space, i.e., it occupies a larger areas in the n_3-n_1 plane. By fixing the interaction U, our numerical simulation shows that the smaller α is, the closer the population distribution is to the adiabatic limit.

For the hysteresis quench given by Eq. (5.8), we see that even for $U = 5$ (meaning the eigenstate exhibits complicated level crossings) the density mostly returns to the initial state, at least when $\alpha \ll 1$ [Fig. 5.4(b)]. Here the hysteresis quench has allowed for a large level of *reversibility* in the dynamics [120], as the chaotic behaviour has not been triggered. Increasing the quench rate α, the population distributions cluster around much smaller regions in phase space, than the one shown in panel (a).

In Fig. 5.4(c) we quench the interaction according to Eq. (5.9). The initial states depend on the value of γ. For example the groundstate is $\bar{\Psi} = [0.5, 1/\sqrt{2}, 0.5]$ for $\gamma = 0$. The final states are highly dependent on the initial conditions, due to the chaos in the dynamics [see the crossing energy levels in Fig. 5.3 (a) and Lyapunov exponent in Fig. 5.3(c)]. We have verified that by increasing γ the

randomness associated with the final states decreases, as the number of crossings in the eigenenergy will decrease.

In case of the hysteresis quench of U, we find that the results [Fig. 5.4(d)] are similar to the linear quench. When looking at $\gamma = 0$, the final states do not return to the initial value. As shown in Fig. 5.3(c), the Lyapunov exponent of the groundstate becomes positive when $U \gtrsim 4$, which causes the final state to be more random, i.e. resulting in a broader distribution of the densities. As the tilt γ increases, we have verified that chaos is gradually suppressed, as the population localizes in the trap that corresponds to the lowest energy state. In order to trigger chaotic dynamics in the tilted case, stronger interactions are needed in general.

5.4 Stability of the localized state

5.4.1 Bogoliubov spectra and Lyapunov exponents

In this section, we will explore stability of a situation where the condensate is trapped in a single site. When localized at one end of the lattice, it corresponds to the groundstate if the lattice potential is strongly tilted $|\gamma| \gg 1$. We will examine dynamics of localized states even in the balanced case ($\gamma = 0$), partially motivated by the fact that the self-trapped state can be stabilized by strong nonlinear interactions. We will show that dynamical instabilities of localized states will depend strongly on the long-range interaction. To be concrete, we will consider a scenario where the condensate is confined in the second trap from the left of the lattice, i.e. $\bar{\Psi} = [0, 1, \cdots, 0]$. In the numerical simulations of the dynamics, uniform density fluctuations are applied to the lattice to trigger the hopping dynamics. This modifies the initial state to be $\bar{\Psi} = [\sqrt{\varepsilon/L}e^{\phi_1}, \sqrt{1-\varepsilon}e^{\phi_2}, \cdots, \sqrt{\varepsilon/L}e^{\phi_L}]$ with $\epsilon \ll 1$ and ϕ_j to be a random phase. This choice furthermore insures that the energy of different initial states are almost identical.

In Figs. 5.5(a) and (b), dynamical unstable regions in the Bogoliubov spectra for

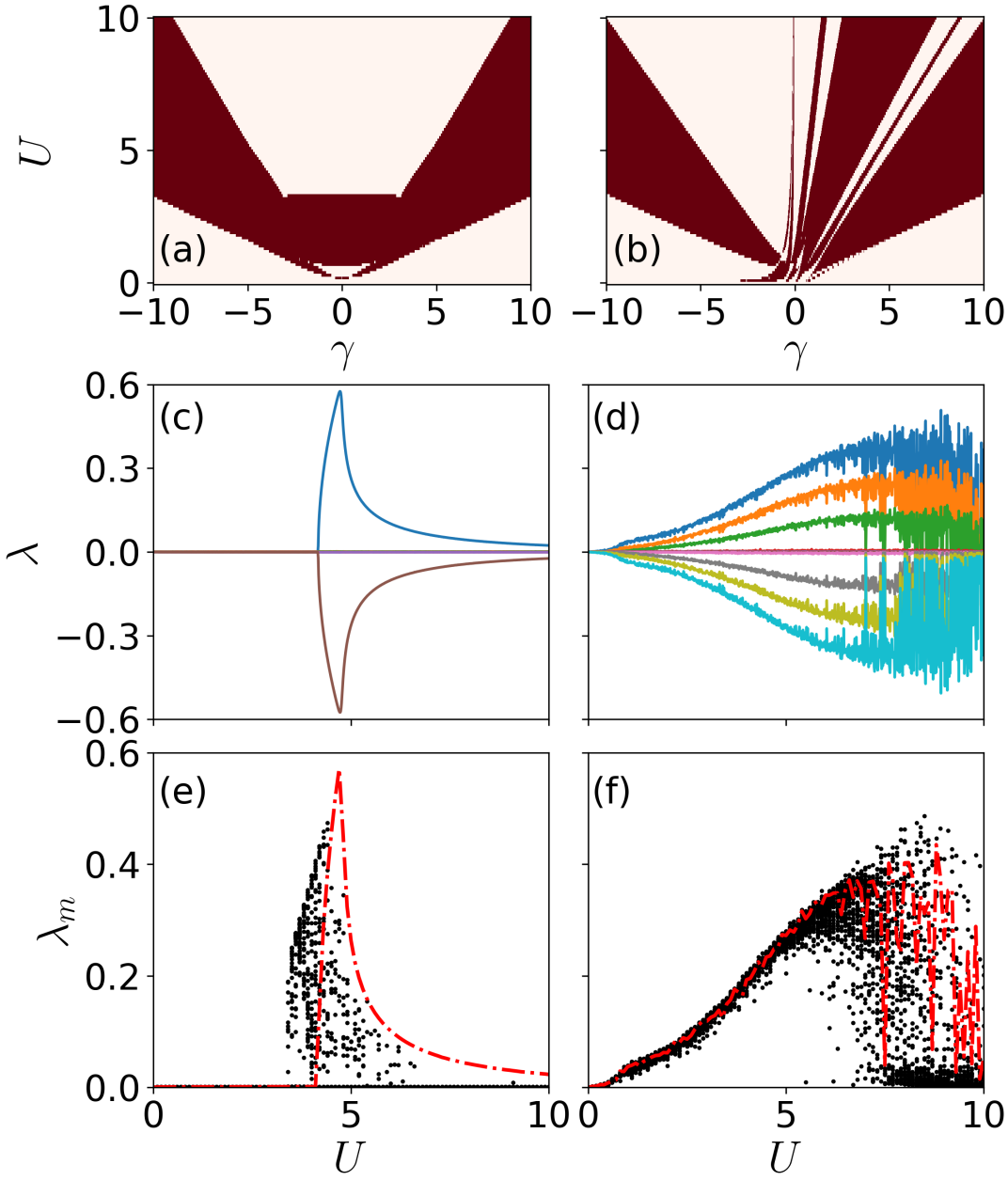

Figure 5.5: *(color online)* ***Bogoliubov spectra and Lyapunov exponents of the localized state.*** *Dynamically unstable regions (dark red) for (a) $L = 3$ and (b) L=5 are shown as a function of U and γ. Panels (c) and (d) give the Lyapunov exponents as a function of U. Random perturbation to the initial state are examined for (e) $L = 3$ and (f) $L = 5$. The red lines show the maximal Lyapunov exponents in (c) and (d), correspondingly. Here $\gamma = 0$ in panels (c)-(d).*

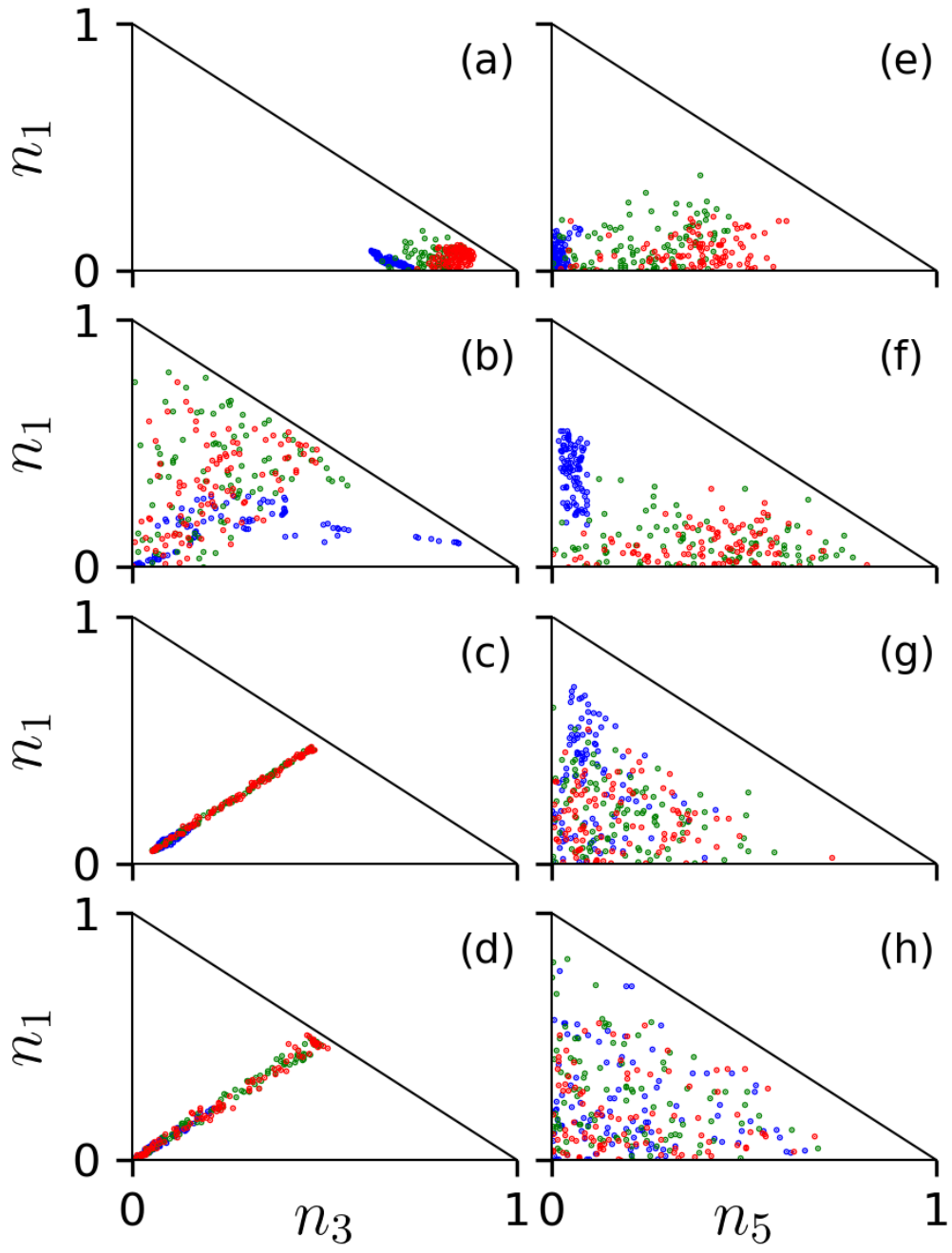

Figure 5.6: *(color online)* ***Final population distribution for the localized state.*** *The first and second row show the linear and hysteresis quench of γ. Here $U = 5$, $\gamma_i = -\gamma_f = 10$. The third and fourth row show the linear and hysteresis quench of U with $U_i = 0$, $U_f = 10$ and $\gamma = 0$. In (a)-(d) we consider three sites and the initial thermal state is $\bar{\Psi} = [0.1e^{i\phi_1}, \sqrt{0.98}e^{i\phi_2}, 0.1e^{\phi_3}]$ with ϕ_j $(j = 1, 2, 3)$ are random number in $[0, 2\pi]$. In (e)-(h) $L = 5$ and the initial state is $\bar{\Psi} = [\sqrt{0.005}e^{i\phi_1}, \sqrt{0.98}e^{i\phi_2}, \sqrt{0.005}e^{i\phi_3}, \sqrt{0.005}e^{i\phi_4}, \sqrt{0.005}^{i\phi_5}]$ with ϕ_j $(j = 1, \cdots, 5)$ being randomly distributed in $[0, 2\pi]$. The small fraction in sites other than the localized state is used to trigger the hopping dynamics. Other parameters are same with the one in Fig. 5.4.*

$L = 3$ and $L = 5$ are shown (highlighted with dark red color). In the unstable region, ϵ_B develops imaginary components, which depend on U, γ and L. In case of $L = 3$, the condensate is localized in the middle site initially, meaning the Bogoliubov spectra are symmetric with respect to γ. Fig. 5.5(a) shows that the system is dynamically unstable when U is small, in particular when the lattice is balanced ($|\gamma|$ is small). This is not surprising, as the localized state is not the groundstate, nor does the system support the self-trapped state. By increasing the interaction strength, we note that the localized state returns to a stable configuration when $|\gamma|$ is small. This means that the localized state becomes a stable, self-trapped state [86]. When $L = 5$, the dynamical stability now depends heavily on tilt γ. When $\gamma > 0$ there is a much broader range of unstable regions. This feature is largely due to the non-symmetric initial state having higher energies. Therefore we expect to see qualitatively different dynamics in the various quenching schemes.

The Lyapunov exponents exhibit sensitive dependence on the system size. As shown in Fig. 5.5(c) the Lyapunov exponents for $L = 3$ show an unusually symmetric shape when $U \gtrsim 4$. The exponents are a smooth function of U, and reach maximal value around $U = 5$. Further increasing U, the positive Lyapunov exponents decrease. This indicates that the localized configuration could exhibit chaotic dynamics for large U. For $L = 5$ we notice that positive Lyapunov exponents can be found when U is relatively small. A key difference is that there are multiple positive Lyapunov exponents [Fig. 5.5(d)], where the nonlinear dynamics enters the hyperchaotic regime.

To understand the maximal Lyapunov exponents, we slightly alter the initial state so that we have $\bar{\Psi} = \left[\varepsilon, \sqrt{1-2\varepsilon^2}, \varepsilon, \cdots, 0\right]$, where ε is a small perturbation to the wavefunction of the traps on either side of the localized site, with $0 < \varepsilon < 0.01$. In Fig. 5.5(e) and (f) [corresponding to $L = 3$ and 5] the largest Lyapunov exponent λ_m (red) and Lyapunov exponents obtained with modified initial states (black) are shown (only the positive branch). It shows that a minor change to

the initial state will change Lyapunov exponents significantly. However λ_m gives an approximate upper bound for all the Lyapunov exponents.

5.4.2 Quench dynamics

For $U = 5$ and $L = 3$, a linear quench [Fig. 5.6(a)] from $\gamma_i = -10$ to $\gamma_f = 10$ shows strong self-trapping behavior in the rightmost potential. We expect that by performing a hysteresis quench back towards γ_i, the population would localize in the leftmost site again. However from Fig. 5.6(b) we see that the final state is rather chaotic. Due to the dynamical instability and chaos near $|\gamma| < 1$, the final state deviates from the initial state. In panels (c) and (d) we quench according to Eqs. (5.9) and (5.10) respectively. The dynamics show that in both cases the localized initial state loses population to the outer potential wells in an approximately equal manner for both the linear and hysteresis quenches. The strong nonlinear interactions in the initial localized trap repel the condensate symmetrically to the two neighboring traps. Additionally, we notice that in panel (d) the population could be $n_1 = n_3 \approx 0$, meaning that the final state is exactly equal to the initial state. We have achieved fully reversible with the hysteresis dynamics in these simulations. As shown in panel (c), this is not the case where the populations are always $n_1 \approx n_2 > 0$, implying that the strong two-body interactions prevent a complete localization of the condensate on a single site.

We now move on to examine the dynamics for the five site system. Without two-body interactions, linearly quenching from γ_i to γ_f will force the atoms towards the rightmost trap. However from Fig. 5.6(e) we see that the occupation is never very much greater than $n_5 \approx 0.5$, even for the slowest quenching rates considered in the simulation. When the quench rate is fast ($\alpha \sim 1$), we find less occupation in both the first and last site, implying the occupation has been spread amongst the remaining sites. In panel (f), the hysteresis counterpart is shown. Now the population should tend towards $n_1 \approx 1$. However this is not what is found in the numerical simulations. The populations distribute randomly in all sites. In panels

(g) and (h), the dynamics is qualitatively different from the $L = 3$ scenario. The symmetry between the densities of the two outermost sites is lost completely, and is replaced with a chaotic distributions, largely due to the presence of hyperchaos [see Fig. 5.5(d)].

5.5 Scaling of Lyapunov exponents with the system size

In the following we will investigate how the maximal and total number of Lyapunov exponents depend on the system size and initial state, focusing on parameter regimes where the nonlinear interaction can not be neglected, i.e. chaos and hyperchaos are expected in the dynamics. In general Lyapunov exponents depend on the input state of the calculation [184]. Two different initial states, i.e. the groundstate and the localized state, will be examined in detail.

In Fig. 5.7(a) the largest Lyapunov exponent λ_m for the groundstate configuration is shown. When $2 \leq L \leq 4$, the values of λ_m are small in general. This is due to the fact that chaos has not been triggered [see Fig. 5.5(b) and (c)]. When $L > 4$, the situation changes as chaos is already found with the given U. We find λ_m decreases gradually when $U = 3$ and $U = 5$ for larger L. On the other hand, the total number of positive Lyapunov exponents η is seen to increase almost linearly with L when $U = 3$ and $U = 5$, depicted in Fig. 5.7(b). Importantly, $\eta > 2$ when $L > 4$ for both $U = 3$ and $U = 5$, i.e. the dynamics is hyperchaotic. On the other hand, η decreases and deviates from the linear dependence on L when L is large, e.g. at $L = 10$ when $U = 3$ and $L = 14$ when $U = 5$. In general the linear relation holds up to a larger L for larger U. Recently it has been shown that the largest Lyapunov exponents in the BHM can be obtained from the echo dynamics of the condensate [194]. A similar technique could be applied to extract the largest Lyapunov exponents studied here.

Figs. 5.7(c) and (d) show both λ_m and η for the the localized state. In this

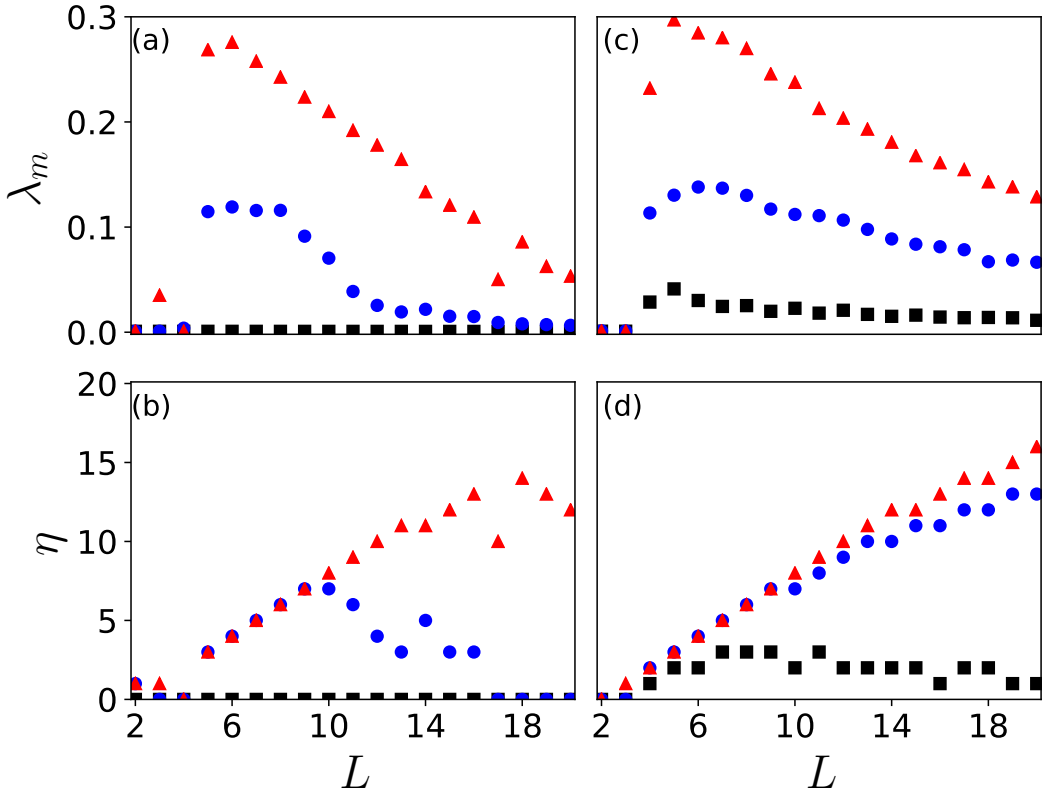

Figure 5.7: *(color online)* ***Lyapunov Exponents vs System Size.*** *The maximum Lyapunov exponent and total number of positive Lyapunov exponents are shown in (a) and (b) for the groundstate configuration. Panels (c) and (d) show the same quantity for the localized state. The larger U is, the larger the maximal Lyapunov exponent. The maximal Lyapunov exponent decreases with increasing L. The number of Lyapunov exponents increases and then decreases with increasing L. For the localized state, η increases nearly linearly with increasing L. In each panel, $U = 1$ (black squares), 3 (blue circles) and 5 (red triangles).*

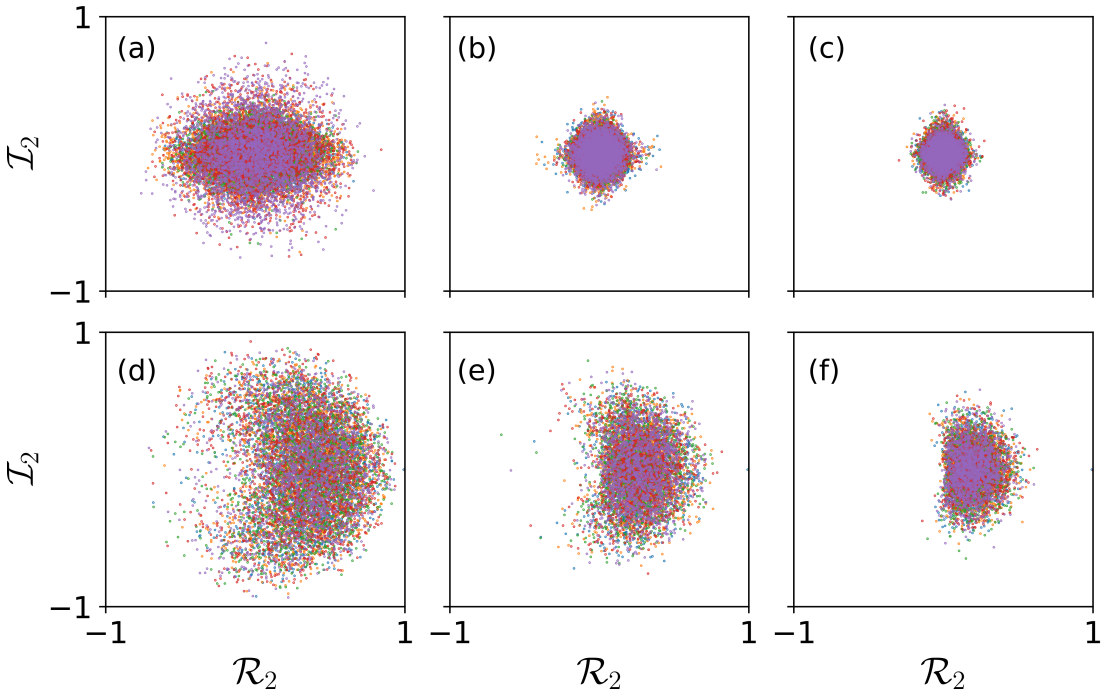

Figure 5.8: *(color online)* ***Poincaré Sections of the groundstate and localized state on the*** $\mathcal{U}_1$***-plane.*** *The Poincaré sections are shown for the groundstate (a-c) and the localized state (d-f). Each point represents a numerical realization. We consider* $L = 5$ *(a,d),* $L = 10$ *(b,e), and* $L = 20$ *(c,f). Other parameters are* $U = 3$ *and* $\gamma = 0$*.*

case, λ_m is largest when $L = 5$, and decreases with increasing L for $U = 3$ and $U = 5$. Compared to the groundstate, a visible difference is that $\lambda_m \neq 0$ when $U = 1$ for the localized state. Their values, however, are smaller than the one for $U = 3$ and $U = 5$. This implies that it will be difficult to observe chaotic dynamics with this level of nonlinear interactions. On the other hand, η increases with increasing U. When $L > 10$, η still increases with L, but slightly deviates from the linear scaling with L. A similar dependence is also found for stronger nonlinear interactions, as demonstrated with $U = 5$ in panel (d). For such state, $\eta > 1$ can be seen even with relatively weak interaction (e.g. $U = 1$), leading to more pronounced hyperchaotic dynamics.

The total number of nonlinear differential equations is $2L$ (the real and imaginary parts of ψ_j). For conserved systems, the number of positive and negative Lyapunov exponents are the same, and the sum of the Lyapunov exponents is zero. These features can be seen, e.g., in Fig. 5.2(d). Our numerical simulations show that the maximal number of positive Lyapunov exponents is $L - 2$ [see

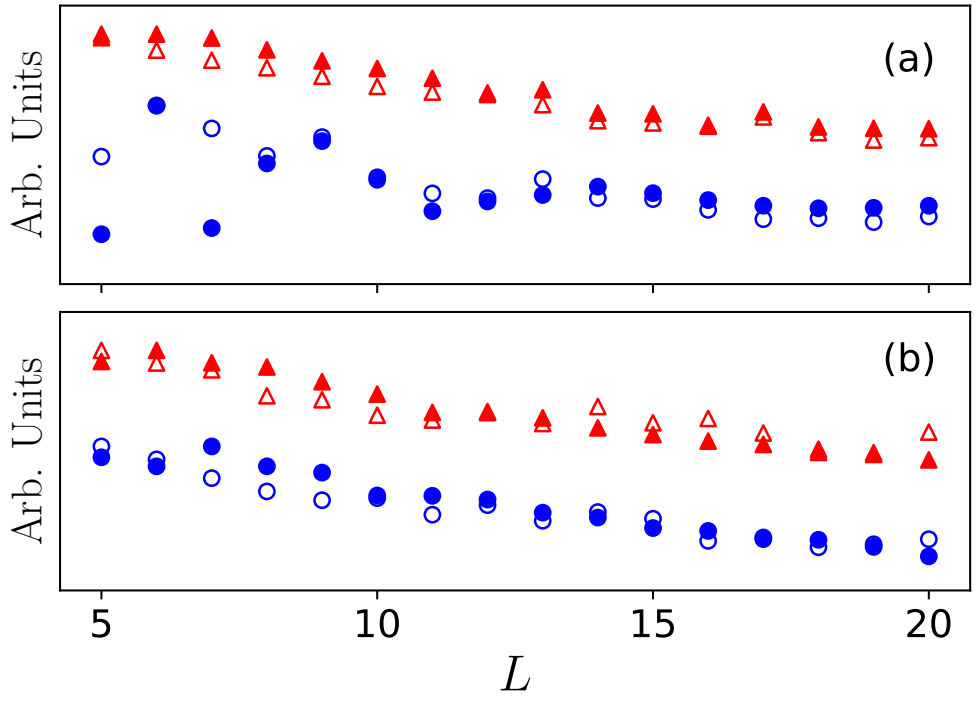

Figure 5.9: *(color online)* ***Areas of the Poincaré Sections****. We compare the fitted area (open shapes) of the Poincaré section with λ_m (solid) for both the groundstate (a) and localized state (b), respectively. The blue circles are for $U = 3$, and red triangles for $U = 5$. In both situations $\gamma = 0$.*

Fig. 5.7(b) when $U = 5$ and $L \leq 11$ and Fig. 5.7(d) when $U = 5$ and $L \leq 14$.]. As the extended Bose-Hubbard model is a Hamiltonian system, not only the sum of the Lyapunov exponents vanishes, but also conserved quantities, such as the energy and particle number, are found in the dynamics. This indicates that the maximal number of the Lyapunov exponents is $L-2$ but not L. For sufficiently large L, the total number of positive Lyapunov exponents is smaller than $L-2$, as the nonlinear interaction becomes smaller. For the groundstate, one can estimate the interaction energy for a given site to be $2(U+V)/L^2$ approximately, i.e. the mean local interaction energy decreases with increasing L.

The chaotic dynamics depend strongly on the largest Lyapunov exponents λ_m, which is considered as an indication of chaos in the dynamics. To illustrate this, the Poincaré section on the $\mathcal{U}_1$ plane for different system sizes is shown in Fig. 5.8, showing that profiles of the Poincaré section depend on the system size and the initial state. When $L = 5$ the area is largest [Fig. 5.8(a)] and decrease with

increasing L in case of the groundstate [Fig. 5.8(b) and (c)]. For different L, the profile of the Poincaré section is largely symmetric with respect to $\mathcal{R}_2 = 0$ and $\mathcal{I}_2 = 0$. In case of the localized state, similar dependence on L is found, as depicted in Fig. 5.8(d)-(f). We note two differences compared to the groundstate ones. First, the profile of the Poincaré section displays symmetry with respect to $\mathcal{I}_2 = 0$ but not $\mathcal{R}_2 = 0$. Second, the areas of the Poincaré section in the localized state are slightly larger, as the corresponding λ_m is larger [see Fig. 5.7(a) and (c)].

The area is largely determined by the largest Lyapunov exponent. To verify this, we find the area of the Poincaré section approximately through numerically fitting the Poincaré section, shown in Fig. 5.9. For the groundstate, the dependence of the fitted area and λ_m on L agrees well when $U = 5$. For $U = 3$, a good agreement is also found when $L \geq 8$. When $L = 5$ and $L = 7$, the fitted areas differ largely from the corresponding λ_m. This discrepancy might be caused by the fact that the relatively weak nonlinear interaction leads to uncertainties in calculating the Lyapunov exponent. For the localized state, the agreement is improved in general for both $U = 3$ and $U = 5$. This suggests that the discrepancy in the groundstate could be a boundary effect when L is small, as the localized state suffers less from the boundary effect.

5.6 Summary and outlook

We have investigated the chaotic and hyperchaotic dynamics of a one-dimensional Bose-Hubbard chain of Rydberg-dressed BECs in the semiclassical regime. We have shown that both the groundstate and localized state can have positive Lyapunov exponents, even though the corresponding Bogoliubov spectra are real valued. As a result, small perturbations to these states lead to large fluctuations, which are captured by the quench dynamics. We have found that hyperchaos emerges in both the groundstate and localized states when the nonlinear interaction is strong and L is large. The total number of positive Lyapunov exponents,

η, is bound by $L-2$ ($L \geq 3$). We have shown that η grows with the system size L when U is large. So far our investigations are focusing on the semiclassical regime. There has been an exploration into the relationships between chaos and quantum entanglement [195]. Moreover, quantum chaos can be seen by analyzing the statistics of eigenspectra on the Bose-Hubbard model with onsite [196] and long-range interactions [197, 198]. It is therefore worthwhile to explore features of chaos and hyperchaos due to the Rydberg dressed interaction in the quantum regime.

Chapter 6

Overview and conclusion

To conclude, we will first discuss the main outcomes of each chapter. Following that we will also discuss possible limitation of our findings, and what we believe would be acceptable steps to enrich the field of Rydberg-dressed bosonic dynamics.

6.1 Main contributions

In Chapter 3, we explored the dynamics of Rydberg-dressed bosonic atoms in free space. What was found was that the resulting dynamics showed a unique high frequency oscillation. This was attributed to the maxon modes being stable, a property not found in the long-range dipole-dipole interaction counterpart. We showed that this was possible due to the decay channel being blocked in the Rydberg-dressed case. In Chapter 4, we showed that when there are three optical traps in tandem, the condensates interact in a highly turbulent manner. The long-range interaction causes a bifurcation in the adiabatic eigenspectrum, when the interaction strength is strong with respect to the tunnelling strength. The results of this chapter provided a glimpse into the chaotic nature of coupled Rydberg-dressed BECs, and proved to be our starting point in chapter 5. Here we expanded our analysis to examine the Rydberg-dressed dynamics on a lattice chain of length L. We returned to the Bogoliubov equations first introduced in

chapter 3, and made use of the Lyapunov exponents, to determine that coupled Rydberg-dressed BECs are indeed hyperchaotic. We showed that the number of sites is directly correlated with the number of positive Lyapunov exponents. Additionally, we showed that the area encapsulated in phase space is inversely proportional to L.

6.2 Limitations and suggestions for further improvements

In Chapter 3, the high frequency maxon modes warrants more study. While we provided an insight into the dampening process, this was only a taster to qualitatively explain the results found. More research into Baliaev dampening is needed to truly understand the internal dynamics of a 3D BEC with Rydberg-dressed interactions.

Chapters 4 and 5 provided a means of exploring they chaotic dynamics of Rydberg-dressed atoms on a optical lattice. We show that Rydberg-dressing provides a means of controlling the interatomic interactions within a BEC. However, a caveat is that these systems are incredibly sensitive to minor perturbations in the ground state. Meaning that care needs to be taken when preparing the initial state. An appropriate next step would be to expand to higher dimensional lattices, where potentially the soft-core interaction may create unique spatial patterns in the BEC. Whether chaos is increased or decreased with the addition of higher dimensions is still undetermined.

Bibliography

[1] W. Ketterle and N. J. V. Druten, in *Advances In Atomic, Molecular, and Optical Physics*, Vol. 37 (Academic Press, 1996) pp. 181–236.

[2] D. Jaksch and P. Zoller, Annals of Physics **315**, 52 (2005).

[3] P. C. Hohenberg, Physical Review **158**, 383 (1967).

[4] K. B. Davis, M. O. Mewes, M. R. Andrews, N. J. van Druten, D. S. Durfee, D. M. Kurn, and W. Ketterle, Physical Review Letters **75**, 3969 (1995).

[5] C. C. Bradley, C. A. Sackett, J. J. Tollett, and R. G. Hulet, Physical Review Letters **75**, 1687 (1995).

[6] M. H. Anderson, J. R. Ensher, M. R. Matthews, C. E. Wieman, and E. A. Cornell, Science **269**, 198 LP (1995).

[7] E. L. Bolda, E. Tiesinga, and P. S. Julienne, Physical Review A - Atomic, Molecular, and Optical Physics **66**, 013403 (2002).

[8] N. P. Proukakis, S. A. Gardiner, M. J. Davis, and M. Szymanska, *Cold Atoms*, Vol. Volume 1 (IMPERIAL COLLEGE PRESS, London, 2011).

[9] C. J. Pethick and H. Smith, in *Bose–Einstein Condensation in Dilute Gases* (Cambridge University Press, Cambridge, 2008) pp. 225–254.

[10] R. Grimm, M. Weidemüller, and Y. B. Ovchinnikov, in *Advances In Atomic, Molecular, and Optical Physics*, Vol. 42, edited by B. Bederson and H. Walther (Academic Press, 2000) pp. 95–170.

[11] V. S. Letokhov, Journal of Energy and Power Technology **7**, 272 (1968).

[12] C. Salomon, J. Dalibard, A. Aspect, H. Metcalf, and C. Cohen-Tannoudji, Physical Review Letters **59**, 1659 (1987).

[13] J. Hubbard and B. H. Flowers, Proceedings of the Royal Society of London. Series A. Mathematical and Physical Sciences **276**, 238 (1963).

[14] M. Greiner, O. Mandel, T. Esslinger, T. W. Haensch, and I. Bloch, Nature **415**, 39 (2002).

[15] H. T. Stoof, K. B. Gubbels, and D. B. Dickerscheid, *Ultracold Quantum Fields* (Springer, Bristol, UK, 2009).

[16] L. Landau, Zh. Eksp. teor. Fiz **7** (1937).

[17] Jacob J. Leventhal and Charles E. Burkhardt, in *Topics in Atomic Physics* (Springer New York, New York, NY, 2006) pp. 214–229.

[18] J R Rydberg, The London, Edinburgh, and Dublin Philosophical Magazine and Journal of Science **29**, 331 (1890).

[19] Y. Li, A. Geißler, W. Hofstetter, and W. Li, Physical Review A **97**, 023619 (2018).

[20] H. P. Büchler, E. Demler, M. Lukin, A. Micheli, N. Prokof'Ev, G. Pupillo, and P. Zoller, Physical Review Letters **98**, 060404 (2007).

[21] S. Ji, C. Ates, and I. Lesanovsky, Physical Review Letters **107**, 060406 (2011).

[22] I. Lesanovsky, Physical Review Letters **106**, 025301 (2011).

[23] N. Henkel, F. Cinti, P. Jain, G. Pupillo, and T. Pohl, Physical Review Letters **108**, 265301 (2012).

[24] F. Maucher, N. Henkel, M. Saffman, W. Królikowski, S. Skupin, and T. Pohl, Physical Review Letters **106**, 1 (2011).

[25] J. Honer, H. Weimer, T. Pfau, and H. P. Büchler, Physical Review Letters **105**, 160404 (2010).

[26] F. Cinti, P. Jain, M. Boninsegni, A. Micheli, P. Zoller, and G. Pupillo, Physical Review Letters **105**, 135301 (2010).

[27] N. Henkel, R. Nath, and T. Pohl, Physical Review Letters **104**, 195302 (2010).

[28] A. Geißler, U. Bissbort, and W. Hofstetter, Physical Review A **98**, 063635 (2018).

[29] E. Sela, M. Punk, and M. Garst, Physical Review B - Condensed Matter and Materials Physics **84**, 085434 (2011).

[30] A. Lauer, D. Muth, and M. Fleischhauer, New Journal of Physics **14**, 095009 (2012).

[31] H. Weimer and H. P. Büchler, Physical Review Letters **105**, 230403 (2010).

[32] R. Heidemann, U. Raitzsch, V. Bendkowsky, B. Butscher, R. Löw, L. Santos, and T. Pfau, Physical Review Letters **99**, 163601 (2007).

[33] H. Weimer, R. Löw, T. Pfau, and H. P. Büchler, Physical Review Letters **101**, 1250601 (2008).

[34] J. E. Johnson and S. L. Rolston, Physical Review A **82**, 033412 (2010).

[35] R. Lopes, C. Eigen, N. Navon, D. Clément, R. P. Smith, and Z. Hadzibabic, Physical Review Letters **119**, 190404 (2017).

[36] J. Zeiher, R. Van Bijnen, P. Schauß, S. Hild, J. Y. Choi, T. Pohl, I. Bloch, and C. Gross, Nature Physics **12**, 3835 (2016).

[37] G. Pupillo, A. Micheli, M. Boninsegni, I. Lesanovsky, and P. Zoller, Physical Review Letters **104**, 223002 (2010).

[38] M. Viteau, M. G. Bason, J. Radogostowicz, N. Malossi, D. Ciampini, O. Morsch, and E. Arimondo, Physical Review Letters **107**, 060402 (2011).

[39] Y. Y. Jau, A. M. Hankin, T. Keating, I. H. Deutsch, and G. W. Biedermann, Nature Physics **12**, 3487 (2016).

[40] J. Zeiher, J. Y. Choi, A. Rubio-Abadal, T. Pohl, R. Van Bijnen, I. Bloch, and C. Gross, Physical Review X **7**, 041063 (2017).

[41] M. Barbier, A. Gei\ss{}ler, and W. Hofstetter, Phys. Rev. A **99**, 33602 (2019).

[42] E. Guardado-Sanchez, B. M. Spar, P. Schauss, R. Belyansky, J. T. Young, P. Bienias, A. V. Gorshkov, T. Iadecola, and W. S. Bakr, Physical Review X **11**, 21036 (2021).

[43] Y. Li, J. Yuan, A. Hemmerich, and X. Li, Physical Review Letters **121**, 93401 (2018).

[44] V. Borish, O. Marković, J. A. Hines, S. V. Rajagopal, and M. Schleier-Smith, Physical Review Letters **124**, 063601 (2020).

[45] Y. Chougale and R. Nath, Journal of Physics B: Atomic, Molecular and Optical Physics **49**, 144005 (2016).

[46] C. Gaul, B. J. DeSalvo, J. A. Aman, F. B. Dunning, T. C. Killian, and T. Pohl, Physical Review Letters **116**, 243001 (2016).

[47] J. B. Balewski, A. T. Krupp, A. Gaj, S. Hofferberth, R. Löw, and T. Pfau, New Journal of Physics **16**, 063012 (2014).

[48] M. Płodzień, G. Lochead, J. De Hond, N. J. Van Druten, and S. Kokkelmans, Physical Review A **95**, 043606 (2017).

[49] R. Campargue, *Atomic and Molecular Beams: The State of the Art 2000*, Physics and astronomy online library (Springer, 2001).

[50] G. McCormack, R. Nath, and W. Li, Physical Review A **102**, 023319 (2020).

[51] L. P. Pitaevskii and S. Stringari, *Bose-Einstein Condensation and Superfluidity* (Oxford University Press, 2016).

[52] T. D. Lee, K. Huang, and C. N. Yang, Physical Review **106**, 1135 (1957).

[53] J. Stenger, S. Inouye, A. P. Chikkatur, D. M. Stamper-Kurn, D. E. Pritchard, and W. Ketterle, Physical Review Letters **82**, 4569 (1999).

[54] W. Ketterle, S. Inouye, M. R. Andrews, J. Stenger, H.-J. Miesner, and D. M. Stamper-Kurn, Nature **392**, 151 (1998).

[55] P. Makotyn, C. E. Klauss, D. L. Goldberger, E. A. Cornell, and D. S. Jin, Nature Physics **10**, 116 (2014).

[56] G. I. Martone, P. E. Larre, A. Fabbri, and N. Pavloff, Physical Review A **98**, 063617 (2018).

[57] S. S. Natu and E. J. Mueller, Physical Review A **87**, 053607 (2013).

[58] X. Yin and L. Radzihovsky, Physical Review A **88**, 063611 (2013).

[59] A. G. Sykes, J. P. Corson, J. P. D'Incao, A. P. Koller, C. H. Greene, A. M. Rey, K. R. Hazzard, and J. L. Bohn, Physical Review A **89**, 021601 (2014).

[60] D. H. Smith, E. Braaten, D. Kang, and L. Platter, Physical Review Letters **112**, 110402 (2014).

[61] R. J. Wild, P. Makotyn, J. M. Pino, E. A. Cornell, and D. S. Jin, Physical Review Letters **108**, 145305 (2012).

[62] B. Kain and H. Y. Ling, Physical Review A **90**, 063626 (2014).

[63] C. R. Cabrera, L. Tanzi, J. Sanz, B. Naylor, P. Thomas, P. Cheiney, and L. Tarrue, Science **359**, 301 (2018).

[64] S. S. Natu, L. Campanello, and S. Das Sarma, Physical Review A **90**, 043617 (2014).

[65] U. R. Fischer, Physical Review A **73**, 031602 (2006).

[66] L. Santos, G. V. Shlyapnikov, P. Zoller, and M. Lewenstein, Physical Review Letters **85**, 1791 (2000).

[67] C. Ticknor, R. M. Wilson, and J. L. Bohn, Physical Review Letters **106**, 065301 (2011).

[68] T. Lahaye, C. Menotti, L. Santos, M. Lewenstein, and T. Pfau, Rep. Prog. Phys. **72**, 126401 (2009).

[69] R. M. Wilson and S. Natu, Physical Review A **93**, 053606 (2016).

[70] Y. Cai, M. Rosenkranz, Z. Lei, and W. Bao, Physical Review A **82**, 043623 (2010).

[71] L. Santos, G. V. Shlyapnikov, and M. Lewenstein, Physical Review Letters **90**, 250403 (2003).

[72] L. Chomaz, R. M. Van Bijnen, D. Petter, G. Faraoni, S. Baier, J. H. Becher, M. J. Mark, F. Wächtler, L. Santos, and F. Ferlaino, Nature Physics **14**, 442 (2018).

[73] W. Li, C. Ates, and I. Lesanovsky, Physical Review Letters **110**, 213005 (2013).

[74] C. Ates, B. Olmos, W. Li, and I. Lesanovsky, Physical Review Letters **109**, .233003 (2012).

[75] A. L. Gaunt, T. F. Schmidutz, I. Gotlibovych, R. P. Smith, and Z. Hadzibabic, Physical Review Letters **110**, 200406 (2013).

[76] N. N. Bogoliubov, J. Phys (USSR) **23**, 292 (1947).

[77] Y. Yu, Annals of Physics **323**, 2367 (2008).

[78] S. M. Roccuzzo and F. Ancilotto, Physical Review A **99**, 041601 (2019).

[79] T. Macrì, F. Maucher, F. Cinti, and T. Pohl, Physical Review A **87**, 061602 (2013).

[80] I. Seydi, S. H. Abedinpour, R. E. Zillich, R. Asgari, and B. Tanatar, Physical Review A **101**, 013628 (2020).

[81] Z. Tian, S. Y. Chä, and U. R. Fischer, Physical Review A **97**, 063611 (2018).

[82] A. Griesmaier, J. Werner, S. Hensler, J. Stuhler, and T. Pfau, Physical Review Letters **94**, 160401 (2005).

[83] N. Katz, J. Steinhauer, R. Ozeri, and N. Davidson, Physical Review Letters **89**, 220401 (2002).

[84] S. S. Natu and S. Das Sarma, Physical Review A **88**, 031604 (2013).

[85] H. J. Maris, Physical Review A **49**, 341 (1977).

[86] G. McCormack, R. Nath, and W. Li, Phys. Rev. A **102**, 63329 (2020).

[87] A. Polkovnikov, S. Sachdev, and S. M. Girvin, Physical Review A **66**, 053607 (2002).

[88] T. F. Viscondi and K. Furuya, Journal of Physics A: Mathematical and Theoretical **44**, 175301 (2011).

[89] G. F. Wang, L. B. Fu, and J. Liu, Physical Review A **73**, 013619 (2006).

[90] R. P. Smith and Z. Hadzibabic, in *Physics of Quantum Fluids: New Trends and Hot Topics in Atomic and Polariton Condensates*, edited by A. Bramati and M. Modugno (Springer Berlin Heidelberg, Berlin, Heidelberg, 2013) pp. 341–359.

[91] L. Fallani, C. Fort, J. E. Lye, and M. Inguscio, Opt. Express **13**, 4303 (2005).

[92] A. Smerzi, S. Fantoni, S. Giovanazzi, and S. R. Shenoy, Physical Review Letters **79**, 4950 (1997).

[93] A. Zenesini, H. Lignier, C. Sias, O. Morsch, D. Ciampini, and E. Arimondo, Laser Physics **20**, 1182 (2010).

[94] T. A. Bell, J. A. P. Glidden, L. Humbert, M. W. J. Bromley, S. A. Haine, M. J. Davis, T. W. Neely, M. A. Baker, and H. Rubinsztein-Dunlop, New Journal of Physics **18**, 035003 (2016).

[95] L. Amico and V. Penna, Physical Review Letters **8**, 2189 (1998).

[96] P. Buonsante and V. Penna, Journal of Physics A: Mathematical and Theoretical **41**, 175301 (2008).

[97] A. Muryshev, G. V. Shlyapnikov, W. Ertmer, K. Sengstock, and M. Lewenstein, Physical Review Letters **89**, 110401 (2002).

[98] V. A. Brazhnyi, V. V. Konotop, and V. Kuzmiak, Physical Review A **70**, 043604 (2004).

[99] A. R. Fritsch, M. Lu, G. H. Reid, A. M. Piñeiro, and I. B. Spielman, Physical Review A **101**, 53629 (2020).

[100] W. Li, M. Haque, and S. Komineas, Physical Review A **77**, 053610 (2008).

[101] J. Rogel-Salazar, European Journal of Physics **34**, 247 (2013).

[102] C. Boccato, C. Brennecke, S. Cenatiempo, and B. Schlein, Communications in Mathematical Physics **359**, 975 (2018).

[103] D. McKay, U. Ray, S. Natu, P. Russ, D. Ceperley, and B. Demarco, Physical Review A **91**, 023625 (2015).

[104] D. Witthaut, F. Trimborn, H. Hennig, G. Kordas, T. Geisel, and S. Wimberger, Physical Review A **83**, 063608 (2011).

[105] I. Bloch, Nature Physics **1**, 138 (2005).

[106] T. Byrnes, K. Wen, and Y. Yamamoto, Physical Review A **85**, 040306(R) (2012).

[107] T. Byrnes, D. Rosseau, M. Khosla, A. Pyrkov, A. Thomasen, T. Mukai, S. Koyama, A. Abdelrahman, and E. Ilo-Okeke, Optics Communications **337**, 102 (2015).

[108] S. Dadras, A. Gresch, C. Groiseau, S. Wimberger, and G. S. Summy, Physical Review Letters **121**, 70402 (2018).

[109] G. K. Brennen, C. M. Caves, P. S. Jessen, and I. H. Deutsch, Physical Review Letters **82**, 1060 (1999).

[110] G. J. Milburn, J. Corney, E. M. Wright, and D. F. Walls, Physical Review A **55**, 4318 (1997).

[111] J. Liu, L. Fu, B. Y. Ou, S. G. Chen, D. I. Choi, B. Wu, and Q. Niu, Physical Review A **66**, 023404 (2002).

[112] J. Liu, B. Wu, and Q. Niu, Physical Review Letters **90**, 170404 (2003).

[113] M. Albiez, R. Gati, J. Fölling, S. Hunsmann, M. Cristiani, and M. K. Oberthaler, Physical Review Letters **95**, 010402 (2005).

[114] T. Zibold, E. Nicklas, C. Gross, and M. K. Oberthaler, Physical Review Letters **105**, 204101 (2010).

[115] E. M. Graefe, H. J. Korsch, and D. Witthaut, Physical Review A **73**, 013617 (2006).

[116] B. Liu, L. B. Fu, S. P. Yang, and J. Liu, Physical Review A **75**, 033601 (2007).

[117] J. Liu, S.-C. Li, L.-B. Fu, and D.-F. Ye, *Nonlinear Adiabatic Evolution of Quantum Systems: Geometric Phase and Virtual Magnetic Monopole* (Springer, Singapore, 2018).

[118] A. Dey, D. Cohen, and A. Vardi, Physical Review Letters **121**, 250405 (2018).

[119] A. Dey, D. Cohen, and A. Vardi, Physical Review A **99**, 033623 (2019).

[120] R. Bürkle, A. Vardi, D. Cohen, and J. R. Anglin, Physical Review Letters **123**, 114101 (2019).

[121] B. Wang, H. Zhang, Y. Chen, and L. Tan, European Physical Journal D **71**, 56 (2017).

[122] V. I. Yukalov, K. P. Marzlin, and E. P. Yukalova, Physical Review A **69**, 023620 (2004).

[123] Q. Guo, X. Chen, and B. Wu, Optics Express **22**, 19219 (2014).

[124] T. Lahaye, T. Pfau, and L. Santos, Physical Review Letters **104**, 170404 (2010).

[125] B. Xiong and U. R. Fischer, Physical Review A **88**, 063608 (2013).

[126] A. P. Tonel, L. H. Ymai, K. Wittmann, A. Foerster, and J. Links, SciPost Physics Core **2**, 003 (2020).

[127] A. Gallemí, M. Guilleumas, R. Mayol, and A. Sanpera, Physical Review A **88**, 063645 (2013).

[128] F. Cinti, T. MacRì, W. Lechner, G. Pupillo, and T. Pohl, Nature Communications **5**, 4235 (2014).

[129] B. Xiong, H. H. Jen, and D. W. Wang, Physical Review A **90**, 013631 (2014).

[130] C. H. Hsueh, Y. C. Tsai, and W. C. Wu, Physical Review A **93**, 063605 (2016).

[131] Z. Lan, J. Minar, E. Levi, W. Li, and I. Lesanovsky, Physical Review Letters **115**, 203001 (2015).

[132] X. Li and S. D. Sarma, Nature Communications **6**, 8137 (2015).

[133] A. Angelone, F. Mezzacapo, and G. Pupillo, Physical Review Letters **116**, 135303 (2016).

[134] Y. Zhou, Y. Li, R. Nath, and W. Li, Physical Review A **101**, 013427 (2020).

[135] S. Raghavan, A. Smerzi, S. Fantoni, and S. R. Shenoy, Physical Review A **59**, 620 (1999).

[136] L. D. Landau, Z. Sowjetunion **2**, 46 (1932).

[137] C. Zener, Proc. Roy. Soc. A **33**, 696 (1932).

[138] M. V. Berry, Proceedings of the Royal Society of London. A. Mathematical and Physical Sciences **392**, 45 (1984).

[139] V. Cantoni and L. Mistrangioli, International Journal of Theoretical Physics **31**, 937 (1992).

[140] C. Wittig, Journal of Physical Chemistry B **109**, 8428 (2005).

[141] M. R. Andrews, C. G. Townsend, H. J. Miesner, D. S. Durfee, D. M. Kurn, and W. Ketterle, Science **275**, 637 (1997).

[142] R. J. Ballagh and C. M. Savage, Modern Physics Letters B **14**, 153 (2000).

[143] B. Wu and Q. Niu, Physical Review A **61**, 023402 (2000).

[144] T. Kato, Journal of the Physical Society of Japan **5**, 435 (1950).

[145] J. E. Avron and A. Elgart, Commun. Math. Phys **203**, 445 (1999).

[146] R. Franzosi and V. Penna, Physical Review E **67**, 046227 (2003).

[147] R. Paredes and E. Neri, Journal of Physics B **42**, 035301 (2009).

[148] G. McCormack, R. Nath, and W. Li, Photonics **8**, 554 (2021).

[149] M. Ma, R. Navarro, and R. Carretero-González, Physical Review E **93**, 022202 (2016).

[150] B. P. Anderson, P. C. Haljan, C. A. Regal, D. L. Feder, L. A. Collins, C. W. Clark, and E. A. Cornell, Phys. Rev. Lett. **86**, 2926 (2001).

[151] Z. Dutton, M. Budde, C. Slowe, and L. V. Hau, Science **293**, 663 (2001).

[152] J. Denschlag, Science **287**, 97 (2000).

[153] S. Burger, K. Bongs, S. Dettmer, W. Ertmer, K. Sengstock, A. Sanpera, G. V. Shlyapnikov, and M. Lewenstein, Physical Review Letters **83**, 5198 (1999).

[154] S. L. Cornish, S. T. Thompson, and C. E. Wieman, Physical Review Letters **96**, 170401 (2006).

[155] L. Khaykovich, F. Schreck, G. Ferrari, T. Bourdel, J. Cubizolles, L. D. Carr, Y. Castin, and C. Salomon, Science **296**, 1290 (2002).

[156] K. E. Strecker, G. B. Partridge, A. G. Truscott, and R. G. Hulet, Nature **417**, 150 (2002).

[157] T. Kinoshita, T. Wenger, and D. S. Weiss, Nature **440**, 900 (2006).

[158] B. Xia, W. Hai, and G. Chong, Physics Letters, Section A: General, Atomic and Solid State Physics **351**, 136 (2006).

[159] Y. Li, J. Yuan, A. Hemmerich, and X. Li, Physical Review Letters **121**, 93401 (2018).

[160] G. Chong, W. Hai, and Q. Xie, Physical Review E **71**, 16202 (2005).

[161] I. Gotlibovych, T. F. Schmidutz, A. L. Gaunt, N. Navon, R. P. Smith, and Z. Hadzibabic, Phys. Rev. A **89**, 61604 (2014).

[162] T. F. Schmidutz, I. Gotlibovych, A. L. Gaunt, R. P. Smith, N. Navon, and Z. Hadzibabic, Phys. Rev. Lett. **112**, 40403 (2014).

[163] W. Hai, S. Rong, and Q. Zhu, Physical Review E **78**, 066214 (2008).

[164] S. Sinha and S. Sinha, Phys. Rev. Lett. **125**, 134101 (2020).

[165] E. Boukobza, M. G. Moore, D. Cohen, and A. Vardi, Physical Review Letters **104**, 240402 (2010).

[166] P. Pedri and L. Santos, Phys. Rev. Lett. **95**, 200404 (2005).

[167] I. Tikhonenkov, B. A. Malomed, and A. Vardi, Phys. Rev. Lett. **100**, 90406 (2008).

[168] R. Nath, P. Pedri, and L. Santos, Phys. Rev. Lett. **102**, 50401 (2009).

[169] J. Cuevas, B. A. Malomed, P. G. Kevrekidis, and D. J. Frantzeskakis, Phys. Rev. A **79**, 53608 (2009).

[170] L. E. Young-S, P. Muruganandam, and S. K. Adhikari, J. Phys. B: At. Mol. Opt. Phys. **44**, 101001 (2011).

[171] P. Köberle, H. Cartarius, T. Fabčič, J. Main, and G. Wunner, New Journal of Physics **11**, 23017 (2009).

[172] P. A. Andreev, Chaos: An Interdisciplinary Journal of Nonlinear Science **31**, 23120 (2021).

[173] B. Xiong, J. Gong, H. Pu, W. Bao, and B. Li, Phys. Rev. A **79**, 13626 (2009).

[174] M. Abad, M. Guilleumas, R. Mayol, M. Pi, and D. M. Jezek, EPL **94**, 10004 (2011).

[175] C. Wang, P. G. Kevrekidis, D. J. Frantzeskakis, and B. A. Malomed, Physica D: Nonlinear Phenomena **240**, 805 (2011).

[176] S. K. Adhikari, Phys. Rev. A **89**, 43609 (2014).

[177] A.-X. Zhang and J.-K. Xue, J. Phys. B: At. Mol. Opt. Phys. **45**, 145305 (2012).

[178] R. Fortanier, D. Zajec, J. Main, and G. Wunner, J. Phys. B: At. Mol. Opt. Phys. **46**, 235301 (2013).

[179] K. Wittmann W., E. R. Castro, A. Foerster, and L. F. Santos, Physical Review E **105**, 034204 (2022).

[180] I. Bouchoule and K. Molmer, Physical Review A **65**, 041803 (2002).

[181] W. Li, L. Hamadeh, and I. Lesanovsky, Physical Review A **053615**, 053615 (2012).

[182] B. J. DeSalvo, J. A. Aman, C. Gaul, T. Pohl, S. Yoshida, J. Burgdörfer, K. R. A. Hazzard, F. B. Dunning, and T. C. Killian, Phys. Rev. A **93**, 22709 (2016).

[183] C.-H. Hsueh, C.-W. Wang, and W.-C. Wu, Phys. Rev. A **102**, 63307 (2020).

[184] A. Wolf, J. B. Swift, H. L. Swinney, and J. A. Vastano, Physica D: Nonlinear Phenomena **16**, 285 (1985).

[185] A. V. Andreev, A. G. Balanov, T. M. Fromhold, M. T. Greenaway, A. E. Hramov, W. Li, V. V. Makarov, and A. M. Zagoskin, npj Quantum Information **7**, 1 (2021).

[186] S. Eckel, J. G. Lee, F. Jendrzejewski, N. Murray, C. W. Clark, C. J. Lobb, W. D. Phillips, M. Edwards, and G. K. Campbell, Nature **506**, 200 (2014).

[187] A. Trenkwalder, G. Spagnolli, G. Semeghini, S. Coop, M. Landini, P. Castilho, L. Pezzè, G. Modugno, M. Inguscio, A. Smerzi, and M. Fattori, Nature Physics **12**, 826 (2016).

[188] M. O. Scully and M. S. Zubairy, *Quantum Optics* (Cambridge University Press, Cambridge, 1997).

[189] E. R. Castro, J. Chávez-Carlos, I. Roditi, L. F. Santos, and J. G. Hirsch, "Quantum-classical correspondence of a system of interacting bosons in a triple-well potential," (2021).

[190] G. Datseris, Journal of Open Source Software **3**, 598 (2018).

[191] G. Baier and M. Klein, Physics Letters A **151**, 281 (1990).

[192] G. Baier and S. Sahle, Physical Review E **51**, R2712 (1995).

[193] T. Kapitaniak, K.-E. Thylwe, I. Cohen, and J. Wojewoda, Chaos, Solitons & Fractals **5**, 2003 (1995).

[194] A. E. Tarkhov, S. Wimberger, and B. V. Fine, Phys. Rev. A **96**, 23624 (2017).

[195] A. Lerose and S. Pappalardi, Physical Review A **102**, 32404 (2020).

[196] L. Pausch, E. G. Carnio, A. Rodríguez, and A. Buchleitner, Phys. Rev. Lett. **126**, 150601 (2021).

[197] C. Kollath, G. Roux, G. Biroli, and A. M. Läuchli, J. Stat. Mech. **2010**, P08011 (2010).

[198] Y. Chen and Z. Cai, Phys. Rev. A **101**, 23611 (2020).